Fracture-based fabrication of a size-controllable micro/nanofluidic platform for mapping of DNA/chromatin

by

Byoung Choul Kim

A dissertation submitted in partial fulfillment
of the requirements for the degree of
Doctor of Philosophy
(Biomedical Engineering)
in the University of Michigan
2014

Doctoral Committee:

Professor Shuichi Takayama, Chair
Professor Mark Burns
Professor Xudong Fan
Research Assistant Professor Yifan Liu
Professor Michael D. Thouless

To my family and friends

Acknowledgments

This dissertation is a sweet fruit cultivated through collaborations with a number of excellent people whom I have worked with over the years since I entered this program.

I would first like to express my gratitude to Professor Shuichi Takayama, for his mentorship and the invaluable support he provided throughout the period of my graduate study. The opportunity to work with him allowed me to explore many challenging questions across diverse fields of study. His passion for science and engineering served as a constant source of inspiration and encouragement as I worked to pursue the questions I sought to address through my own efforts.

I would also like to thank Professors Thouless and Liu. For Professor Thouless, I would like to express my gratitude for his thoughtful comments, constructive criticism, and guidance; which allowed me to pursue my work in the area of fracture mechanics. For Professor Liu, who introduced me to a new biological system; I would like to express my gratitude for serving as an invaluable co-advisor, willing to provide valuable advice and insight whenever needed. Finally, I would like to warmly thank my committee members, Professor Burns and Professor Xudong, who have mentored me. Their constructive criticism and comments proved very useful in helping me to develop my project.

In addition to my faculty advisors, I extend my deepest gratitude to the numerous gifted collaborators with whom I worked over the years: Jessie Huang at Prof. Thouless lab,

Shan Gao and Dui Wen at Prof. Liu lab, Jae Sung Lee at Prof. Burns lab, Mou-Chi Cheng and Chanrith Siv at Julie Biteen Lab. Their help and support were invaluable in allowing me to finish my work. I would not have accomplished anything without them.

During the years I spent in Ann Arbor, I was fortunate to have also worked with a number of brilliant individuals in the Takayama lab: Toshiki Matsuoka, Sung Jin Kim, Joong Yull Park, Se Joong Kim, Chris Moraes, Priyan Weerappuli, Brendan Leung, John Frampton, Minsub Han, Cedric Bathany, Sasha Cai Lesher-Perez, Joseph Labuz, David Lai, Stephen Cavnar, Madhuresh Sumit, Chao Zhang, Cameron Yamanishi, Joyce Hanching Chiu, Amy Hsiao, Yi-Chung Tung, Jason Kuo, Arlyne Simon, Wansik Cha, Bobak Mosadegh, Hossein Tavana, Tommaso Bersano-Begey, Ryuiji Yokokawa, Joshua White, Nicholas Douville, and my undergraduate mentee, Lisa Liang. Their presence and energy helped make my time in Ann Arbor both joyous and productive.

I'm also thankful for my advisors and friends in Korea: Eun Song Lee, Dae Hwan Park, Yong Jae Jeon, Prof. Jin ho Choy, Prof. In Suk Lee, Prof. Hyungil Jung, Prof. Kang Yell Choi, Hyun Seung Koh, Sang Won Min, Jiwon Lee, Chan Ho Park, Seung Yup Lee, Joong Hwan Bahng, Daewoo Park, Eunjoo Hwang, Gu Eon Kang, Sean Park, Hyesun Jun.

Lastly, but most importantly, I would like to express my heartfelt gratitude to my family. Their unwavering support provided me a source of strength that provided context and a sense of transience to the challenges which my work, and life in a new country, presented. Thank you.

Table of Contents

List of Figures

List of Tables

Abstract

In the years since the launch of The Human Genome Project (HGP), which significantly increased our understanding of biological inheritance by revealing the structure and function of genetic material, tangential research efforts have revealed mechanisms of inheritance that extend beyond the sequence of nucleic acids within an individual's genome. The study of these mechanisms, referred to as epigenetics, now lies at the frontier of biomedical research. While much is known regarding genetic inheritance, the complexity of chromosome structure and lack of appropriate methodologies have long hindered mechanistic dissection of epigenetic inheritance. The work presented in this dissertation seeks three fundamental objectives: (1) the development of appropriate tools for chromatin mapping, (2) the identification of a well-defined model system, and (3) the use of 'super-resolution imaging', working with a multi-disciplinary team of collaborators having experience raging from the basic biology to advanced engineering.

First, a unique micro/nanofluidics platform was developed utilizing fracture-based fabrication techniques. The use of such techniques, combined with the careful selection of appropriate materials, enabled the formation of channels with dimensions that could be modified by simply modifying the magnitude of the uniaxial strain applied. By integrating stress focusing notch micro-features into the soft elastomer, polydimethylsiloxane (PDMS), nano-scale fractures were generated at desired positions, producing an array of nano-channels.

These adjustable channels were then utilized to achieve the efficient pre-concentration, capturing, and linearization of DNA and chromatin via nano-confinement and a squeezing flow. In the tuneable channel device, DNA molecules were pre-

concentrated up to 10,000 fold at the defined position using electrophoresis, and were successfully trapped and linearized up to its contour length for epigenetic marker profiling.

Finally, *Tetrahymena* was selected as an optimal biological system, and was used to elucidate the spatial distribution of histones along replicated DNA, as well as to characterize specific histone-DNA interactions occurring during replication, with the aid of super-resolution microscopy.

This multi-disciplinary dissertation project provides insight into both the unknown epigenetic changes occurring during DNA replication, and the biological machinery underlying fundamental DNA-histone interactions. The application of this adjustable fluidics platform to other biological model species may provide a means to establish other epigenetic marker maps including patterns of post translational modifications of histone and DNA methylation to study yet unknown epigenetic mechanisms.

Chapter 1

Introduction

The contents in this chapter have been adapted with minor modifications from the following publication: 'Micro-and nanoflduic technologies for epigenetic profiling', *Biomicrofluidics*, 2013

1.1 BACKGROUND

The biological 'instruction manual' for structure, function and growth has long been considered to be encoded in the DNA of organisms. Interactions between DNA and external factors drive differential transcription of these genes into proteins, producing transmittable signals that regulate function. However, cells can present distinct heritable phenotypes, without changes in the underlying DNA. Alterations to the instruction manual via these 'epigenetic' changes, such as DNA methylation or histone modifications, have recently generated tremendous scientific interest (Papp and Plath, 2013). As these changes are transmitted from parent to child, the existence of epigenetic mechanisms suggest that lifestyle choices may impact future generations (Anway et al., 2005; Bohacek and Mansuy, 2013; Crews et al., 2012; Guerrero-Bosagna et al., 2010; Guerrero-Bosagna and Skinner, 2009; Lim and Brunet, 2013). Conversely, epigenetic mechanisms may enable us to manipulate or avoid the conditions that drive phenotypic expression of a genetic disorder. Hence, with implications in cancer (Feinberg and

Tycko, 2004; Jones and Baylin, 2007; Waldmann and Schneider, 2013), autism (Grafodatskaya et al., 2010; Pareja-Galeano et al., 2013), and Alzheimer's disease (Chouliaras et al., 2010; Mastroeni et al., 2010), the epigenetic paradigm provides a powerful set of tools with which to understand the transmission and etiology of diseases, and ultimately design treatments for genetic disorders that need not rely on potentially hazardous genetic modification (Ptak and Petronis, 2008).

Epigenetics also have significant implications in the fields of tissue engineering (Atala, 2004), regenerative medicine (Cherry and Daley, 2012; Rizzino, 2007), and creating artificial in vitro cell culture models (Postovit et al., 2006); particularly in sourcing cells for these technologies. A particularly promising approach is the use of embryonic, adult and induced pluripotent stem cells (Takahashi and Yamanaka, 2006), which can be differentiated towards a specified phenotype (Carr et al., 2009). This powerful technique enables basic scientists and clinicians to create autologous artificial tissues for transplantation (Wu and Hochedlinger, 2011), or to better study various aspects of disease using genetically identical source materials; but the epigenetic paradigm raises a significant concerns about this process (Pujadas and Feinberg, 2012). Differentiated cells may contain significant and previously unsuspected epigenetic variations (Fig. 1), arising from the use of chemical differentiation reagents (Lister et al., 2011) and from requirements to prepare undifferentiated stem cells for long periods in culture (Baker et al., 2007). These epigenetic differences may lead to unexpected and potentially detrimental cell functionality, such as uncontrolled cancerous proliferation (Baker et al., 2007; Lister et al., 2011; Pujadas and Feinberg, 2012). Hence, techniques to rapidly assess the epigenetic profiles of differentiated and diseased cells are of critical importance in a broad variety of applications.

1.2 CHALLENGES IN CHROMATIN ANALYSIS

Chromatin structure influences cell function

DNA in a living cell must be accessible so as to readily perform vital biological functions such as gene transcription, DNA replication, DNA recombination and DNA repair. At the same time, however, the meter-long eukaryotic DNA must be highly condensed so as to fit into the nucleus, which affords space of only a few microns in size. The two seemingly incompatible requirements of extremely compact storage and rapid accessibility have prompted a decade of intense studies of chromatin organization. The hierarchical structure of chromatin necessary to achieve this degree of packing and accessibility of DNA has subtle and diverse features at all levels of organization, some of which have only recently been understood (Luger et al., 2012). Since the structure of chromatin itself likely regulates aspects of gene transcription (Rubtsov et al., 2006), understanding these factors is of critical importance in probing epigenetics. Intensive research has been conducted to characterize the structural and functional properties of chromatin using diverse experimental and modeling techniques including atomic force microscopy (Montel et al., 2009; Sato et al., 1999; Wang et al., 2002), optical/magnetic tweezers,(Cui and Bustamante, 2000; Gupta et al., 2009), electron microscopy (Dorigo et al., 2004; Grigoryev et al., 2009), and X-ray scattering methods (Nishino et al., 2012; Schalch et al., 2005).

DNA is coiled around a nucleosome core comprised of four pairs of histone proteins, and nucleosomes are connected to each other by linker DNA (often represented by a "beads-on-a-string" model) (Schlick et al., 2012). However, the higher-order structure that the primary chromatin strand coils into is still actively debated (Grigoryev et al., 2009). A regularly arranged secondary structure known as the '30 nm fiber' is believed to exist (Dorigo et al., 2004; Grigoryev et al., 2009; Kruithof et al., 2009). Our current understanding of chromatin structure suggests that the chromatin within a cell exists in a buoyant state, providing greater accessibility for biological purposes (Fussner

et al., 2011). Also, it is known that, on a primary structural level, there are small variations in amino-acid sequences even though core histones are highly conserved proteins across species. The variations can influence the stability and dynamic state of the primary structure, thereby influencing the rate and duration of gene activation. Taken together, the variability, irregularity and dynamics in the hierarchy of chromatin structures represents an epigenetic mechanism, as they form based on specific needs and conditions in a given biological environment. Simply mapping end-point protein-DNA interactions using conventional methods are unable to recreate and capture these dynamic complexities.

Broad variety of histone modifications

A key structural unit of chromatin is the nucleosome. Nucleosomes in eukaryotes consist of DNA coiled around an octamer core comprised of four types of histone proteins: H2A, H2B, H3 and H4, each of which has a high affinity for DNA. Nucleosomes are bound at the entry and exit sites of the DNA by the linker histone H1 (Finch and Klug, 1976; Woodcock et al., 1984; Worcel et al., 1981). About 147 base-pairs of DNA are tightly wound around a histone octamer. The terminal regions of these histones are exposed to modifications, such as acetylation and methylation that can dynamically change chromatin structure, regulating accessibility of proteins to the DNA (Zentner and Henikoff, 2013). For example, activity of transcription factors can be blocked or enhanced based on modification of the histone. This mechanism makes it physically possible to regulate gene expression independently from the DNA sequence, creating an epigenetic effect (Fierz and Muir, 2012).

The variety of known histone modifications is large and growing. The most extensively documented modifications include acetylation, methylation, phosphorylation, ubiquitination and biotinylation (Latham and Dent, 2007). In particular, acetylation on histone H4 and methylation of lysine 9 on histone H3 can significantly influence

chromatin structure of euchromatin (decondensed chromatin) and heterochromatin (highly condensed chromatin) respectively (Nakayama et al., 2001; Narlikar et al., 2002; Rea et al., 2000; Tamaru, 2010). Hence, patterns of these histone modifications, collectively referred to as the 'histone code' can physically regulate gene expression and transcription (Jaenisch and Bird, 2003). Currently, researchers commonly consider 24 histone modifications of acetylation and methylation on 22 modification sites (Fig 2). Modifications are quickly being added to this list to include ubiquitination (Orrick et al., 1973; Yeoman et al., 1973), ADP-ribosylation (Smith and Stocken, 1973; Ueda et al., 1975), citrullination (Nakashima et al., 2002), and sumoylation (Nathan et al., 2006). Analysis of each of these modifications requires the development and validation of uniquely specific antibodies.

One genome but many epigenomes per person.

Generally, the genomic DNA sequence of cells within an individual person is all the same. The human genome project, successfully achieved over 10 years ago and progressively improved upon, enables an individual person's DNA to be mapped for less than $1000, from amplification of genetic contents of a single cell (Ku and Roukos, 2013). While knowledge of the complete genomic sequence is useful to detect genomic variations such as single-nucleotide polymorphism analysis, this information is not always sufficient to understand individual cell type-based function and phenotype. To understand cell type-dependent functional differences, not only the DNA sequence but knowledge of how that DNA is packaged within the cell's nucleus is required. In other words, epigenomic information of that specific cell that includes patterns of histone modifications across the whole genome is needed (Bernstein et al., 2007). This is because significant epigenomic diversity exists not only between individuals in a population, but from tissue to tissue, and between individual cells within the same tissue (Jones and Baylin, 2007; Schmitz et al., 2013).

Unfortunately, no technology currently exists with which to study the epigenetic profile of chromatin from a single cell. DNA amplification cannot be utilized, as it does not replicate the modified histones and structure of the chromatin necessary for epigenetic analysis. Recently, the Encyclopedia of DNA Elements (ENCODE) project undertook a massive research program involving the compilation of many researchers' efforts in mapping the epigenome (Ecker et al., 2012). However, even this well-funded consortium chose to study cell lines, at least in part, due to the need to produce sufficient numbers of cells for the epigenetic analyses such as chromatin immunoprecipitation (ChIP). The ability to map histone states using chromatin from a single cell would greatly reduce the time and cost involved in such endeavors. Additionally, the ability to perform histone mapping of single cells would open new opportunities in understanding cell-to-cell variability of the epigenome as well as in identifying and understanding rare cells such as cancer progenitors or pluripotent stem cells which play critical roles in disease and repair but are currently very difficult to analyze due to lack of starting cellular materials.

1.3 MICRO- AND NANOFLUIDIC APROACHES

Conventional methods to study chromatin are limited in their ability to provide sufficient information at a single cell level – information critical for rare cell or cell differentiation research (Dahl and Collas, 2007, 2008a, b; Flanagin et al., 2008; Kuo and Allis, 1999; Nelson et al., 2006; O'Neill et al., 2006). These issues are compounded by the complexity and insufficient-throughput of such technologies given the challenges associated with having over 30 histone modification possibilities and multiple epigenomes per person. Recent advancements in micro/nanotechnology offer opportunities for the study of chromatin at the single cell level using mechanisms that allow for precise control, improved handling, and higher throughput studies.

ChIP in micro/nanofluidics

ChIP has been exploited to study DNA-protein interactions and histone modifications for many years. Despite the capabilities and history of this technology, ChIP assays can be challenging to perform. It requires several sequential steps: 1) cell lysis, 2) binding of an antibody to a target DNA-binding protein, 3) immunoprecipitation of the antibody and antigen complex using a secondary antibody and beads, 4) purification, and 5) further analysis such as PCR and sequencing. Multiple processing steps in any assay typically results in larger sample requirements and assay time. In contrast to conventional technologies, miniaturized micro/nanofluidics platforms require only small amount of sample volume, can simplify and accelerate the assay, and enables the study of single cells in a high-throughput manner.

Microfluidic systems can greatly improve antibody reaction and immunoprecipitation times in ChIP assays and can also be used to improve assay throughput and automation. For instance, Quake and coworkers designed an automated microfluidic platform for ChIP that requires small cell populations. Fluid flow within the microfluidic chip was controlled using integrated pneumatic valves and pumps, enabling rapid and automated processing of immunoprecipitation procedures. Another approach for improved ChIP based histone modification analysis in a PDMS microfluidic device combining with magnetic beads. Rapid immunoprecipitation and purification of target DNA are achieved. Similar to the microfluidics devices described above, fluids are controlled in the PDMS microfluidic device by pumps and valves.

Despite advances made in using microfluidics to improve ChIP methodologies, there is still a need to enable detection of multiple types of histone modifications simultaneously across the whole genome, on a single-cell level, in order to study epigenetic influences of rare cells. Achieving this goal requires technologies that can bypass two limitations associated with the conventional ChIP process: (1) The need for large number of cells to provide the required amount of nuclear material; and (2) The

inability to amplify chromatin. These challenges have led to development of alternatives to ChIP to identify histone modifications directly on chromatin.

Chromatin linearization

Since chromatin exists in a highly compact state, specific markers in chromatin are quite difficult to discriminate when tangled. ChIP assays include a shearing step to generate chromatin fragments to overcome the entanglement problem. The harsh mechanical forces, however, may damage epigenetic information. More importantly, extensive fragmentation of the chromatin strand destroys positional information for epigenetic markers on the genomic structure. An alternative approach is to directly observe the position of epigenetic markers along a long strand of chromatin. This approach requires chromatin to be linearized, a task suited to micro and nano-fluidics. Nanochannels are well known to provide confinement conditions that allow for reliable linearization of DNA. (Chantiwas et al., 2011; Douville et al., 2008; Lam et al., 2012; Reisner et al., 2005; Reisner et al., 2012) More recently, chromatin has also been linearized by nanoconfinement. With fluorescent labeling using multiple antibodies against specific histone modification, positions of epigenetic markers can then be directly imaged. (Cipriany et al., 2012; Cipriany et al., 2010; Matsuoka et al., 2012)

To date, efforts to study DNA linearization in micro/nanofluidics have been oriented toward the visualization of single DNA molecules and the detection of target markers on DNA.(Hsieh et al., 2008; Levy and Craighead, 2010; Tegenfeldt et al., 2004)

1.4 DISSERTATION RESEARCH PERSPECTIVES

The ability to map the whole human genome, in combination with more recent advances in chromatin analysis based on histone modifications by the ENCODE project have provided the basis for scientists to identify the dynamic processes involved in

epigenetics. The limitations imposed by available techniques, however, require development of additional novel technologies to enable genome-wide epigenetic analysis, using very few cells in a time and cost efficient manner. The ability to analyze positional relationships between multiple histone markers simultaneously from a single chromatin molecule would be one example of a novel tool that would enhance our mechanistic understanding of the roles of the various histone markings and how it contributes to normal physiology as well as disease. There are still relatively few micro- and nanofluidic methods that have been developed for chromatin analysis. Therefore, the tuneable nanofluidic platform described in my dissertation presents a promising approach towards achieving this goal. In conjunction with advances in super resolution imaging techniques, this platform approaches direct visualization of chromatin at the single nucleosome level for the structural analysis of chromatin, and the inheritance of chromatin during DNA replication.

FIGURES

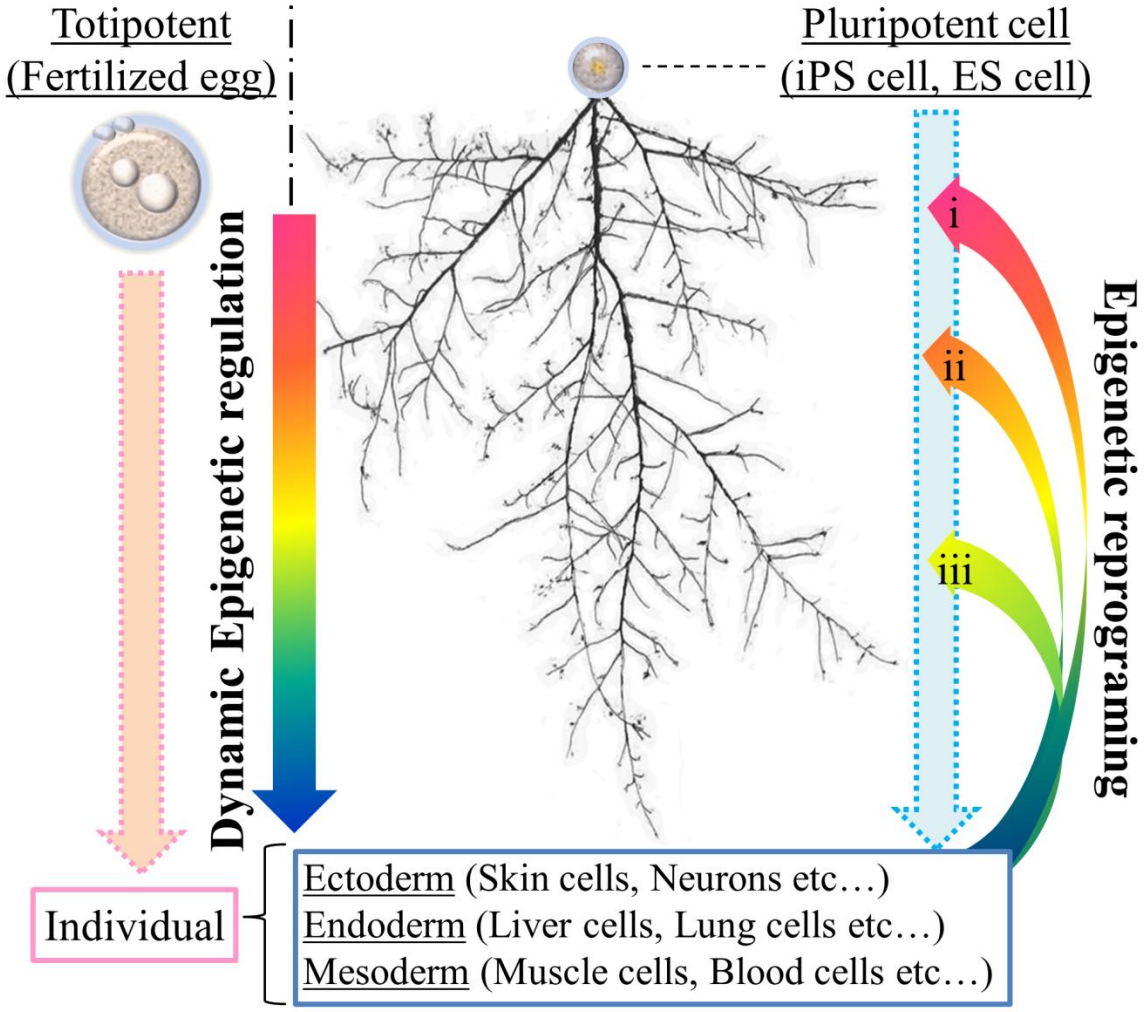

Figure 1.1 The concept of epigenetic regulation and reprograming

Fertilized egg represents totipotency or iPS and ES represents pluripotency, they have the potential to differentiate down all pathways through dynamic epigenetic regulation. Bottom roots represent differentiated cells such as skin, neurons, liver, lung, muscle, blood cells etc. Alternatively, differentiated cell types in an individual can reverse their fate through epigenetic reprogramming. These induced pluripotent cells can be re-differentiated to various cell types through dynamic epigenetic regulation, but cannot develop into an individual

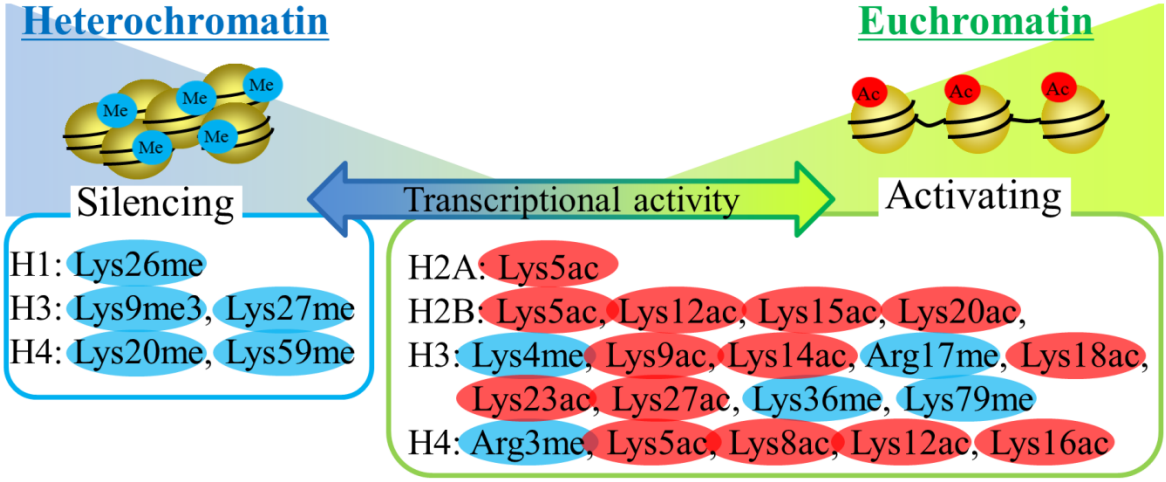

Figure 1.2 Transcriptional relationship between chromatin structure and histone modifications on histones.

Gene transcriptional activity can be controlled by chromatin structure such as heterochromatin and euchromatin. These chromatin structures can also be controlled by histone modifications, as demonstrated in the diagram which shows post-translational histone modifications on each histone. (Ac, acetylation; Me, Methylation).

1.5 REFENCES

Anway, M.D., Cupp, A.S., Uzumcu, M., and Skinner, M.K. (2005). Epigenetic transgenerational actions of endocrine disruptors and male fertility. Science *308*, 1466-1469.

Atala, A. (2004). Tissue engineering and regenerative medicine: concepts for clinical application. Rejuvenation research *7*, 15-31.

Baker, D.E., Harrison, N.J., Maltby, E., Smith, K., Moore, H.D., Shaw, P.J., Heath, P.R., Holden, H., and Andrews, P.W. (2007). Adaptation to culture of human embryonic stem cells and oncogenesis in vivo. Nature biotechnology *25*, 207-215.

Bernstein, B.E., Meissner, A., and Lander, E.S. (2007). The mammalian epigenome. Cell *128*, 669-681.

Bohacek, J., and Mansuy, I.M. (2013). Epigenetic inheritance of disease and disease risk. Neuropsychopharmacology : official publication of the American College of Neuropsychopharmacology *38*, 220-236.

Carr, A.J., Vugler, A.A., Hikita, S.T., Lawrence, J.M., Gias, C., Chen, L.L., Buchholz, D.E., Ahmado, A., Semo, M., Smart, M.J.*, et al.* (2009). Protective effects of human iPS-derived retinal pigment epithelium cell transplantation in the retinal dystrophic rat. PloS one *4*, e8152.

Chantiwas, R., Park, S., Soper, S.A., Kim, B.C., Takayama, S., Sunkara, V., Hwang, H., and Cho, Y.K. (2011). Flexible fabrication and applications of polymer nanochannels and nanoslits. Chemical Society reviews *40*, 3677-3702.

Cherry, A.B., and Daley, G.Q. (2012). Reprogramming cellular identity for regenerative medicine. Cell *148*, 1110-1122.

Chouliaras, L., Rutten, B.P., Kenis, G., Peerbooms, O., Visser, P.J., Verhey, F., van Os, J., Steinbusch, H.W., and van den Hove, D.L. (2010). Epigenetic regulation in the pathophysiology of Alzheimer's disease. Progress in neurobiology *90*, 498-510.

Cipriany, B.R., Murphy, P.J., Hagarman, J.A., Cerf, A., Latulippe, D., Levy, S.L., Benitez, J.J., Tan, C.P., Topolancik, J., Soloway, P.D.*, et al.* (2012). Real-time analysis and selection of methylated DNA by fluorescence-activated single molecule sorting in a nanofluidic channel. Proceedings of the National Academy of Sciences of the United States of America *109*, 8477-8482.

Cipriany, B.R., Zhao, R., Murphy, P.J., Levy, S.L., Tan, C.P., Craighead, H.G., and

Soloway, P.D. (2010). Single molecule epigenetic analysis in a nanofluidic channel. Analytical chemistry *82*, 2480-2487.

Crews, D., Gillette, R., Scarpino, S.V., Manikkam, M., Savenkova, M.I., and Skinner, M.K. (2012). Epigenetic transgenerational inheritance of altered stress responses. Proceedings of the National Academy of Sciences of the United States of America *109*, 9143-9148.

Cui, Y., and Bustamante, C. (2000). Pulling a single chromatin fiber reveals the forces that maintain its higher-order structure. Proceedings of the National Academy of Sciences of the United States of America *97*, 127-132.

Dahl, J.A., and Collas, P. (2007). Q2ChIP, a quick and quantitative chromatin immunoprecipitation assay, unravels epigenetic dynamics of developmentally regulated genes in human carcinoma cells. Stem Cells *25*, 1037-1046.

Dahl, J.A., and Collas, P. (2008a). MicroChIP--a rapid micro chromatin immunoprecipitation assay for small cell samples and biopsies. Nucleic acids research *36*, e15.

Dahl, J.A., and Collas, P. (2008b). A rapid micro chromatin immunoprecipitation assay (microChIP). Nature protocols *3*, 1032-1045.

Dorigo, B., Schalch, T., Kulangara, A., Duda, S., Schroeder, R.R., and Richmond, T.J. (2004). Nucleosome arrays reveal the two-start organization of the chromatin fiber. Science *306*, 1571-1573.

Douville, N., Huh, D., and Takayama, S. (2008). DNA linearization through confinement in nanofluidic channels. Analytical and bioanalytical chemistry *391*, 2395-2409.

Ecker, J.R., Bickmore, W.A., Barroso, I., Pritchard, J.K., Gilad, Y., and Segal, E. (2012). Genomics: ENCODE explained. Nature *489*, 52-55.

Feinberg, A.P., and Tycko, B. (2004). The history of cancer epigenetics. Nature reviews Cancer *4*, 143-153.

Fierz, B., and Muir, T.W. (2012). Chromatin as an expansive canvas for chemical biology. Nature chemical biology *8*, 417-427.

Finch, J.T., and Klug, A. (1976). Solenoidal model for superstructure in chromatin. Proceedings of the National Academy of Sciences of the United States of America *73*, 1897-1901.

Flanagin, S., Nelson, J.D., Castner, D.G., Denisenko, O., and Bomsztyk, K. (2008). Microplate-based chromatin immunoprecipitation method, Matrix ChIP: a platform to

study signaling of complex genomic events. Nucleic acids research *36*, e17.

Fussner, E., Ching, R.W., and Bazett-Jones, D.P. (2011). Living without 30nm chromatin fibers. Trends in biochemical sciences *36*, 1-6.

Grafodatskaya, D., Chung, B., Szatmari, P., and Weksberg, R. (2010). Autism spectrum disorders and epigenetics. Journal of the American Academy of Child and Adolescent Psychiatry *49*, 794-809.

Grigoryev, S.A., Arya, G., Correll, S., Woodcock, C.L., and Schlick, T. (2009). Evidence for heteromorphic chromatin fibers from analysis of nucleosome interactions. Proceedings of the National Academy of Sciences of the United States of America *106*, 13317-13322.

Guerrero-Bosagna, C., Settles, M., Lucker, B., and Skinner, M.K. (2010). Epigenetic transgenerational actions of vinclozolin on promoter regions of the sperm epigenome. PloS one *5*.

Guerrero-Bosagna, C.M., and Skinner, M.K. (2009). Epigenetic transgenerational effects of endocrine disruptors on male reproduction. Seminars in reproductive medicine *27*, 403-408.

Gupta, P., Zlatanova, J., and Tomschik, M. (2009). Nucleosome assembly depends on the torsion in the DNA molecule: a magnetic tweezers study. Biophysical journal *97*, 3150-3157.

Hsieh, C.C., Balducci, A., and Doyle, P.S. (2008). Ionic effects on the equilibrium dynamics of DNA confined in nanoslits. Nano letters *8*, 1683-1688.

Jaenisch, R., and Bird, A. (2003). Epigenetic regulation of gene expression: how the genome integrates intrinsic and environmental signals. Nature genetics *33 Suppl*, 245-254.

Jones, P.A., and Baylin, S.B. (2007). The epigenomics of cancer. Cell *128*, 683-692.

Kruithof, M., Chien, F.T., Routh, A., Logie, C., Rhodes, D., and van Noort, J. (2009). Single-molecule force spectroscopy reveals a highly compliant helical folding for the 30-nm chromatin fiber. Nature structural & molecular biology *16*, 534-540.

Ku, C.S., and Roukos, D.H. (2013). From next-generation sequencing to nanopore sequencing technology: paving the way to personalized genomic medicine. Expert review of medical devices *10*, 1-6.

Kuo, M.H., and Allis, C.D. (1999). In vivo cross-linking and immunoprecipitation for studying dynamic Protein:DNA associations in a chromatin environment. Methods *19*,

425-433.

Lam, E.T., Hastie, A., Lin, C., Ehrlich, D., Das, S.K., Austin, M.D., Deshpande, P., Cao, H., Nagarajan, N., Xiao, M.*, et al.* (2012). Genome mapping on nanochannel arrays for structural variation analysis and sequence assembly. Nature biotechnology *30*, 771-776.

Latham, J.A., and Dent, S.Y. (2007). Cross-regulation of histone modifications. Nature structural & molecular biology *14*, 1017-1024.

Levy, S.L., and Craighead, H.G. (2010). DNA manipulation, sorting, and mapping in nanofluidic systems. Chemical Society reviews *39*, 1133-1152.

Lim, J.P., and Brunet, A. (2013). Bridging the transgenerational gap with epigenetic memory. Trends in genetics : TIG *29*, 176-186.

Lister, R., Pelizzola, M., Kida, Y.S., Hawkins, R.D., Nery, J.R., Hon, G., Antosiewicz-Bourget, J., O'Malley, R., Castanon, R., Klugman, S.*, et al.* (2011). Hotspots of aberrant epigenomic reprogramming in human induced pluripotent stem cells. Nature *471*, 68-73.

Luger, K., Dechassa, M.L., and Tremethick, D.J. (2012). New insights into nucleosome and chromatin structure: an ordered state or a disordered affair? Nature reviews Molecular cell biology *13*, 436-447.

Mastroeni, D., Grover, A., Delvaux, E., Whiteside, C., Coleman, P.D., and Rogers, J. (2010). Epigenetic changes in Alzheimer's disease: decrements in DNA methylation. Neurobiology of aging *31*, 2025-2037.

Matsuoka, T., Kim, B.C., Huang, J., Douville, N.J., Thouless, M.D., and Takayama, S. (2012). Nanoscale squeezing in elastomeric nanochannels for single chromatin linearization. Nano letters *12*, 6480-6484.

Montel, F., Menoni, H., Castelnovo, M., Bednar, J., Dimitrov, S., Angelov, D., and Faivre-Moskalenko, C. (2009). The dynamics of individual nucleosomes controls the chromatin condensation pathway: direct atomic force microscopy visualization of variant chromatin. Biophysical journal *97*, 544-553.

Nakashima, K., Hagiwara, T., and Yamada, M. (2002). Nuclear localization of peptidylarginine deiminase V and histone deimination in granulocytes. The Journal of biological chemistry *277*, 49562-49568.

Nakayama, J., Rice, J.C., Strahl, B.D., Allis, C.D., and Grewal, S.I. (2001). Role of histone H3 lysine 9 methylation in epigenetic control of heterochromatin assembly. Science *292*, 110-113.

Narlikar, G.J., Fan, H.Y., and Kingston, R.E. (2002). Cooperation between complexes

that regulate chromatin structure and transcription. Cell *108*, 475-487.

Nathan, D., Ingvarsdottir, K., Sterner, D.E., Bylebyl, G.R., Dokmanovic, M., Dorsey, J.A., Whelan, K.A., Krsmanovic, M., Lane, W.S., Meluh, P.B.*, et al.* (2006). Histone sumoylation is a negative regulator in Saccharomyces cerevisiae and shows dynamic interplay with positive-acting histone modifications. Genes & development *20*, 966-976.

Nelson, J.D., Denisenko, O., Sova, P., and Bomsztyk, K. (2006). Fast chromatin immunoprecipitation assay. Nucleic acids research *34*, e2.

Nishino, Y., Eltsov, M., Joti, Y., Ito, K., Takata, H., Takahashi, Y., Hihara, S., Frangakis, A.S., Imamoto, N., Ishikawa, T.*, et al.* (2012). Human mitotic chromosomes consist predominantly of irregularly folded nucleosome fibres without a 30-nm chromatin structure. The EMBO journal *31*, 1644-1653.

O'Neill, L.P., VerMilyea, M.D., and Turner, B.M. (2006). Epigenetic characterization of the early embryo with a chromatin immunoprecipitation protocol applicable to small cell populations. Nature genetics *38*, 835-841.

Orrick, L.R., Olson, M.O., and Busch, H. (1973). Comparison of nucleolar proteins of normal rat liver and Novikoff hepatoma ascites cells by two-dimensional polyacrylamide gel electrophoresis. Proceedings of the National Academy of Sciences of the United States of America *70*, 1316-1320.

Papp, B., and Plath, K. (2013). Epigenetics of reprogramming to induced pluripotency. Cell *152*, 1324-1343.

Pareja-Galeano, H., Sanchis-Gomar, F., and Mayero, S. (2013). Autism spectrum disorders: possible implications of BDNF modulation through epigenetics. Acta psychiatrica Scandinavica.

Postovit, L.M., Seftor, E.A., Seftor, R.E., and Hendrix, M.J. (2006). A three-dimensional model to study the epigenetic effects induced by the microenvironment of human embryonic stem cells. Stem Cells *24*, 501-505.

Ptak, C., and Petronis, A. (2008). Epigenetics and complex disease: from etiology to new therapeutics. Annual review of pharmacology and toxicology *48*, 257-276.

Pujadas, E., and Feinberg, A.P. (2012). Regulated noise in the epigenetic landscape of development and disease. Cell *148*, 1123-1131.

Rea, S., Eisenhaber, F., O'Carroll, D., Strahl, B.D., Sun, Z.W., Schmid, M., Opravil, S., Mechtler, K., Ponting, C.P., Allis, C.D.*, et al.* (2000). Regulation of chromatin structure by site-specific histone H3 methyltransferases. Nature *406*, 593-599.

Reisner, W., Morton, K.J., Riehn, R., Wang, Y.M., Yu, Z., Rosen, M., Sturm, J.C., Chou, S.Y., Frey, E., and Austin, R.H. (2005). Statics and dynamics of single DNA molecules confined in nanochannels. Physical review letters *94*, 196101.

Reisner, W., Pedersen, J.N., and Austin, R.H. (2012). DNA confinement in nanochannels: physics and biological applications. Rep Prog Phys *75*, 106601.

Rizzino, A. (2007). A challenge for regenerative medicine: proper genetic programming, not cellular mimicry. Developmental dynamics : an official publication of the American Association of Anatomists *236*, 3199-3207.

Rubtsov, M.A., Polikanov, Y.S., Bondarenko, V.A., Wang, Y.H., and Studitsky, V.M. (2006). Chromatin structure can strongly facilitate enhancer action over a distance. Proceedings of the National Academy of Sciences of the United States of America *103*, 17690-17695.

Sato, M.H., Ura, K., Hohmura, K.I., Tokumasu, F., Yoshimura, S.H., Hanaoka, F., and Takeyasu, K. (1999). Atomic force microscopy sees nucleosome positioning and histone H1-induced compaction in reconstituted chromatin. FEBS letters *452*, 267-271.

Schalch, T., Duda, S., Sargent, D.F., and Richmond, T.J. (2005). X-ray structure of a tetranucleosome and its implications for the chromatin fibre. Nature *436*, 138-141.

Schlick, T., Hayes, J., and Grigoryev, S. (2012). Toward convergence of experimental studies and theoretical modeling of the chromatin fiber. The Journal of biological chemistry *287*, 5183-5191.

Schmitz, R.J., Schultz, M.D., Urich, M.A., Nery, J.R., Pelizzola, M., Libiger, O., Alix, A., McCosh, R.B., Chen, H., Schork, N.J*., et al.* (2013). Patterns of population epigenomic diversity. Nature *495*, 193-198.

Smith, J.A., and Stocken, L.A. (1973). Identification of poly (ADP-ribose) covalently bound to histone F1 in vivo. Biochemical and biophysical research communications *54*, 297-300.

Takahashi, K., and Yamanaka, S. (2006). Induction of pluripotent stem cells from mouse embryonic and adult fibroblast cultures by defined factors. Cell *126*, 663-676.

Tamaru, H. (2010). Confining euchromatin/heterochromatin territory: jumonji crosses the line. Genes & development *24*, 1465-1478.

Tegenfeldt, J.O., Prinz, C., Cao, H., Huang, R.L., Austin, R.H., Chou, S.Y., Cox, E.C., and Sturm, J.C. (2004). Micro- and nanofluidics for DNA analysis. Analytical and bioanalytical chemistry *378*, 1678-1692.

Ueda, K., Omachi, A., Kawaichi, M., and Hayaishi, O. (1975). Natural occurrence of poly(ADP-ribosyl) histones in rat liver. Proceedings of the National Academy of Sciences of the United States of America *72*, 205-209.

Waldmann, T., and Schneider, R. (2013). Targeting histone modifications--epigenetics in cancer. Current opinion in cell biology *25*, 184-189.

Wang, H., Bash, R., Yodh, J.G., Hager, G.L., Lohr, D., and Lindsay, S.M. (2002). Glutaraldehyde modified mica: a new surface for atomic force microscopy of chromatin. Biophysical journal *83*, 3619-3625.

Woodcock, C.L., Frado, L.L., and Rattner, J.B. (1984). The higher-order structure of chromatin: evidence for a helical ribbon arrangement. The Journal of cell biology *99*, 42-52.

Worcel, A., Strogatz, S., and Riley, D. (1981). Structure of chromatin and the linking number of DNA. Proceedings of the National Academy of Sciences of the United States of America *78*, 1461-1465.

Wu, S.M., and Hochedlinger, K. (2011). Harnessing the potential of induced pluripotent stem cells for regenerative medicine. Nature cell biology *13*, 497-505.

Yeoman, L.C., Taylor, C.W., and Busch, H. (1973). Two-dimensional polyacrylamide gel electrophoresis of acid extractable nuclear proteins of normal rat liver and Novikoff hepatoma ascites cells. Biochemical and biophysical research communications *51*, 956-966.

Zentner, G.E., and Henikoff, S. (2013). Regulation of nucleosome dynamics by histone modifications. Nature structural & molecular biology *20*, 259-266.

Chapter 2

Guided crack generation with uniform spacing

The contents in this chapter have been adapted with minor modifications from the following publication: 'Guided fracture of films on soft substrates to create micro/nano-feature arrays with controlled periodicity', *Scientific Reports,* 2013

2.1 ABSTRACT

While the formation of cracks is often stochastic and considered undesirable, controlled fracture would enable rapid and low cost manufacture of micro/nanostructures. Here, we report a propagation-controlled technique to guide fracture of thin films supported on soft substrates to create crack arrays with highly controlled periodicity. Precision crack patterns are obtained by the use of strategically positioned stress-focusing V-notch features under conditions of slow application of strain to a degree where the notch features and intrinsic crack spacing match. This simple but robust approach provides a variety of precisely spaced crack arrays on both flat and curved surfaces. The general principles are applicable to a wide variety of multi-layered materials systems because the method does not require the careful control of defects associated with

initiation-controlled approaches. There are also no intrinsic limitations on the area over which such patterning can be performed opening the way for large area micro/nano-manufacturing.

2.2 INTRODUCTION

Fracture-induced patterns are ubiquitous in nature, and diverse patterns (Federl and Prusinkiewicz, 1996; Leung et al., 2001) are found in many inanimate objects such as dried mud and rocks. Cellular or hierarchical crack patterns are also observed on the surfaces of living creatures, occasionally determining appearances (Ball, 2011; Milinkovitch et al., 2013). In order to increase our understanding of these problems, the formation of crack arrays in multilayers has been extensively studied as a fundamental problem in fracture mechanics (Beuth, 1992a; Hutchinson and Suo, 1992; Shenoy et al., 2000; Thouless, 1990; Thouless et al., 2011a; Thouless et al., 1992; Ye et al., 1992). Using this knowledge of the theoretical background, artificial crack patterning on layered materials has been achieved for practical applications in micro/nano-fabrication (Adelung et al., 2004; Huh et al., 2007; Matsuoka et al., 2012; Mills et al., 2010; Zhu et al., 2005). Nevertheless, cracks are typically difficult to control precisely as a means of manufacturing, because they tend to initiate from random defects created during processing. Carefully-controlled conditions, such as those that can be obtained in a clean-room, are required to create systems in which any natural defects are small and few enough for fracture to be controlled by the subsequent deliberate introduction of artificial flaws (Meitl et al., 2007; Nam et al., 2012). While it has been shown that such an initiation-controlled approach can be used to control fracture patterns (Nam et al., 2012), this technique has only been applied specifically to materials in which intrinsic flaws are kept below a minimum threshold, and is not robust against accidental introduction of damage or use with soft materials. Here, we report an alternative and more general propagation-controlled approach for precision cracking of multi-layered materials; one that is relatively robust and not sensitive to the nature of the flaws in the system. While

our experiments focus on thin films supported by silicone elastomers, the general principles elucidated by the observations are applicable to a broad range of multilayered systems. To our knowledge, this is the first approach to control crack patterns by propagation control, rather than initiation control, and it is a technique that can also be used on multi-layered soft materials, not prepared under clean-room conditions.

2.3 METHODS

Saw-tooth structure design and device fabrication.

V-notch structures were fabricated using standard soft lithographic techniques. Patterns were designed in AutoCAD, and printed on transparent films (CAD Art inc.). SU-8 lithography was used to prepare a mold on silicon wafers. A 5:1 mixture of curing agent and PDMS (Sylard 184, Dow Corning) was mixed and cast against the molds, and were cured at 60℃ for at least 4 hours, before peeling the finished structures from the mold. Two different thin film layers were produced on the cured PDMS: i) plasma treated oxidized PDMS layer: the cured PDMS having the transferred microstructures were directly exposed to plasma treatment for 6 min at 200 W (COVANCE-MP, Femto-science inc.); ii) cured PDMS was coated with 10 nm of Cr layer first as a adhesion layer and then 40 nm of Au layer using e-beam deposition. A tensile strain was applied using specially designed stretchers.

Microscopy and image analysis.

The bright field images were acquired using a Nikon Ti-U microscope. Laser interferometer (LEXT, Olympus OLS4000) at 100x magnification was used to observe 3D images of cracks. The LEXT software was used to measure width, spacing, and depth of the cracks.

Strain rate dependent crack formation.

Defined strain rate stretching was performed using a programmed, electric stepping motor driven stretcher (Scholar Tec Corp., Osaka, Japan. Model: NS-500; a similar system is available from Strex ST-140). This system was used to compare crack formation between paired, un-paired, and alternating V-notch structures. Crack images were taken by an inverted microscope.

2.4 RESULTS

Guided fracture of thin films deposited on soft substrates

To investigate and demonstrate the concept of guided fracture, we designed parallel microgroove structures with opposing V-notch features, spaced up to 300 μm from each other (forming opposing saw-teeth structures). Polymer-"silica" and polymer-metal bilayer systems were fabricated using micro-patterned polydimethylsiloxane (PDMS) substrates, supporting a thin surface layer of oxidized PDMS (SiO_x, 200 nm thick (Mills et al., 2006)) or gold (Au, 40 nm on 10 nm chromium (Cr); Fig. 1a). (An adhesion layer of chromium was used to avoid delamination of the fold film during the formation of cracks in this system.)

We determined experimentally that notch lengths of 40 μm were suitable to initiate crack formation in these systems under a minimum applied critical strain (ε_c) (Fig. 1b). Since the notches are intended to activate existing intrinsic defects at their tips, and shadow defects at other locations, rather than introducing a region of significant stress concentration (Nam et al., 2012), the design of the notch angle was robust over a range of values (Fig. 2). Notch angles of 50^o were chosen for both systems presented in this work, because of the technical difficulties in fabricating an array of very sharp tips using SU-8 photolithography. It was found that an angle of 50^o provided the optimum balance of

ease-of-fabrication and generation of single cracks. All further experiments were performed using these parameters while varying the spacing, *d*, between them.

Earlier work has demonstrated that crack arrays are intrinsically much more dense for the SiO_x/PDMS system than they are for the Au/PDMS system, owing primarily to the significantly higher modulus of the Au (Douville et al., 2011; Mills et al., 2010; Thouless et al., 2011a) (See Supplementary Information for further discussion of fracture on gold film). In our case, the natural crack spacing with uniform stress applied in the Au/PDMS system was 340±180 μm, and 16.2 ± 8.3 μm in SiO_x/PDMS at 10% strain, consistent with analyses (Jiexi Huang, 2013). The spacing of our V-notches fell between these two natural crack spacings, explaining the differences observed between the two material systems studied. For example, the Au/PDMS system at 10% strain produced uniform cracks originating from the notch tips for all the spacings used (50 to 300 μm; Fig. 1c, Fig. 3, and Table 1). The SiO_x/PDMS system at a lower 6% strain, on the other hand, only formed uniform cracks with spacings ranging from 50 to 80 μm (Fig. 1d, Fig. 4, and Table 2). At larger spacings and strains, additional cracks were formed between notches (Fig. 5). The high modulus of the gold was also responsible for driving the cracks into the substrate, which also affected the crack spacing (Douville et al., 2011; Thouless et al., 2011a). The wrinkles that often formed at higher strains perpendicular to the cracks were generated by a Poisson's ratio effect (Efimenko et al., 2005). The uncracked region of the substrate induced a compressive strain in the cracked surface layer, where the stresses had been relaxed by the cracks. This compressive transverse strain was relaxed by buckling.

Three regimes of cracking.

Three regimes of crack formation were identified based on the level of applied strain (Fig. 6a and Fig. 7). In Regime I, at low strains below the threshold required to create uniform crack arrays, the ratio of the number of cracks to the number of V-notches

was less than 1. In Regime II, at intermediate strains, there was a 1:1 correspondence between the number of cracks and notches. At higher strains, in Regime III, additional cracks were generated between the notches. It is important to note that before entering Regime III, one crack formed from every notch tip.

As modeled (Jiexi Huang, 2013), in both Regimes I and III, the average crack spacing is similar to that obtained in systems without patterned notches. In Regime I, the thermo-dynamic spacing is larger than the spacing of the V-notches. In Regime III, the thermo-dynamic spacing is smaller than the spacing of the V-notches, and cracks can be initiated from intrinsic defects between notches. The range of strains over which Regime II can be obtained is dependent on the spacing between the notches, and is dictated by the strains corresponding to the inherent crack spacing that would be obtained in the absence of notches. Therefore, the link between the appropriate strain range and the notch spacing depends on the material properties of the system (Fig. 6b-c). Our experiments showed that a wider notch spacing reduces the strain range for Regime II and, while we were able to obtain a broad range of strains for Regime II in the Au/PDMS system, achieving the same strain range in SiO_x/PDMS would have required a much smaller spacing of V-notches.

Optimization of notch structure positioning and strain rates

Although uniform crack spacing was achieved in Regime II, individual cracks in paired notches occasionally generated multiple branches. Presumably, cracks simultaneously propagated from opposing sides and met to form misaligned cracks (Fig. 8a). To reduce the incidence of such imperfections, we tested un-paired notch configurations that initiate cracks from one side only. However, cracks starting from the notched side occasionally did not propagate to the other side; and intrinsic defects along the un-patterned side were occasionally activated and extended to the notched side (Fig. 8b). To address these imperfections, alternating notch structures were tested. This

configuration significantly improved crack quality, and cracks propagated only from the notches (Fig. 8c). The problem with paired notches is that each notch in a pair will be the same distance from a fully channeled crack. Cracks will be equally likely to propagate from either notch. A similar problem exists with notches on only one side. Since the notches only serve to control crack propagation, and shield flaws at neighboring sites, channel cracks can equally likely grow from the un-notched side as from the notched side. The advantage of the alternating notches is that each notch on each side provides a single site from which it is thermo-dynamically possible for a crack to channel at a given level of strain and current crack pattern.

Another fabrication parameter found to be useful for improving crack quality was the strain rate. A reduction in the applied strain rate improved quality of cracks formed particularly for the paired and un-paired notch features (Fig. 8d). This improvement is presumably because slow strain rates give cracks sufficient time to propagate across the specimen surface before fresh cracks were initiated from the opposite face.

Controlled fabrication of arrays with user-defined variable crack spacing

To demonstrate the versatility of this technique beyond uniformly spaced notches, structures with varying notch spacing were designed. Although with limits on the magnitude of notch spacing variability that could be accommodated, it was possible to generate arrays of cracks with variable spacing in both Au/PDMS and SiO_x/PDMS systems (Fig. 9a-d). The key is to maintain the applied strain and notch spacing such that the entire system stays within the cracking regime II (Fig. 6a). We did observe, as expected, that for a given strain, crack widths were larger in regions of increased notch spacing (Fig. 9a-b), owing to the larger stress that had to be accommodated by each crack. Rather than have notch features with uniform or gradually increasing spacing, the notch features could also be made to have irregular spacing (Fig. 9c-d). Increasing crack lengths with offset notch positions (Fig. 9e) or aligned notch positions (Fig. 9f) could be

generated in Au/PDMS (Fig. 9e) or SiO_x/PDMS system (Fig. 9f) to provide crack patterns over large areas. Additionally, arrays of width-adjustable cracks that are each several millimeters in length could also be obtained (Fig. 10a). Millimeter long cracks in the Au/PDMS system were sometimes observed to be branched; however, this was overcome by utilizing sequential arrays of diamond shaped notches which encourage the crack generation in both directions and connected each other without branching (Fig. 10b).

Controlled fracture on curved surfaces

We further utilized these principles to demonstrate fabrication of three dimensional, micro- and nano-sized patterns on multilayer soft polymer systems. (Fig. 11 and Fig. 12) Orientation of the crack patterns can be controlled by changing the applied forces. For example, a thin, Au/PDMS film (~1mm) was rolled and bonded into a cylinder by plasma treatment or a clip. The film was thin enough not to generate cracks during the rolling step. A hoop stress was gradually applied to the cylinder by the slow expansion of a compressed foam cylinder (Fig. 11a). The resultant cracks followed the designed notch pattern (Fig. 11b), demonstrating that this technique is potentially applicable to broader ranges of non-flat pattern fabrication.

2.5 DISCUSSION & CONCLUSION

It is important to realize that the situation considered in the current work, and the strategy for forming regular pattern is fundamentally different from that presented by Nam *et al*. for relatively "defect-free" material systems (Nam et al., 2012). The approach described in that work was one that relied on controlling the flaw population responsible for generating cracks. By careful processing, the intrinsic flaw population was kept so low that, in the absence of artificial flaws, the crack spacing would be much greater than

expected from the predictions of fracture mechanics. The introduction of artificial flaws then allowed control of the crack spacing, but always at spacings much larger than the thermo-dynamic equilibrium levels.

The mechanics of fracture can be broadly categorized into two situations: (i) the "defect-free" situation where there are few defects large enough to readily nucleate crack, and (ii) the situation where the number of large defects from which cracks readily propagate is not limiting. In the former situation, the limiting factor to initiate cracking is achieving sufficiently high stress. Thus, in such materials, cracks formation can be controlled by stress concentration without much concern for unintended crack formation. The challenge is creating materials with features that are sharp enough to create the level of stress concentration needed to form crack while maintaining the material devoid of any unintended damage or flaws. This type of defect-free materials requires careful fabrication techniques, often in a clean-room (Nam et al., 2012).

The alternative situation in which crack arrays are propagation controlled is more common. Here, the statistics of the flaw population do not play a significant role in determining the average spacing of arrays, and the spacing is determined primarily by the applied strain, the toughness and thickness of the film and the modulus of the film and substrate (Dundurs, 1969; Mills et al., 2010; Shenoy et al., 2000; Thouless et al., 2011a). Thus, in such materials, controlled crack formation relies on the shielding of crack propagation from unwanted sites, rather than actively initiating cracks from artificial flaws. Our current work falls under this latter category, and a detailed analysis of the interaction between the mechanics and the statistics of these two approaches has been presented elsewhere (Jiexi Huang, 2013).

To be more specific, whether intrinsic flaws might trigger random cracks to initiate would depend on the spacing between the V-notch stress concentrators and the intrinsic defect density. In our system, the notch spacing is much larger than the spacing between intrinsic flaws. Conversely, in the system described by Nam *et al*. (Nam et al., 2012), the "natural" crack spacing, which assumes abundant flaws, can be estimated as being about 4 μm, using the data given in that paper (Nam et al., 2012) and the analysis

of Thouless *et al*. (Thouless et al., 1992). This is much smaller than the notch spacing of 100 μm that was used in that study, and the fact that the notches resulted in a crack spacing much larger than the natural spacing indicates that a very low density of intrinsic flaws was achieved by the careful processing. The systems we present in this chapter are much closer to an equilibrium configuration. Therefore, the fabrication of uniform crack arrays requires not only creation of stress-concentrating features, but coordination of spacing between the features with the applied strain. The beneficial consequence of this design approach is that the crack patterns are stable against the introduction of additional flaws making it more robust and applicable to a broader range of materials and processing parameters including curved and 3D soft structures.

In summary, we demonstrate robust guidance of fracture in multilayer soft materials via selective activation of intrinsic defects based on matching spacing design and strain application with material properties of the system. In defect-rich materials such as utilized in this chapter, precision fracture fabrication requires undesired stress suppression first, then localized stress focusing to initiate cracks second. Here, we balance these two opposing requirements of stress relief and focusing using alternating V-notch features, slow strain rates, and most critically the use of a strain where the V-notch spacing matches the equilibrium average crack spacing of the material system under study. This simple and versatile approach achieves surprisingly precise micro- and nanoscale features in a variety of readily-processed materials and in a variety of geometries including curved surfaces.

2.6 ADDITIONAL DISCUSSION

Discussion on fracture on gold film

It should be emphasized that the fracture for both the oxidized film and the gold film were brittle in nature. All nano-scale thin metal films (including metals) are

inherently brittle (in the rigorous sense of the word used to describe the energy dissipated per unit area of crack advance), with a toughness that can be estimated approximately by the product of the thickness and yield strength as being less than about 50 J/m^2 for a 100 nm film. However, when the film is supported on a relatively stiff substrate, the energy-release rate for crack channeling is limited by the fracture mechanics, and the applied strain for crack channeling is about 5% (Beuth, 1992b; Hu et al., 1988), which tends to be higher than the yield strain. Conversely, if the film is supported on a very compliant substrate, the energy-release rate is much higher (Beuth, 1992b; Thouless et al., 2011b), and the strain required for crack channeling is lower, resulting in the observed brittle behavior on substrates such as PDMS. Furthermore, in the absence of a constraint, such as when the film is unsupported (Pashley, 1960) or supported on a very complaint material such as PDMS (Douville et al., 2011) fracture is initiated by shear localization at the onset of yield. The film deforms in an elastic fashion up to relatively high strains because of an elevated yield stress, and then catastrophically ruptures because of the shear localization. Only when a thin metal film is supported on a substrate with a reasonable modulus, capable of providing significant constraint to the deformation and reducing the magnitude of the energy-release rate for channel cracking, can ductile behavior be induced (Li et al., 2005).

FIGURES

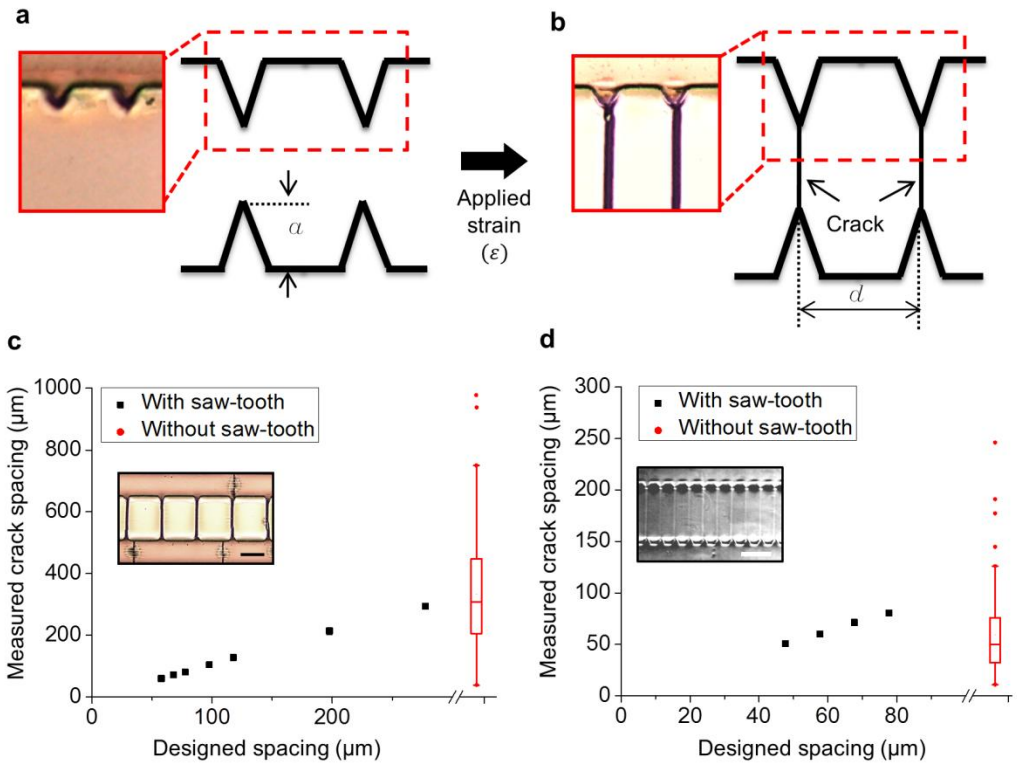

Figure 2.1 Guiding formation of periodic cracks with saw-tooth structures

(a,b) Optical images and schematics of multilayer structures fabricated with an array of V-notches, (a) before and (b) after cracks are generated by applied tension. Periodic cracks are produced along V-notches. (c,d) Crack spacing in a (c) Au/PDMS and (d) SiOx/PDMS bilayer system with different saw-tooth spacings as compared to a control measurement without saw-tooth structures at (c) $\varepsilon \sim 10\%$ and (d) $\varepsilon \sim 6\%$. Scale bar: 200 μm.

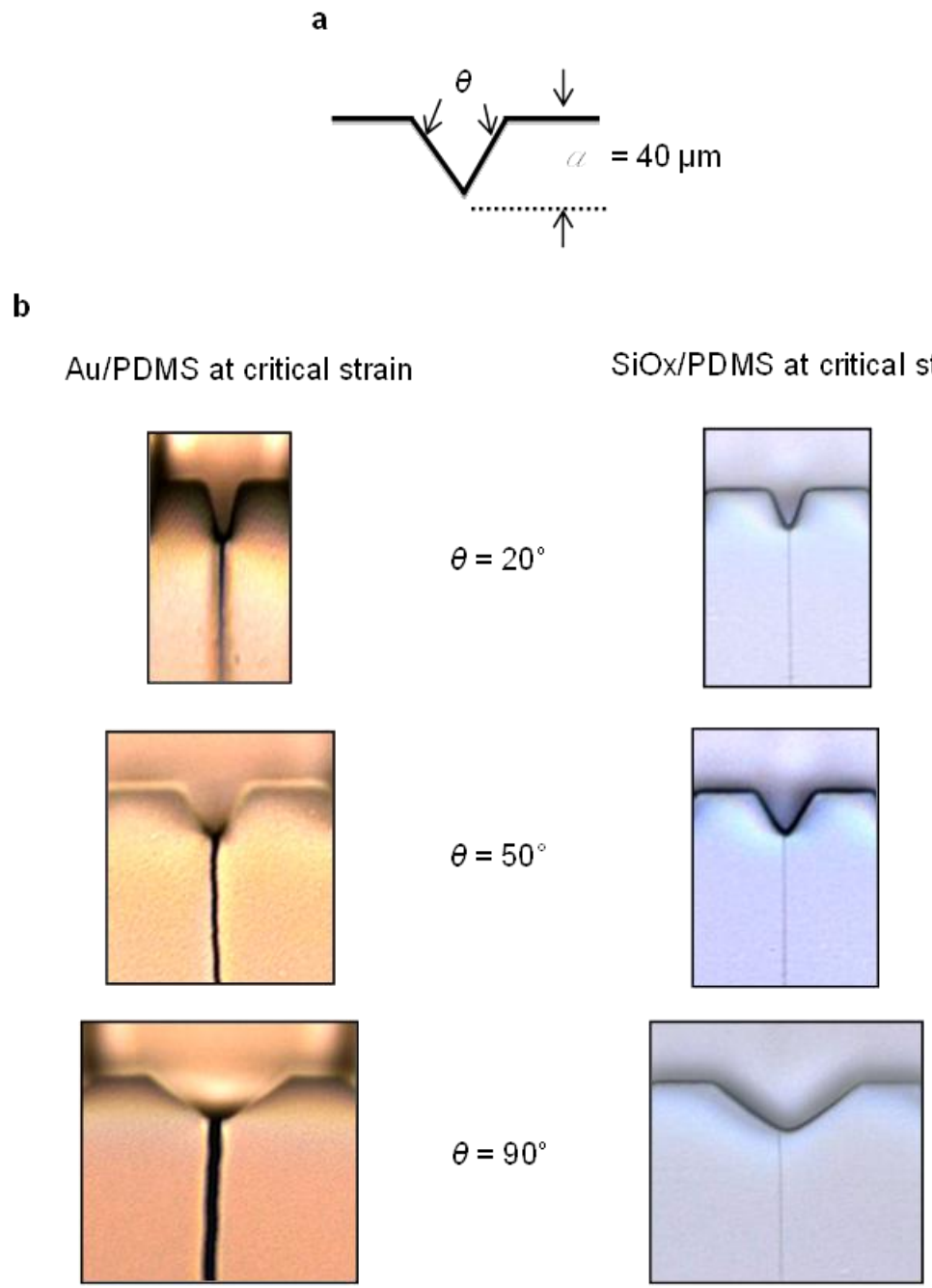

Figure 2.2 Cracking relatively independent of 'V-notch' angle

a, Schematics of multilayer structures with V-notches having different angles, θ. **b,** Crack formation in Au/PDMS and SiOx/PDMS bilayer systems under applied uniaxial tensile force. θ = 20°, 50°, 90° with a notch of fixed length a = 40 μm. but different anges.

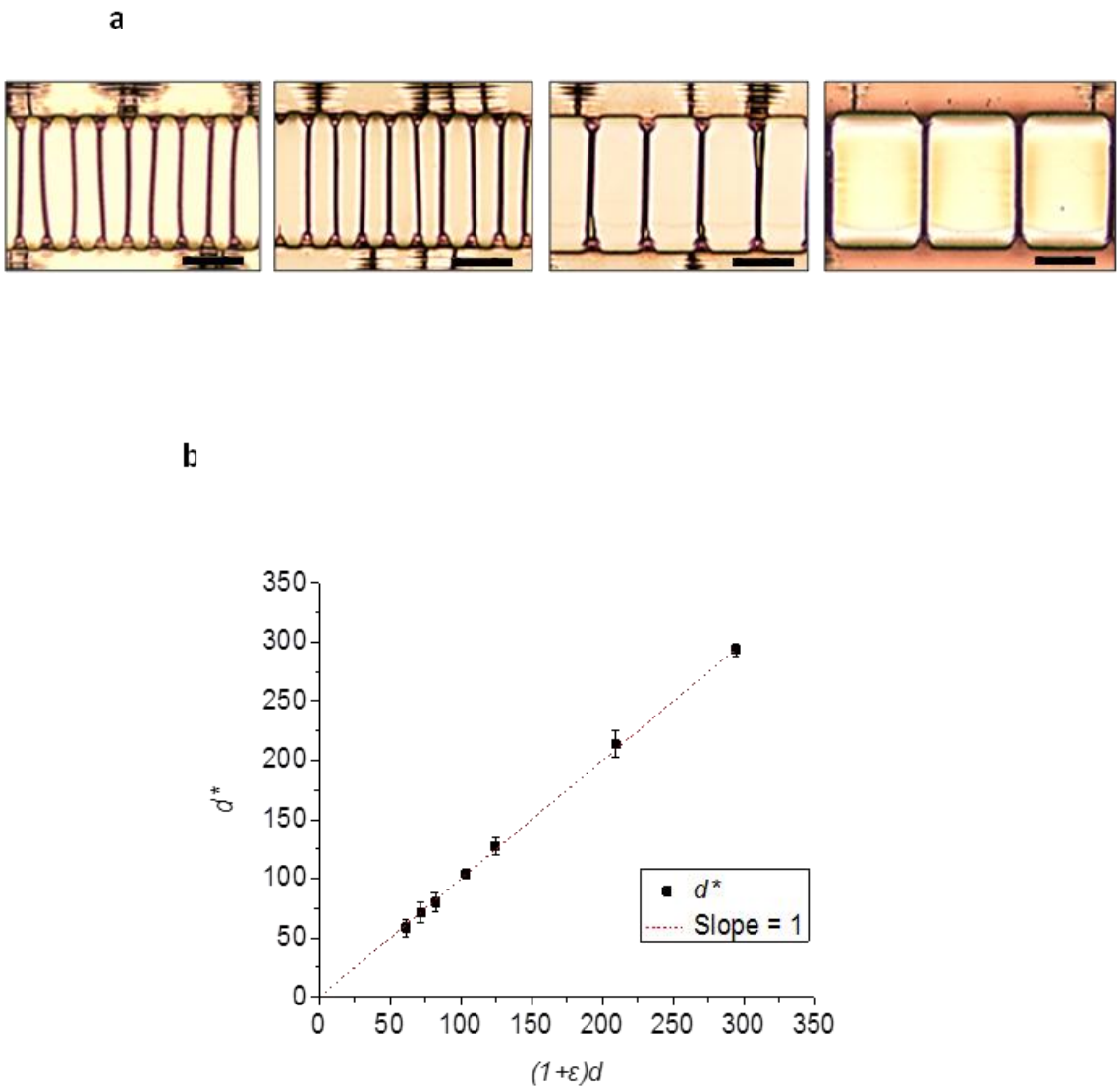

Figure 2.3 Periodic uniformity of cracking on Au/PDMS layer

a, Controlled spacing of the cracks on Au surface with different spacing between notches, d, (47.7 μm < d < 277.7 μm), Scale bar: 200 μm. b, Comparison of measured dimensionless crack spacing (d^*) and dimensionless spacing considering the applied strain,$(1+\varepsilon)d$ on Au/PDMS system at ε ~ 10%. The slope of the dash line ~ 1.

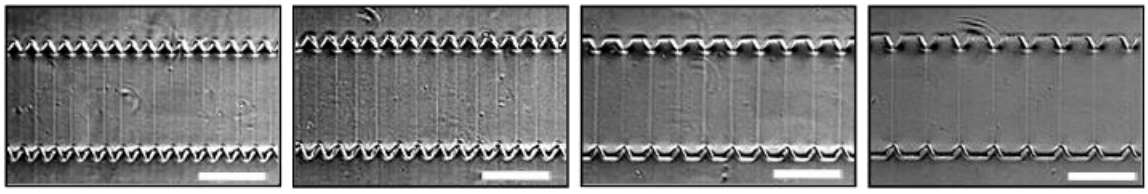

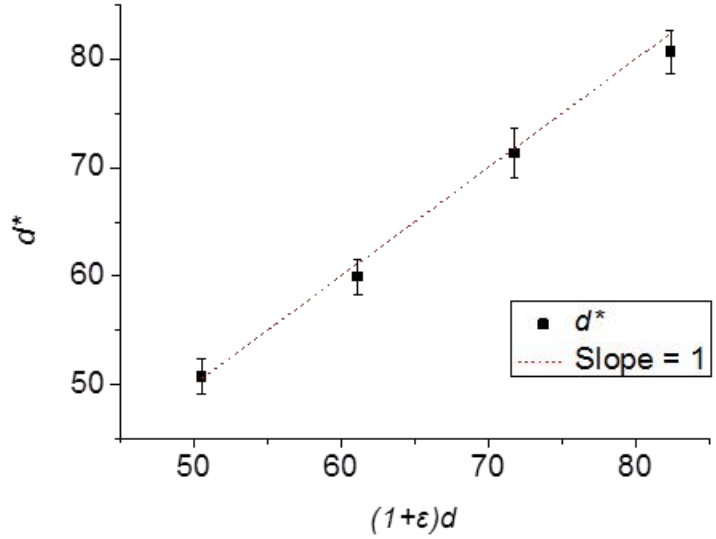

Figure 2.4 Periodic uniformity of cracking on SiOx/PDMS bilayer.

a, Controlled spacing of the cracks formed on oxidized PDMS surface as spacing between notches, d, was changed (47.7 μm < d < 117.7 μm), Scale bar: 200 μm. **b,** Comparison of measured dimensionless crack spacing (d^*) and dimensionless spacing considering the applied strain,$(1+\varepsilon)d$ on SiO_x/PDMS system at ε ~ 6%. The slope of the dash line ~ 1.

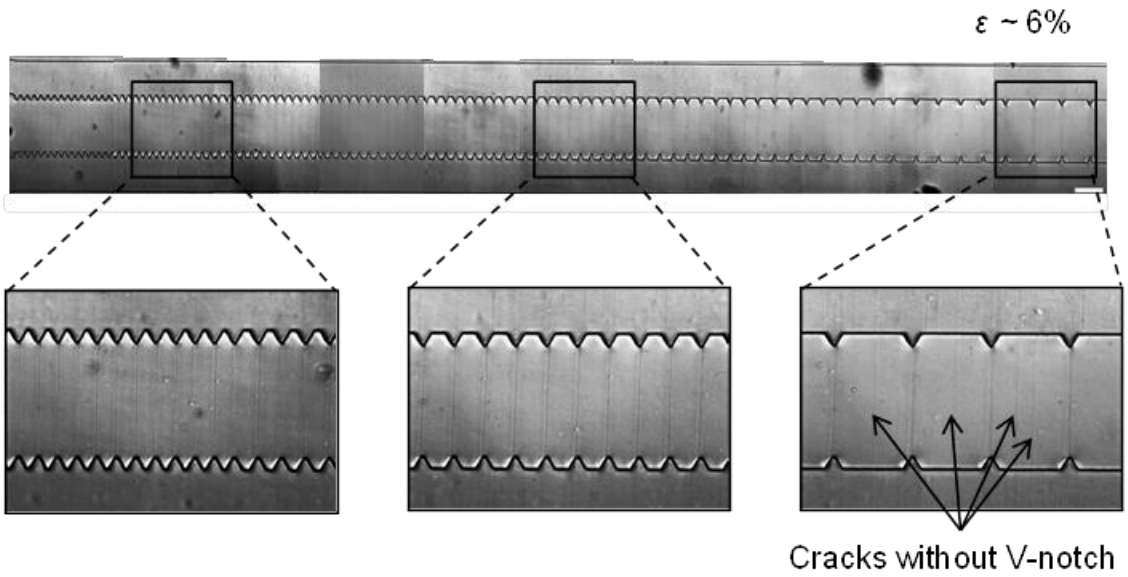

Figure 2.5 Crack formation on SiOx/PDMS systems that have different spacings between V-notches.

At a given strain condition, short spacing regions have uniformly periodic cracks, whereas cracks are formed at V-notches as well as randomly in regions between notches where the spacing between notches is larger. Scale bar: 200 μm.

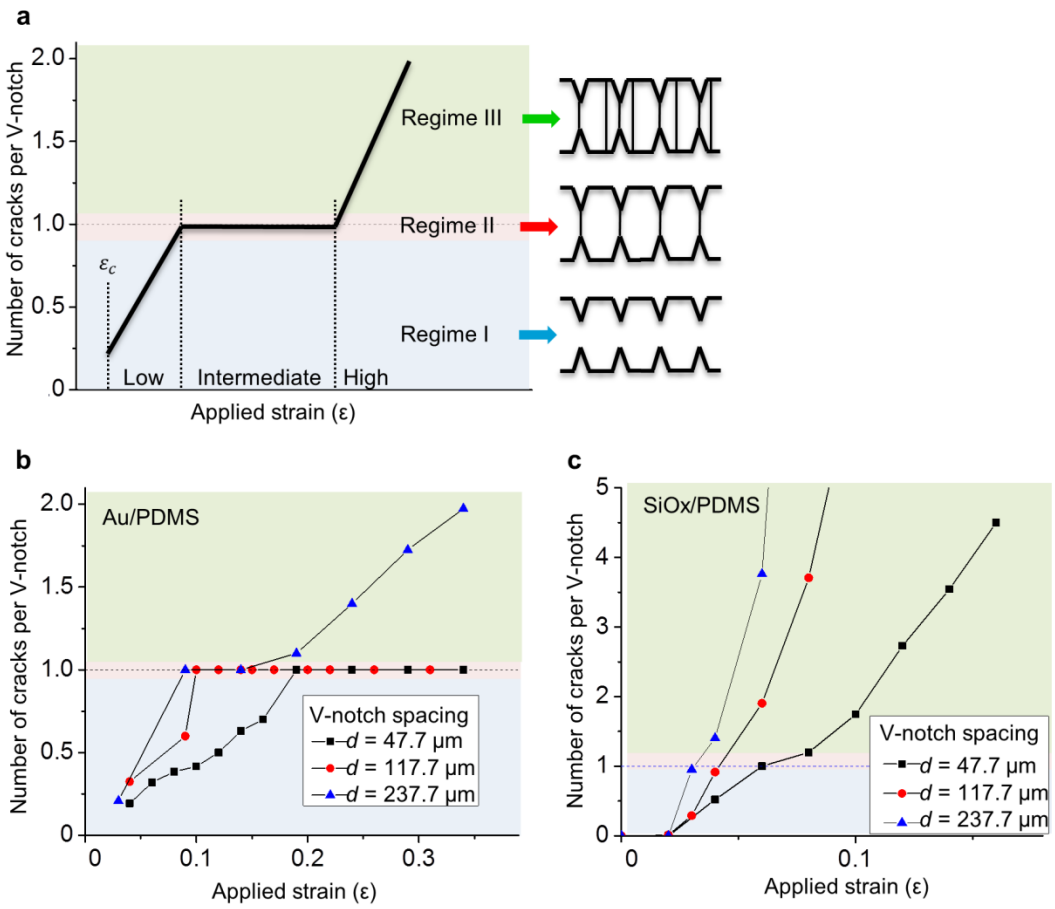

Figure 2.6 Regimes of cracking on thin film/PDMS layers.

(a) Schematic of cracking regimes relating crack positions with V-notch positions. In Regime (I) fewer cracks are observed compared to the number of notches (number of cracks per V-notch spacing is less than 1. In Regime (II), this ratio is equal to 1; and in Regime (III) the ratio is greater than 1. (b, c) Measured number of cracks per unit spacing depends on strain applied to the (b) Au/PDMS layer and (c) SiO_x/PDMS layer.

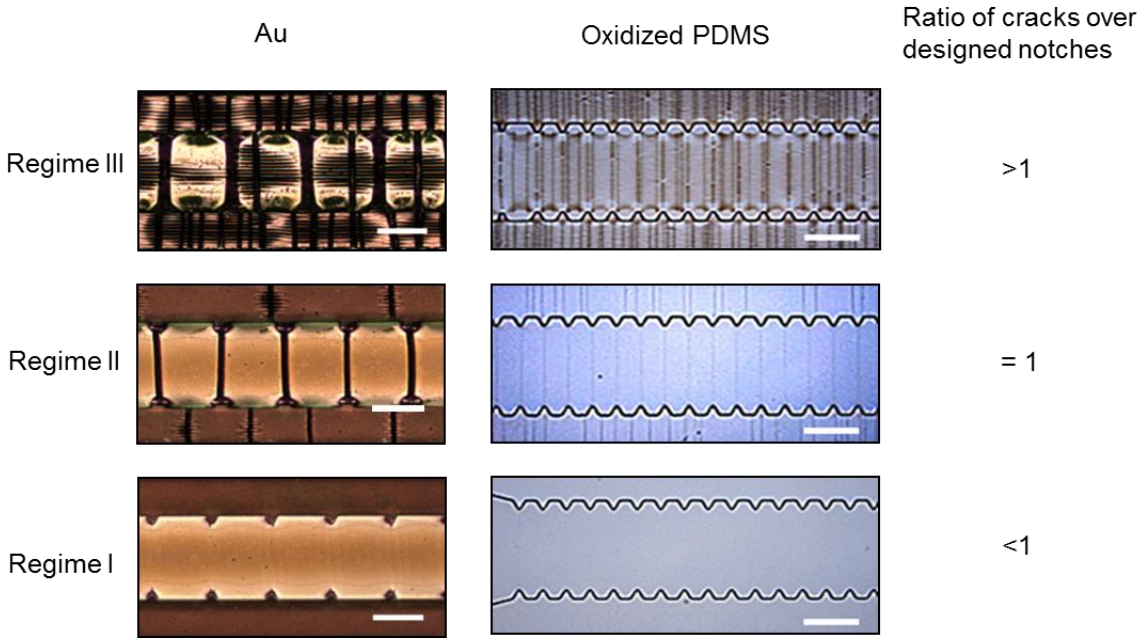

Figure 2.7 Representative images of Au/PDMS layers and SiOx/PDMS layers under different cracking regimes

Scale bar: 200 μm.

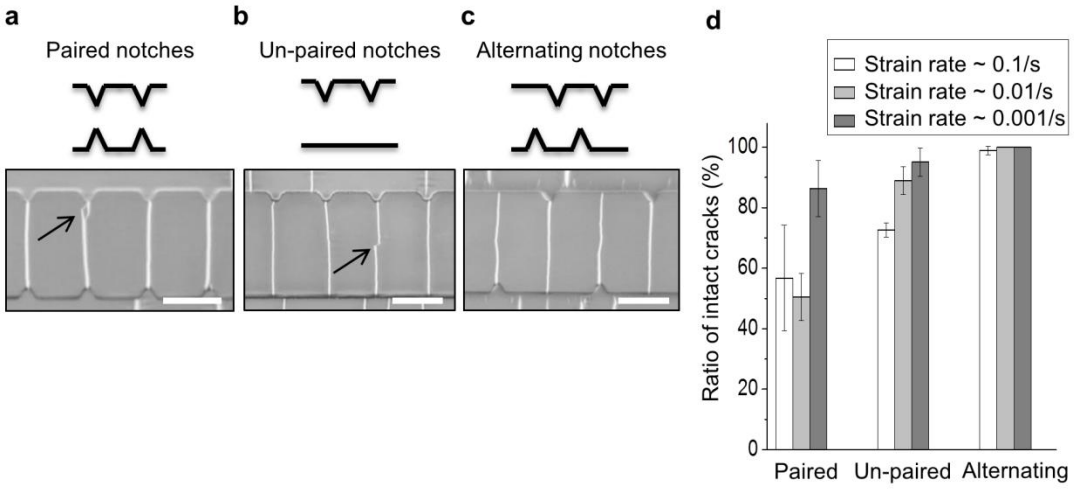

Figure 2.8 Optimal conditions for intact crack formation depend on structures of notches and strain rates.

(a) A branched crack formed on samples with paired notch features. (b) A disconnected crack on samples with un-paired notch features. (c) Only single, intact cracks form on samples with alternating notch features. (d) Intact cracks formation increases at lower strain rates ($\dot{\varepsilon}$ ~ 0.1/s, 0.01/s, and 0.001/s). Scale bar: 250 μm.

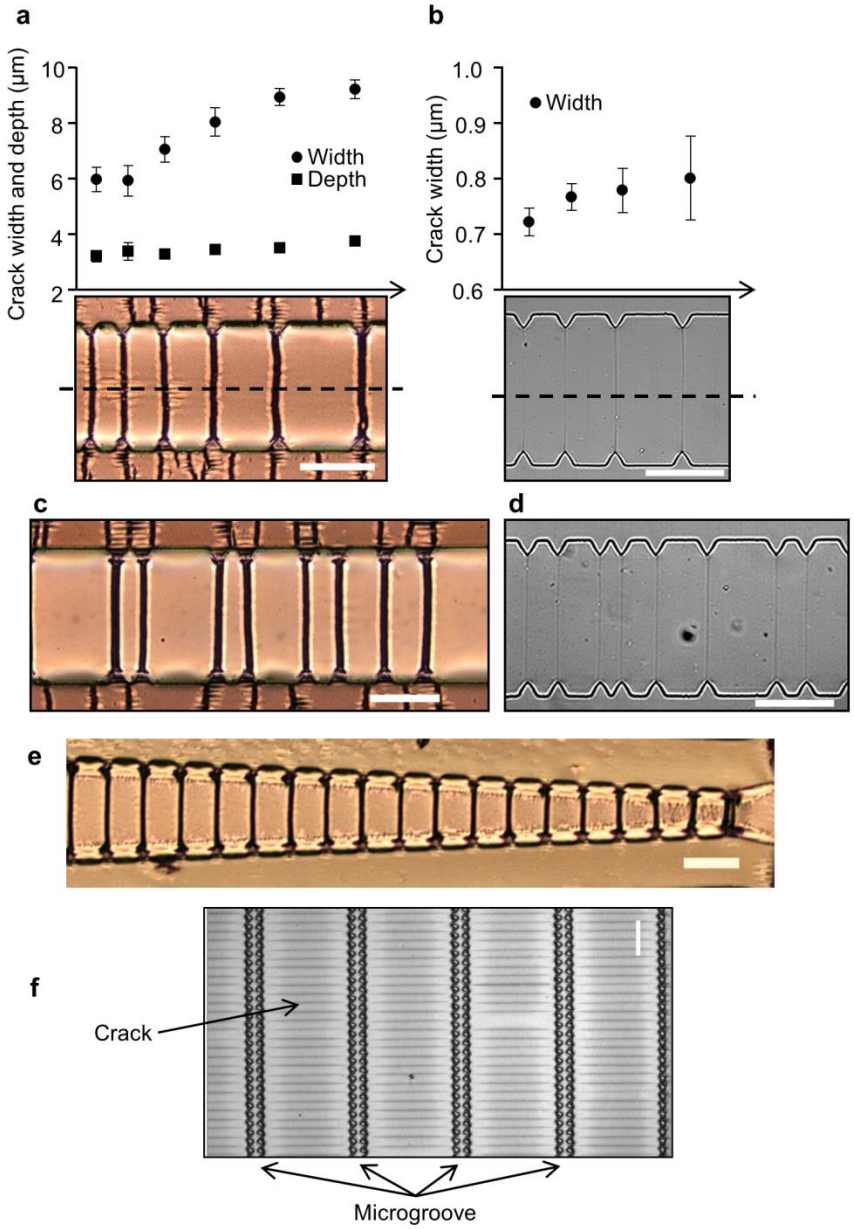

Figure 2.9 Controlled cracking on flat and curved surfaces.

(a,b): Crack dimensions in (a) Au/PDMS bilayers and (b) SiOx/PDMS bilayers vary depending on V-notch spacing. (c,d) Irregular periodic spacing can also provide precisely generated cracks. (e) Increasing crack lengths structures generated by controlled cracking of an Au/PDMS bilayer. (f) Nanocrack arrays extending several millimeters in lengths and centimeters widths formed on SiOx/PDMS bilayers. Scale bar: 200 μm.

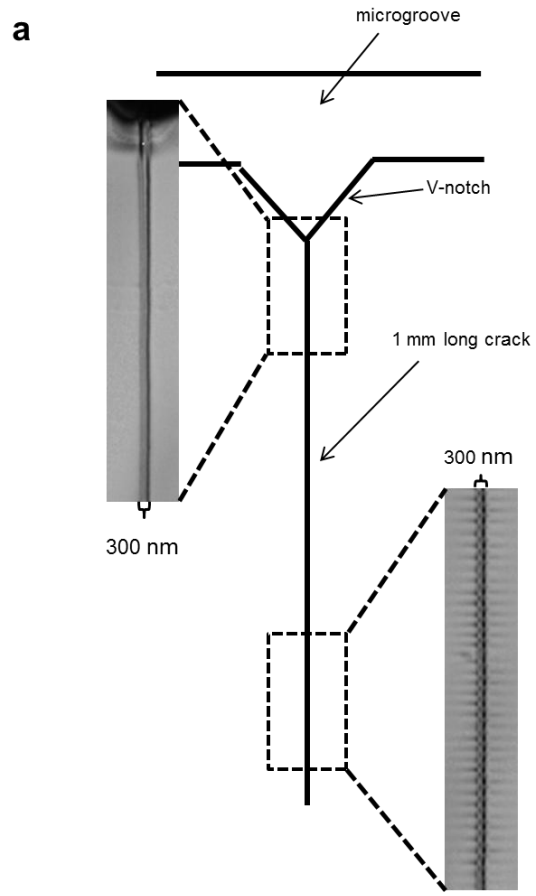

Figure 2.10 Millimeter long crack.

a, millimeter long and nano-sized crack in SiOx/PDMS system. b, arrays of millimeter long, micron sized cracks in Au/PDMS system with the help of ordered diamond notches.

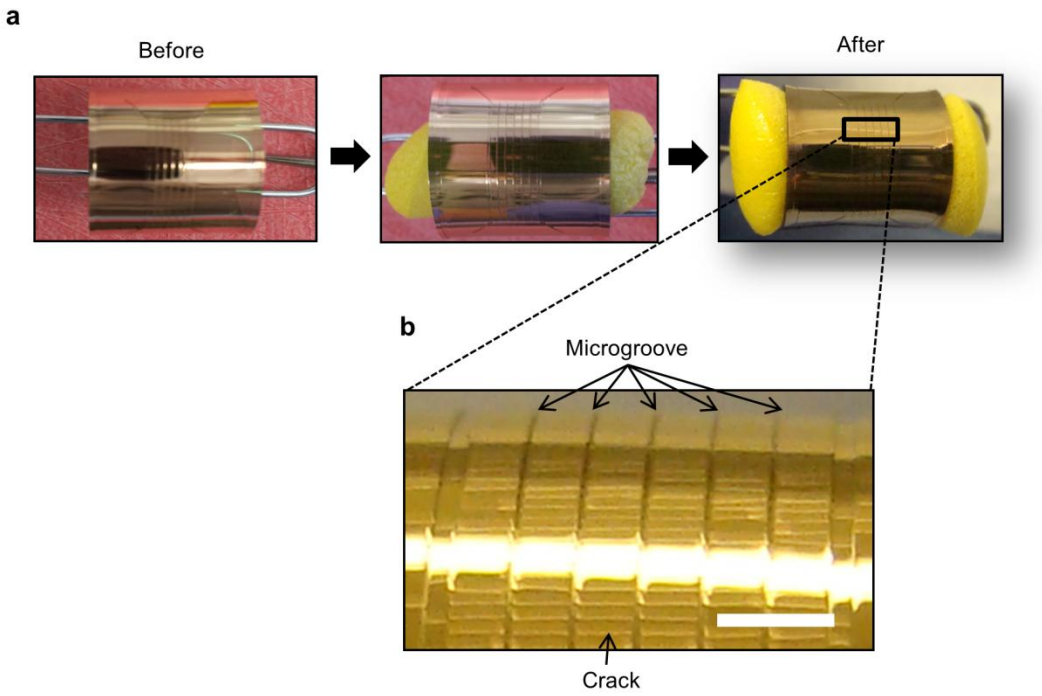

Figure 2.11 Three-dimensional micro- and nano sized patterns on multilayered polymeric system.

a, microgroove features with V-notches before cracking. b, patterned cracks on a rolled Au/PDMS sheet. A thin, rolled Au/PDMS sheet was stretched by radial stress resulting from expansion of a compressed foam cylinder. Scale bar: 1mm.

\

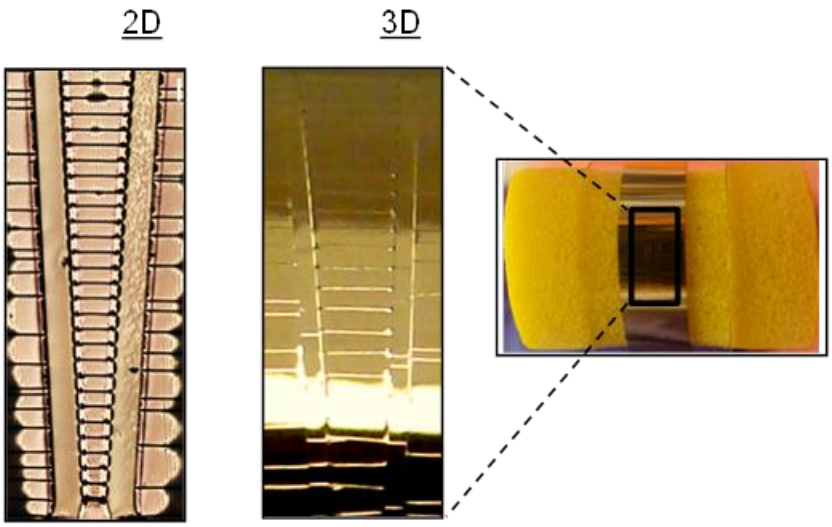

Figure 2.12 Uniformly spaced cracks patterns of different lengths formed on curved surface.

Demonstration of increasing crack lengths produced in a rolled Au/PDMS sheet on a foam cylinder. Cracks are formed from notches both on flat (*left*) and curved (*right*) substrate.

TABLES

Table 2.1 Statistical results of crack spacing on Au/ PDMS layer

Design spacing (μm)	**Control**	**57.70**	**67.70**	**77.70**	**97.70**	**117.70**	**197.70**	**277.70**
Spacing at $\varepsilon \sim 10\%$ (μm)	**-**	**63.47**	**74.47**	**85.47**	**107.47**	**129.47**	**217.47**	**305.47**
Average (μm)	**335.52**	**59.98**	**71.63**	**80.17**	**103.99**	**127.46**	**213.55**	**293.41**
S.D	**179.45**	**1.62**	**8.12**	**8.08**	**2.54**	**6.81**	**11.38**	**5.04**

Table 2.2 Statistical results of crack spacing on SiO_x/PDMS bilayer

Design spacing (μm)	**Control**	**47.70**	**57.70**	**67.70**	**77.70**
Spacing at $\varepsilon \sim 6\%$ (μm)	**-**	**50.56**	**61.16**	**71.76**	**82.36**
Measured spacing (μm)	**27.43**	**50.72**	**59.98**	**71.35**	**80.66**
Standard deviation (SD)	**16.97**	**1.63**	**1.62**	**2.35**	**1.97**

2.7 REFERENCES

Adelung, R., Aktas, O.C., Franc, J., Biswas, A., Kunz, R., Elbahri, M., Kanzow, J., Schürmann, U., and Faupel, F. (2004). Strain-controlled growth of nanowires within thin-film cracks. Nature materials *3*, 375-379.

Ball, P. (2011). Shapes: Nature's patterns: A tapestry in three parts, Vol 1 (Oxford University Press).

Beuth, J. (1992a). Cracking of thin bonded films in residual tension. International Journal of Solids and Structures *29*, 1657-1675.

Beuth, J.L. (1992b). Cracking of Thin Bonded Films in Residual Tension. Int J Solids Struct *29*, 1657-1675.

Douville, N.J., Li, Z., Takayama, S., and Thouless, M.D. (2011). Fracture of metal coated elastomers. Soft Matter *7*, 6493-6500.

Dundurs, J. (1969). Discussion:"Edge-Bonded Dissimilar Orthogonal Elastic Wedges Under Normal and Shear Loading"(Bogy, DB, 1968, ASME J. Appl. Mech., 35, pp. 460–466). Journal of Applied Mechanics *36*, 650.

Efimenko, K., Rackaitis, M., Manias, E., Vaziri, A., Mahadevan, L., and Genzer, J. (2005). Nested self-similar wrinkling patterns in skins. Nature materials *4*, 293-297.

Federl, P., and Prusinkiewicz, P. (1996). A texture model for cracked surfaces, with an application to tree bark. Paper presented at: Proceedings of Western Computer Graphics Symposium.

Hu, M., Thouless, M.D., and Evans, A.G. (1988). The decohesion of thin films from brittle substrates. Acta Metallurgica *36*, 1301-1307.

Huh, D., Mills, K., Zhu, X., Burns, M.A., Thouless, M., and Takayama, S. (2007). Tuneable elastomeric nanochannels for nanofluidic manipulation. Nature materials *6*, 424-428.

Hutchinson, J.W., and Suo, Z. (1992). Mixed mode cracking in layered materials. Advances in applied mechanics *29*, 191.

Jiexi Huang, B.C.K., Shuichi Takayama and M. D. Thouless (2013). The Control of Crack Arrays in Thin Films. Journal of Materials Science, (in press).

Leung, K.-T., Jozsa, L., Ravasz, M., and Neda, Z. (2001). Pattern formation: Spiral cracks without twisting. Nature *410*, 166-166.

Li, T., Huang, Z., Xi, Z., Lacour, S.P., Wagner, S., and Suo, Z. (2005). Delocalizing strain in a thin metal film on a polymer substrate. Mechanics of Materials *37*, 261-273.

Matsuoka, T., Kim, B.C., Huang, J., Douville, N.J., Thouless, M., and Takayama, S. (2012). Nanoscale squeezing in elastomeric nanochannels for single chromatin linearization. Nano letters.

Meitl, M.A., Feng, X., Dong, J., Menard, E., Ferreira, P.M., Huang, Y., and Rogers, J.A. (2007). Stress focusing for controlled fracture in microelectromechanical systems. Applied Physics Letters *90*, 083110-083110-083113.

Milinkovitch, M.C., Manukyan, L., Debry, A., Di-Poï, N., Martin, S., Singh, D., Lambert, D., and Zwicker, M. (2013). Crocodile Head Scales Are Not Developmental Units But Emerge from Physical Cracking. Science *339*, 78-81.

Mills, K.L., Huh, D., Takayama, S., and Thouless, M.D. (2010). Instantaneous fabrication of arrays of normally closed, adjustable, and reversible nanochannels by tunnel cracking. Lab Chip *10*, 1627-1630.

Mills, K.L., Zhu, X., Lee, D., Takayama, S., and Thouless, M.D. (2006). Properties of the surface-modified layer of plasma-oxidized poly (dimethylsiloxane). Mechanics of Nanoscale Materials and Devices *924*, 0924-Z0907.

Nam, K.H., Park, I.H., and Ko, S.H. (2012). Patterning by controlled cracking. Nature *485*, 221-224.

Pashley, D. (1960). A study of the deformation and fracture of single-crystal gold films of high strength inside an electron microscope. Proceedings of the Royal Society of London Series A Mathematical and Physical Sciences *255*, 218-231.

Shenoy, V., Schwartzman, A., and Freund, L.B. (2000). Crack patterns in brittle thin films. International journal of fracture *103*, 1-17.

Thouless, M.D. (1990). Crack spacing in brittle films on elastic substrates. Journal of the American Ceramic Society *73*, 2144-2146.

Thouless, M.D., Li, Z., Douville, N., and Takayama, S. (2011a). Periodic cracking of films supported on compliant substrates. Journal of the Mechanics and Physics of Solids.

Thouless, M.D., Li, Z., Douville, N.J., and Takayama, S. (2011b). Periodic cracking of films supported on compliant substrates. J Mech Phys Solids *59*, 1927-1937.

Thouless, M.D., Olsson, E., and Gupta, A. (1992). Cracking of brittle films on elastic substrates. Acta metallurgica et materialia *40*, 1287-1292.

Ye, T., Suo, Z., and Evans, A.G. (1992). Thin film cracking and the roles of substrate and interface. International Journal of Solids and Structures *29*, 2639-2648.

Zhu, X., Mills, K.L., Peters, P.R., Bahng, J.H., Liu, E.H., Shim, J., Naruse, K., Csete, M.E., Thouless, M., and Takayama, S. (2005). Fabrication of reconfigurable protein matrices by cracking. Nature materials *4*, 403-406.

Chapter 3

Fracture-based Fabrication of Normally-closed, Adjustable and Fully Reversible Micro-scale Fluidic Channels

The contents in this chapter have been adapted with minor modifications from the following publication: 'Fracture-based Fabrication of Normally-closed, Adjustable and Fully Reversible Micro-scale Fluidic Channels', *Small*, 2014

3.1 ABSTRACT

Adjustable fluidic structures play an important role in microfluidic systems. Fracture of multilayered materials under applied tension has been previously demonstrated as a convenient, simple and inexpensive approach to fabricate nano-scale adjustable structures; here, we demonstrate how to extend this concept to the micro-scale. We achieve this by a novel pairing of materials that leverages fracture mechanics to limit crack formation to a specified region, allowing us to create size-controllable and adjustable microfluidic structures. We demonstrate that this technique can be used to fabricate 'normally-closed' microfluidic channels that are completely reversible, a feature that is challenging to achieve in conventional systems without careful engineering

controls. The adjustable microfluidic channels are then applied to mechanically lyse single cells, and subsequently manipulate the released nuclear chromatin, creating new possibilities for epigenetic analysis of single cells. This simple, versatile and robust technology provides an easily accessible pathway to construct adjustable microfluidic structures, which will be useful in developing complex assays and experiments even in resource-limited settings.

3.2 INTRODUCTION

Adjustable fluidic structures are of critical importance in the control and manipulation of fluids at the microscale. The use of these structures as valves (Grover et al., 2003; Unger et al., 2000), flow controllers (Abate et al., 2009), and pumps (Gu et al., 2004) has significantly improved microfluidic throughput (Melin and Quake, 2007), automation (Sun et al., 2012), and sorting and trapping capabilities (Lenshof and Laurell, 2010), particularly for biological applications. However, fabricating adjustable structures is typically a challenging process, requiring unconventional fabrication techniques or precisely controlled actuation mechanisms. Given that biological applications generally require robust, reliable and precise control of microstructures, there exists a need for simple technologies that enable dynamic manipulation of micron-scaled features.

Previous work in our lab has focused on the fabrication of adjustable *nanoscale* fluidic channels by the formation of stable arrays of cracks in multilayered materials under applied tensile strains(Chantiwas et al., 2011; Dixon et al., 2014; Huh et al., 2007; Matsuoka et al., 2012; Uchida et al., 2009; Zhu et al., 2005). In these studies, a thin brittle layer of oxidized PDMS is sandwiched between two tough PDMS slabs, and fractured to form stable nanofluidic crack structures. This nanofabrication approach is simple, robust and versatile; we and others have used these technologies for various biomedical applications (Kim et al., 2014; Matsuoka et al., 2013). These have included the use of fractured nanofluidic channels to mechanically elongate DNA for epigenetic

analysis of chromatin (Matsuoka et al., 2012), and to sort and trap nanoparticles (Huh et al., 2007). An open crack configuration has also been used as adhesive protein matrices for cell culture (Dixon et al., 2014; Moraes et al., 2014; Zhu et al., 2005). While the utility of this nano-crack technology has been established for handling and patterning nano-scaled structures, the ability to extend this technology broadly into the micron-scale regime could be particularly fruitful. For example, such techniques would enable the transport of sufficient quantities of reagents to maintain and stimulate cultured cells: a prerequisite for most microfluidic cells-on-chip applications. In this work, we build on our previous experience with fracture-based fabrication techniques to develop a reliable and versatile system that generates predictable, adjustable and fully-reversible fluidic features at the scale of microns.

The characteristic dimensions of fracture-fabricated structures in oxidized PDMS / PDMS systems are typically limited to < 1 µm (Mills et al., 2008). This limitation arises because cracks formed in this system do not significantly tunnel into the underlying PDMS, and the crack depth is limited to the thickness of the oxidized PDMS. Fabricating oxidized layers thicker than 1 µm is challenging as the layer has a mismatched thermal coefficient with the substrate, and sample heating associated with the plasma oxidation process causes the spontaneous formation of undesired cracks (Béfahy et al., 2009; Tooley et al., 2011). Hence, it is challenging to use this system to extend the crack features beyond sub-micron dimensions.

An alternative approach, recently explored by our group (Cheng et al., 2013; Douville et al., 2011; Kim et al., 2013) and others (Adrega and Lacour, 2010; Lacour et al., 2003; Sun et al., 2012), is the use of a deposited metal layer of gold on bulk PDMS. The huge modulus mismatch with the PDMS substrate prompts the formation of cracks that tunnel into the PDMS. The depth to which these cracks grow is dependent on the distance between neighboring cracks, as well as on the applied strain and modulus/toughness mismatch between the materials (Thouless et al., 2011). Although this system may be used to generate micron-scaled crack structures, the crack dimensions cannot be reliably controlled, and exhibit broad variability. Moreover, this approach

requires physical vapor deposition systems available only in specialized cleanrooms, and the devices are not optically transparent, preventing use of these systems with conventional inverted microscopes.

In order to provide a versatile, tunable system in which crack fabrication can be used to generate a broad variety of structures at the micron scale, we present a novel material pairing that allows us to define the crack depth and width independently at this scale. Our strategy is based on preventing cracks from propagating into the substrate by selecting a material for the brittle layer with appropriate mechanical properties that can be deposited as a film of micron-scale thickness. hard PDMS (h-PDMS) (Schmid and Michel, 2000) is a variant of PDMS that can be spin-coated onto the PDMS substrate, and is brittle enough to initiate cracking. However, in contrast to gold, h-PDMS has a relatively small modulus mismatch with the substrate and, therefore, strongly localizes cracks to the surface layer. Hence, h-PDMS can be used to generate crack structures with well-defined dimensions at the micron-scale. We established that these structures are robust, adjustable, and completely reversible. We demonstrated the utility of this approach in designing 'normally-closed' adjustable microfluidic channels. We then used this technology to mechanically lyse and release chromatin from *single* cells for epigenetic analysis. This was achieved because of the unique capabilities of the system to allow a channel at the micron-scale to collapse all the way to a completely-closed configuration. By opening the channels to the micron scale, individual cells can be positioned within them. These cells can then be mechanically lysed by collapsing the micro-channels to release nuclear chromatin. Further collapse of the channels through the nano-scale induces elongational shear flow that linearizes the chromatin complex (Matsuoka et al., 2012).

3.3 METHODS

Multilayer sample preparation

PDMS elastomers were prepared and cured on glass slides whose surface had been rendered non-adhesive to PDMS by exposure to the vapor phase of the silanization agent (tridecafluoro-1,1,2,2-tetra-hydrooctyl)-1-trichlorosilane (United Chemical Technologies) for 30 minutes (Figure 1a). h-PDMS was prepared following established protocols (Odom et al., 2002). 3.4g of vinyl PDMS pre-polymer (VDT-731; Gelest Corp.), 18 μl of a platinum catalyst (platinum-divinyltetramethyldisiloxane, SIP6831.2, Gelest Corp.) and a drop of a modulator (2,4,6,8-tetramethyl-tetravinylcyclotetrasiloxane, 396281, Sigma-Aldrich) were mixed and degassed for several minutes. To initiate polymerization, one gram of a hydrosilane prepolymer (HMS-301; Gelest Corp.) was added; the system was mixed thoroughly and degassed for one minute. The h-PDMS was then diluted in hexane (20% or 50% w/w depending on the desired thickness) to reduce the viscosity of the fluid, and spin-coated onto the silanized glass slide, using different spin times and speeds to control the thickness of the h-PDMS layer. The relationship between film thickness, spin-time and speed was characterized using a laser interferometer (LEXT, Olympus OLS4000). Combinations of three different spin speeds (2000 rpm, 4000 rpm, and 6000 rpm) and four different spin times (30s, 60s, 120s, and 600s) were employed to generate films of various thicknesses. This layer was then partially cured in an oven at 120 ℃ for one minute to stabilize the liquid film.

Standard PDMS elastomer was prepared using a Sylgard 184 kit (Dow Corning) by mixing the monomer and cross-linking components in a 10:1 ratio. The resulting mixture was degassed, and cast to a thickness of 5 mm over the partially cured h-PDMS layer. The entire system was then cured at 60 ℃ overnight, before the h-PDMS / PDMS bilayer was peeled from the glass slide, and stored at room temperature until use.

Materials characterization

The Young's moduli of the PDMS and h-PDMS were measured using uniaxial tensile tests and compression tests. The tensile specimens were prepared by casting PDMS and h-PDMS in dog-bone shaped molds, following ASTM E1820-11e2. After release from the molds, the specimens were clamped in wedge grips. The tensile tests were performed at room temperature using an MTS 858 Bionix II tensile machine. The load was applied at a constant strain rate of 0.0080/s, and the load was measured using a 250 N load cell. The strains were determined using MetaMorph software to analyze the displacements of markers on the sample that had been recorded optically. True stress-strain curves were used to calculate the Young's modulus of each material.

The compressive tests were conducted using a TA XT-PLUS Texture analyzer, set up with a 30 kg load cell. PDMS and h-PDMS samples were cast and cured to a thickness of 5-10 mm in 22 mm diameter containers. A stainless steel spherical indenter of radius 6.35 mm was used to apply a deformation of 250 μm into the material. The resulting force-displacement curves were fitted to a Hertzian spherical indentation model to calculate the modulus of the material. For the compression tests, three indentation curves were generated from each of at least three independent samples, and averaged.

The toughness of the h-PDMS was measured using a tensile specimen with an edge crack that had been introduced by a razor blade. The crack was imaged optically during the tensile test. No sub-critical crack growth was observed, so the peak load and the original crack length were used to determine the toughness. The toughness of the standard PDMS was previously reported by Mills *et al.* using a compact-tension specimen (Mills et al., 2008).

Crack generation and analysis

After peeling from the glass slides, the multilayer samples were loaded into a MicroVice Holder (S.T. Japan USA LLC. FL, USA). The MicroVice is a microscope-compatible device capable of manually applying uniaxial strains to the sample. These applied strain generated the cracks used as micro-channels. Where orthogonal arrays of channels were required, biaxial strains were applied using a homemade biaxial stretching system, built by assembling the component parts of two MicroVice sample holders on a custom-fabricated acrylic plate. The applied strains were measured using digital calipers with a resolution of 0.01 mm, and the resulting crack dimensions were determined using a laser interferometer (LEXT, Olympus OLS4000). Recorded characteristics included the crack width and depth, and the average spacing between cracks.

Modeling crack deformation

The cross-sectional profiles of cracks in the h-PDMS / PDMS system were simulated using a hyperelastic material model in the commercially available finite-element analysis software ABAQUS (Dassault Systèmes). The model simulated a 7.2 μm thick layer of h-PDMS bonded to a 5 mm thick layer of PDMS, under applied strains of 25 and 35%. The depth of crack penetration into the PDMS layer was iteratively determined by fitting to the experimental data for the crack profile.

Fabrication of microfeatures within sealed bilayer structures

V-notch shaped stress concentrators (Huang et al., 2014; Kim et al., 2013) [21,28], arrayed diamond-shaped chambers, and micropatterned features for fluid flow were fabricated into the h-PDMS layer by spin-coating the h-PDMS layer onto a microfabricated SU-8 (Microchem) master structure fabricated on a silicon wafer using standard photolithography. After the h-PDMS layer was partially cured, a layer of

standard PDMS was cast over the mold and cured overnight at 60 ℃. The h-PDMS / PDMS bilayer was then carefully peeled from the mold, and stretched to generate cracks. The h-PDMS side of the bilayer was then plasma oxidized and placed in conformal contact with a similarly treated slab of cured PDMS and allowed to bond covalently, forming the PDMS / h-PDMS / PDMS sandwich structure.

To characterize the sealed channels, Rhodamine B solution was loaded into the microchannels so that the crack dimensions could be measured directly by confocal fluorescent microscopy. Alternatively, to avoid binding of hydrophobic dyes to the PDMS channel walls, a food-coloring dye was diluted in a mixture of water and ethanol, loaded into the channels, and imaged under varying degrees of strain.

Mechanical lysis of cells

HeLa cells were cultured in growth medium (Dulbecco's Modified Eagle Medium (DMEM) supplemented with 10% Fetal Bovine Serum and 1% antibiotics-antimycotics), and stably transfected to express a green-fluorescent H2B histone protein as previously described (Matsuoka et al., 2012). To conduct the lysis experiments, cells were trypsinized, centrifuged and resuspended at a density of ~10^5 cells/mL. Cells were loaded into parallel microchannels fabricated into the multilayered h-PDMS / PDMS material, and tension was applied in the same direction as the microchannels. Cracks connecting the microfluidic channels were generated, and single cells were driven into the cracked channels by slow flow. Once in the channels, the tensile strain was slowly released to pin and mechanically lyse the cell within the microfluidic channel. Cell lysis was confirmed by rapidly opening and closing the channel to generate elongational fluid flows (Matsuoka et al., 2012) and linearize the released chromatin. Linearized chromatin was visualized using standard fluorescent microscopy with a 40x objective.

3.4 RESULTS & DISCUSSION

Mechanical characterization of materials

h-PDMS is known to be stiffer and more brittle than conventional PDMS (Odom et al., 2002; Schmid and Michel, 2000). Tensile and compressive characterization tests confirmed these findings; the moduli were 3.7 ± 0.3 MPa for the PDMS and 9.2 ± 0.6 MPa for the h-PDMS. The mode-I toughness for the same PDMS used in this study was reported by Mills *et al.* (Mills et al., 2008) to be 460 ± 50 J/m^2. The toughness of the h-PDMS was determined to be 12.9 ± 2.7 J/m^2 (all mechanical characterization data are summarized in Table 1). These data of a comparable modulus and a reduced toughness for the h-PDMS compared to the PDMS are important because they mean that cracks in the multi-layer system will essentially be localized to the h-PDMS film layer, rather than propagating significantly into the underlying PDMS substrate (Beuth and Klingbeil, 1996; Thouless et al., 2011). Furthermore, the toughness of the h-PDMS is significantly higher than the toughness of the oxidized PDMS (0.1-0.3 J/m^2); this avoids the problems of spontaneous cracking from thermal mismatch that occurs with thicker oxidized films.

h-PDMS processing and biocompatibility

The ability to fabricate a thin film of a precisely defined thickness is an important feature in PDMS processing (Kang et al., 2013; Sun et al., 2012) and, in this particular application, the thickness of the h-PDMS is a critical parameter as it dictates the crack depth. Hence, the relationship between spin parameters and film thickness was carefully characterized for h-PDMS (Figure 2). As expected, spin speed plays a significant role in defining the film thickness, and the film thickness exponentially decreases towards a lower limit with spin time. The use of hexane as a solvent to reduce the viscosity and,

hence, the film thickness of h-PDMS was also characterized (Figure 3); but this was found not to make a substantial difference over the range of hexane/PDMS dilutions tested, particularly for longer spin times. This is likely caused by increased solvent evaporation during extended spin times. These results confirm that thin films of h-PDMS can be processed in a manner compatible with PDMS fabrication processes, and a range of film thicknesses from less than 1 µm to greater than 20 µm can be produced. For all further studies discussed in this chapter, a spin speed of 6000 RPM was used, and the spin times were varied to control the h-PDMS film thickness.

To ensure that h-PDMS retained the advantages of PDMS for any potential biological applications, we conducted a simple biocompatibility study to test cell adhesion to h-PDMS surfaces. Fibroblasts adopted well-spread morphologies after one day in culture (Figure 4), and showed no unusual phenotypes. This data strongly suggests that h-PDMS may be used without unusual surface modifications for biological cell-culture applications.

Characteristics of crack profiles

Cracks were formed in multilayered materials by application of mechanical force. Strains were applied to devices using a commercially available MicroVice stage. The use of a simple tensile stage to actuate adjustable microfluidic structures provides some significant advantages over other actuation technologies, such as pneumatic- or hydraulically operated devices. The stage is stable, robust, inexpensive, easily transported, independent of external power supplies, and bypasses the need for extremely robust world-to-chip connections, a common source of failure in conventionally operated microfluidic devices. Strains up to 60% could be applied to the PDMS samples without them breaking.

The average spacing between cracks, *S*, in systems without V-notches, but with different film thicknesses, *h*, were measured (under strain) to confirm that the cracks were limited to the h-PDMS film (Beuth and Klingbeil, 1996; Thouless et al., 2011). Although all data presented in this work were for cracks of length 5 mm, as dictated by the relevant width of the samples, we have demonstrated that crack lengths in excess of 10 mm could be generated (Figure 5). The length of the cracks appears to be limited only by the ability of the rig to apply uniform strains across the sample surface. As shown in Figure 6, the non-dimensional strain-corrected average crack spacing, $S/h(1+\varepsilon_o)$, scales with the non-dimensional parameter $\varepsilon_o(E_f h/\ \Gamma_f)^{1/2}$ (where ε_0 is the applied strain, and E_f and Γ_f are the modulus and toughness of the h-PDMS). This is the result expected from the fracture-mechanics of thin films when the crack depth is limited to the film thickness, and there is no delamination at the interface.

To quantify the degree to which cracks are localized to the h-PDMS, increasing levels of strain were applied to systems with different thicknesses of h-PDMS films, and the crack depth (distance from the center of the crack trough to the imaginary line connecting the crack tips) was quantified using laser surface profilometry (Figure 7A). The crack depth was found to be relatively stable up to 60% applied strain, at which point the supporting PDMS layer underwent catastrophic failure. Small changes in the crack depth and variations in crack profile at higher strains suggest that cracks do penetrate slightly into the underlying PDMS layer, but the degree to which this occurs is relatively small, consistent with the slightly larger modulus of the cracked layer (Thouless et al., 2011). Surface profilometry also revealed that the cracks had relatively flat profiles (Figure 7B, C; blue data points).

To confirm the mechanics underlying these dual observations of slight penetration and flat-bottomed crack profiles, numerical finite-element calculations were conducted. The relatively flat bottom of the crack profile suggests that the strain at the tip of the cracks was huge. Therefore the full stress-strain behavior of PDMS allowing for large deformations of the material was used in the simulations (Mills et al., 2008). The simulated penetration depth, *a*/*h*, was iteratively varied to give the best match to the

experimentally measured crack profiles. Comparisons between the simulation results and experimental measurements (Figure 7B, C) indicate that $a/h = 1.10$ at 25% applied strain and $a/h = 1.14$ at 35% applied strain. The small increase in penetration with a large increase in strain is consistent with experimental observations, and quantifies the close relationship between the thickness of the h-PDMS film and the depth of the generated crack. (It should be emphasized that even if a film is only slightly stiffer than a substrate, cracks are expected to extend slightly across the interface and into the substrate. However, consistent with the experimental observations, this penetration is expected to be insignificant for small modulus mismatches and tough substrates (Thouless et al., 2011).

To determine the reversibility of the system, the crack profiles were monitored using laser surface profilometry during cycles of applied load (Figure 8). These measurements revealed that the cracks appeared to have healed perfectly when allowed to close, with healing presumably associated with a physical attraction such as the van der Waals force. The complete reversibility of the system confirms that there was no delamination at the interface. This was further confirmed by experiments described in section 3.5, in which cracks formed in h-PDMS sandwiched between two PDMS layers were loaded with dye, and no apparent penetration into the interface is observed. Furthermore, cyclic strains were applied and released repeatedly; this resulted in fully-reversible and completely-closed cracks, without additional damage to the material.

Taken together, these results demonstrate that the depths of generated cracks can be fairly accurately controlled by specifying the thickness of the h-PDMS layer. Once a crack has been formed, its width can be controlled by varying the applied strain, both to open and close it. The fact that the crack dimensions can be varied in such a fashion suggests that this material system is suitable for the generation of well-controlled and adjustable micro-scale fluidic channels. In principle, even larger channels can be generated by thicker layers of hPDMS.

Predictive control of crack position and width

As is the case with conventional oxidized-PDMS / PDMS multilayer systems, it is challenging in the present h-PDMS/PDMS system to control precisely the location of individual cracks because of the statistical nature of the intrinsic flaws responsible for initiating channeling cracks (see the error bars in Figure 5). Since the width of a crack is sensitive to the distance to its nearest neighbors (Thouless et al., 2011), it is important to control the crack spacing if one wishes to control the crack width in adjustable microfluidic systems. Furthermore, control of crack location will be necessary in utilizing this approach for specific microfluidic applications. Therefore, we adapted an approach we developed recently to selectively activate intrinsic flaws in the h-PDMS material using microfabricated crack-initiating structures (Kim et al., 2013). To demonstrate this capability in the present system, we micro-fabricated V-notches spaced 700 µm apart and incorporated them into the h-PDMS layer. These notches shield intrinsic flaws from the applied stress field, leaving only the flaws at their tips to be active and available to initiate a crack at the desired level of strain (Huang et al., 2014). As a result, cracks channel across the film from the tips of these notches. For h-PDMS layers of 5-11 µm in thickness, cracks only formed at these pre-specified sites for applied strains ranging from 5 to 25% (Figure 9A). In order to prevent additional randomly positioned cracks, the design of the V-notch spacing can be adjusted according to the desired strains and thickness of the h-PDMS, as previously described (Huang et al., 2014; Kim et al., 2013). This simple demonstration indicates that the position of crack-generated microchannels can be specified *a priori* as part of the design process.

As expected, using the V-notch system to control spacing between cracks, allows the crack profiles to be controlled fairly accurately. The crack width can be controlled up to 50 µm, and depends upon the thickness of the h-PDMS film and the applied strain (Figure 9B). Some variation in widths on the spacing-controlled systems were observed with the h-PDMS / PDMS system possibly due to small localized variations in mechanical properties of the h-PDMS polymer layer. The widths of the cracks generated

in this system are of the same order of magnitude as those needed for many microfluidic devices, indicating that this system may be useful for a number of applications in developing adjustable microfluidic channels and systems.

Design of normally closed microfluidic systems

To demonstrate the potential applications of this system to the development of adjustable micro-scale fluidic platforms, we fabricated a simple geometrically-controllable and fully-reversible microfluidic channel. To achieve this, a pre-cracked brittle h-PDMS / PDMS bilayer was sealed against a PDMS slab (Figure 10A). Applied tension enlarges the cracks in the sandwiched layer, enabling control of crack width by varying the applied strain. A fluorescent solution of Rhodamine B was passed through the crack structures to enable clear visualization of channel dimensions (Figure 10B) and cross-section (Figure 10C). The crack cross-section follows the expected profile shown in Figures 7 and 8. Vertical asymmetry in the channel profile is due to the fabrication procedure: cracks were generated in the h-PDMS / PDMS bilayer first, before bonding the second PDMS layer to seal the channel, resulting in a flat profile on one side, and a parabolic profile on the other. Additional experiments in which the cracks were generated after forming the tri-layer showed the symmetry in the confocal images expected for two crack tips (data not shown).

Releasing the applied strain drove the dye out of the system. In the case of non-adsorbing dyes, such as food coloring in water (Figure 10D), the liquid was completely removed from the channel and could no longer be detected by image analysis (Figure 10E). Hence, microfluidic channels that are normally closed and completely reversible can be fabricated using this technique.

The ability of the system to completely heal a generated crack is of particular importance in applications that typically require microfluidic valves. Typically, valve structures require complex fabrication procedures to create hemispherical channels

(Unger et al., 2000) or bell-shaped channels (Futai et al., 2004; Lai et al., 2013) to allow the deformation of one of the channel walls to form a leak-proof seal. Such valves provide significant advantages such as highly-localized actuation capabilities, but are also challenging to mass produce, requiring careful alignment techniques or workarounds (Moraes et al., 2009), expensive operating equipment, and specialized expertise in multilayer soft lithography (Melin and Quake, 2007). While the fracture-fabricated adjustable microchannels presented in this work cannot provide highly localized and individually addressable valve actuation, they may significantly improve the fabrication process and workflow for applications involving simultaneous operation of multiple valves. To demonstrate the potential of this technology in such applications, we fabricated diamond-shaped cavities within the h-PDMS layer (Figure 10F). The cavities simultaneously direct the formation of cracks through stress concentration, and can serve as reaction chambers or compartments. Either rows or columns of chambers can be connected serially via uniaxial applied strains, or simultaneously connected across all rows and columns via biaxial strains. Furthermore, our micro-scale structures heal completely once the applied strain is removed, without the specialized fabrication considerations and operating equipment required in most systems requiring microfluidic valves. This ability to selectively address and compartmentalize rows or columns of reaction chambers may be applied to various microfluidic applications, such as single-cell trapping for analysis or culture, high-throughput reaction screens, or for analytical applications requiring single-molecule compartmentalization.

The relatively flat-bottomed crack profiles observed (Figure 8, 10C) may also be a significant advantage in many microfluidic applications. Cracks in this h-PDMS / PDMS system display a more rectangular shape than the sharp parabolic profiles demonstrated in gold / PDMS systems (Douville et al., 2011). This may be of importance for applications involving microscopy, particularly of cultured cells. The presence of a flat culture surface would enable simple microscopy-based image collection and analysis of cells cultured in the adjustable microfluidic structures. In contrast, parabolic crack profiles present potentially undesirable and undefined topographical cues to cultured cells,

and necessitate the use of complex and expensive analytical tools and equipment such as confocal or autofocusing microscopes. The flat culture surfaces also simplify calculations and modeling of fluid flow for potential studies involving the application of flow-induced shear stress on cultured cells (Moraes et al., 2011).

Although the characterization data presented in Figures 1 and 9 is limited to relatively small microfluidic channels, the working principles of this technique are applicable to generate a wide variety of channel dimensions. Beyond the specifications of the present system, silicones that can support greater ultimate tensile strains may be used to generate wider channels. The h-PDMS may be processed into thicker layers to create deeper channels, and may be blended with other polymers to increase material toughness and reduce any unintentional cracking during sample handling. Furthermore, the methods used in the preparation of these substrates are compatible with recent interest in DIY (do-it-yourself) "garage microfluidics", and the ability to conduct microfluidic experiments with minimal equipment, training and facilities. Replacing oxidized PDMS with h-PDMS as the brittle layer eliminates the need for expensive and specialized plasma oxidation systems, and adjustable microfluidic channels can be fabricated using a spin-coater and a weigh scale to measure PDMS and h-PDMS components. While we chose to spin-coat the h-PDMS layer onto the PDMS slabs, this process can easily be replaced by the industrially-used spreading process, in which the h-PDMS is coated on the surface and smoothed with a blade; a procedure which does not require specialized equipment, and can be done by hand. Hence, this procedure is applicable in a variety of contexts, including resource-limited settings. Finally, because the h-PDMS layer is mechanically tougher than oxidized PDMS layers, it is experimentally easier to handle the substrates without causing undesired cracking due to unintentional mechanical deformation, making this technique both reliable and experimentally simple.

Application: Mechanical lysis of single cells and manipulation of nuclear chromatin

As a first demonstration of the unique utility of this technology to biological studies, we used the normally-closed micro-scale fluidic channels to mechanically lyse individual cells and manipulate the chromatin released from the nucleus, for subsequent epigenetic analysis of single cells. This process is demonstrated in Figure 11. The PDMS / h-PDMS / PDMS system enables the generation of channels that can be reversibly opened to widths of 10s of microns, and these channels are large enough to accept a dilute suspension of single cells. Once a single cell is positioned in the channel, the channel is collapsed by slowly reducing the external tension on the device. The collapsing channel walls pin, compress and lyse the cells, releasing the chromatin complex from the cell nucleus. The channel is then opened and rapidly closed, generating elongational squeezing flows that linearize the released chromatin (Figure 11). As discussed in our previous work (Matsuoka et al., 2012), elongational flows along one dimension of a channel as well as simultaneous constraints presented along the other two dimensions are necessary to linearize chromatin. These dynamic mechanical constraints cannot be replicated in conventionally deformable mechanical lysis chambers, which are hence unsuitable for the structural manipulation of chromatin (Kim et al., 2007). For visualization purposes, the cells used in this demonstration have been transfected to stably express fluorescently labeled histones (H2B) in the chromatin complex. While the degree of chromatin linearization relative to its contour length is small in this initial demonstration, it is noted that we have previously demonstrated the ability to linearize chromatin strands to a greater degree using nanoscale fracture-based channels (Matsuoka et al., 2012). However, this previous nanoscale chromatin linearization study (Matsuoka et al., 2012) required chromatin materials from many cells to be pooled together to allow for liquid handling needs. The ability to construct both microscale and nanoscale channels by fracture opens the way for future studies with devices that integrate microscale single-cell lysis followed by nanoscale chromatin linearization and mapping, to study the epigenetic structure of chromatin at the single-cell level. Such approaches

are particularly valuable in studying stem cells and other rare cell populations, and may provide significant advantages over conventional chromatin immunoprecipitation (ChIP) assays that require many cells and evaluates one histone modification at a time (Matsuoka et al., 2013).

3.5 CONCLUSIONS

The use of hard PDMS (h-PDMS) as a brittle layer in multilayered structures for crack fabrication provides distinct advantages over more conventionally used oxidized PDMS or metal systems. While the use of cracking in multilayered materials under tension has previously been proposed as a novel nano-fabrication paradigm, significant challenges exist in defining *micro*-scale dimensions of cracks in bilayer material systems. h-PDMS can be processed into a layer of defined thickness at the micron length scale by spin-coating, and produces an array of stable flat-bottomed cracks under tension when supported on an underlying tough PDMS substrate. The toughness mismatch between h-PDMS and PDMS is large enough to generate stable crack arrays at relatively low strains, yet the modulus mismatch is small enough to strongly localize the cracks to the h-PDMS layer. Hence, the crack depth can be controlled based on the thickness of the h-PDMS layer. Microfabricated crack-initiating structures can be introduced into the material, enabling the precise positioning of cracks in this system. The crack width can also be tuned by varying the applied strain. In this way, precisely defined crack dimensions can be prescribed and realized. We have successfully demonstrated the use of this technology to create adjustable, completely-reversible and normally-closed microfluidic channels; a particularly challenging structure to fabricate using conventional approaches. We then demonstrated a simple biological application of the system by using the micro-scale adjustable channels to mechanically lyse single cells, and release and manipulate chromatin. This application requires micron-scale channels capable of accepting single cells, and the ability to completely close the channels to ensure mechanical lysis; features

that cannot be robustly achieved using existing material bilayer systems. The technologies presented in this work are simple, scalable, inexpensive and require relatively little microfabrication experience, enhancing the potential for microfabricated systems to be used by non-specialists in the microfluidics and precision-fabrication fields.

FIGURES

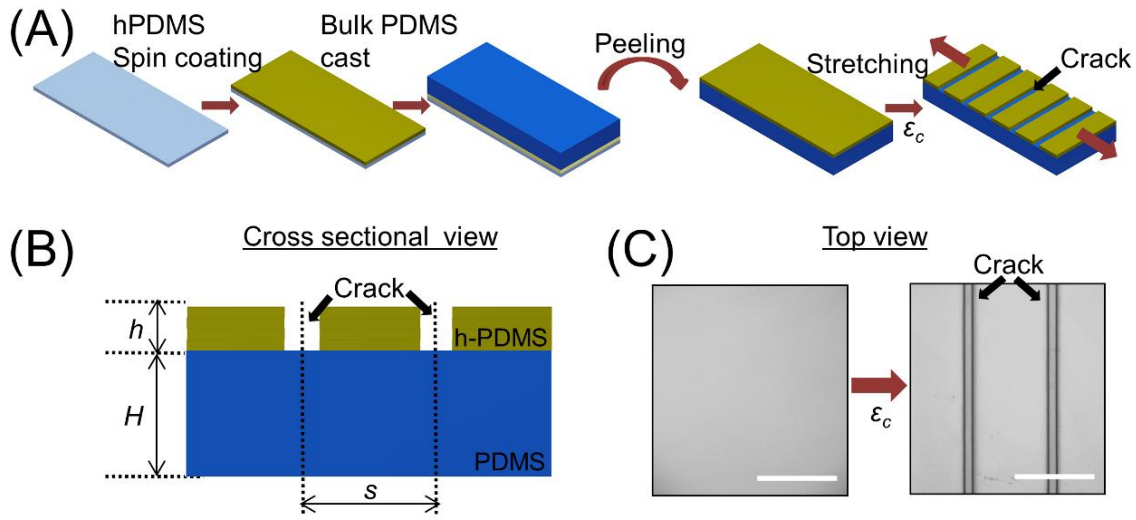

Figure 3.1 Experimental schematic.

(A) The fabrication process. A thin h-PDMS layer is spin coated onto a silanized glass slide and partially cured. PDMS is then cast on top of the film and fully cured. The bilayer is peeled away from the glass slide, and stretched to generate an array of cracks. (B) The dimensioning nomenclature. The thickness of the h-PDMS layer and bulk PDMS are denoted by *h* and *H* respectively, and the crack spacing *s* is measured from center to center of the troughs. (C) A representative bright-field image of crack formation in the substrate under an applied strain. Scale bar = 50 μm.

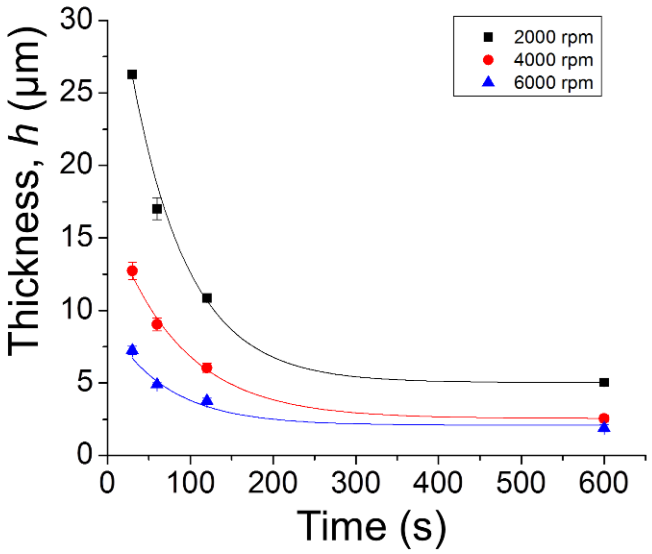

Figure 3.2 Characterization of spin coating parameters on h-PDMS thickness (*h*).

Spin speeds were varied from 2000 to 4000 RPM for between 30 seconds and 10 minutes. This domain of parameters produces films that range from < 1 µm to 27 µm in thickness.

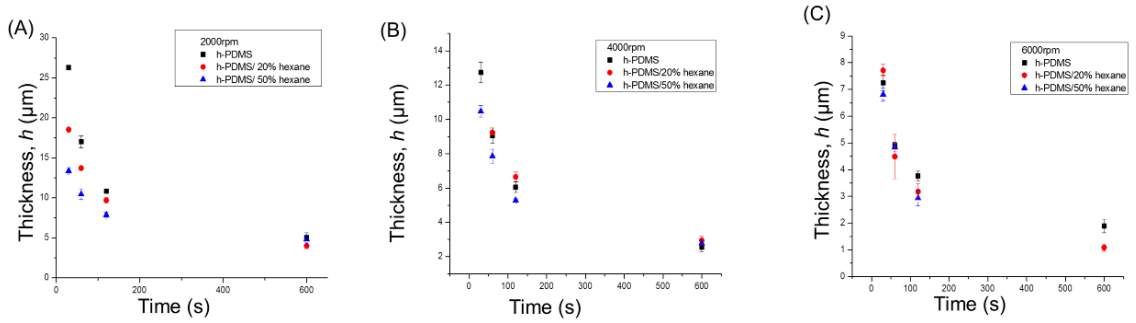

Figure 3.3 The thickness of spin-coated hPDMS films

can be manipulated by diluting the h-PDMS in hexane. The decreased viscosity of the prepolymer enables thinner films. These thinner films are not significantly different over long spin times owing to increased solvent evaporation during the spin-coating process.

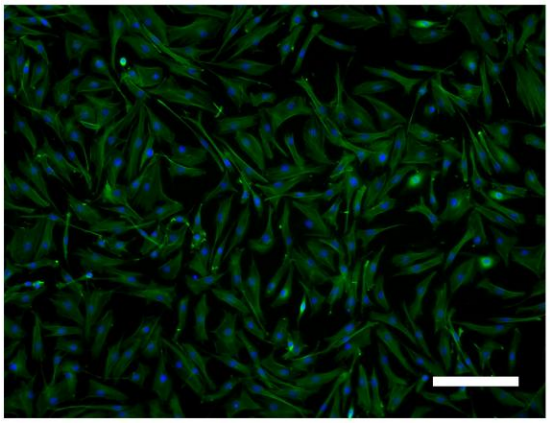

Figure 3.4 Biocompatibility of h-PDMS surface.

To demonstrate biocompatibility of the surface, NIH 3T3 cells were plated onto the h-PDMS surface in fully supplemented Dulbecco's Modified Eagle Medium (DMEM, supplemented with 10% fetal bovine serum, 1% antibiotics-antimycotics). Fibronectin (FN) extracellular matrix protein was used as an adhesive layer by incubating with 10 µg/mL FN (Sigma) for 30 minutes, prior to cell seeding. After one day in culture, the cells were fixed, and fluorescently stained for actin cytoskeletal structure (phalloidin-488; FITC) and cell nuclei (Hoechst 33258; DAPI). NIH 3T3 cells adopt a standard morphology when cultured on fibronectin-coated h-PDMS surfaces (green = actin fibers; blue = cell nuclei). Scale bar: 200 µm.

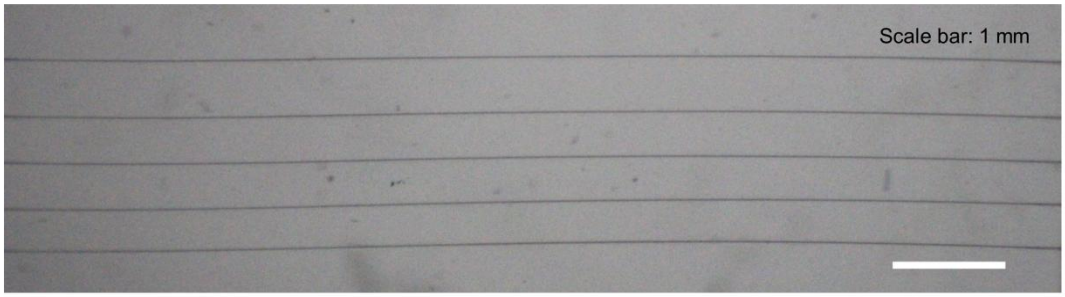

Figure 3.5 Fracture-fabricated microstructures extend into the centimeter-length scale regime.

The maximum length of a crack is limited only by the ability to maintain a constant loading profile over a large area (scale bar = 1mm).

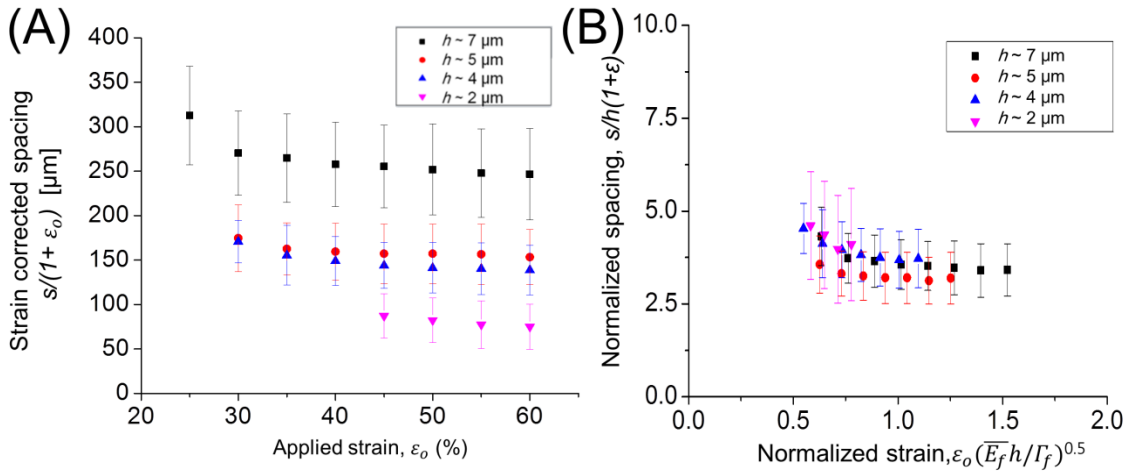

Figure 3.6 Characterization of spacing between cracks generated in the h-PDMS/PDMS material system.

(A) As expected based on theoretical fracture mechanics, the critical strain required to generate cracks is inversely proportional to the thickness of the h-PDMS layer; and the spacing between cracks is proportional to the thickness of the h-PDMS layer and exhibits large variations in spacing within each condition. (B) Non-dimensionalizing the crack spacing data collapses the results to a single curve, indicating that the cracks are strongly localized to the h-PDMS layer.

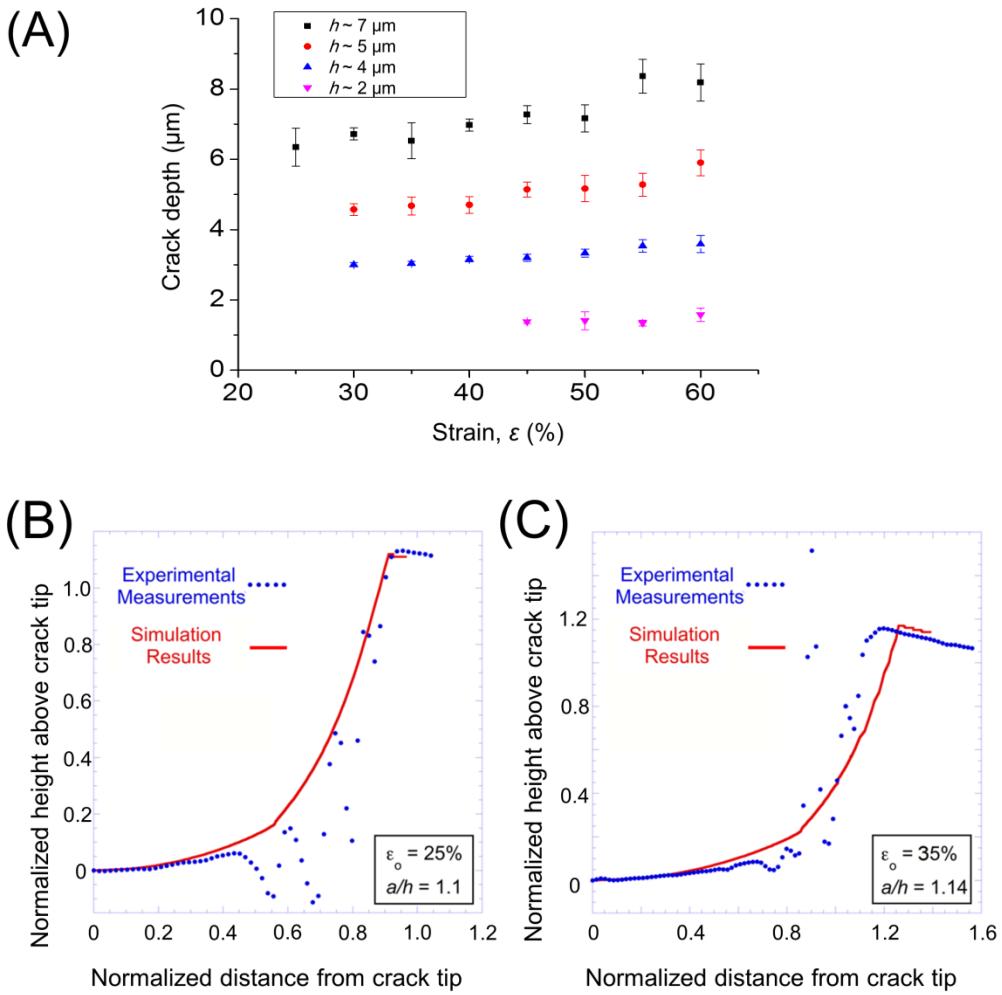

Figure 3.7 Characterization of crack depths in the h-PDMS / PDMS material system for various thicknesses of the brittle h-PDMS layer.

(A) The characteristic depths of the cracks remain stable and well-controlled over a broad range of applied strains; they closely match the thickness of the spin-coated h-PDMS layer. Small increases in crack depth with increasing applied strain suggests that some limited propagation of the crack into the underlying PDMS layer does occur. (B, C) Finite-element simulations demonstrate that a hyperelastic model of the PDMS/h-PDMS system under applied tension matches crack profiles measured by laser scanning profilometry. The x- and y- axes of the graph indicate the lateral distance from the crack tip, and the vertical profile of the crack respectively, both normalized to the thickness of the h-PDMS layer. A limited degree of penetration of the crack into the PDMS layer is expected, and was iteratively determined to match experimental data. The ratio between penetration depth and crack thickness (a/h) was found to be (B) 1.10 for an applied strain

of 25%, and (C) 1.14 for an applied strain of 35%. The hyperelastic material model predicts dramatic deformation in the PDMS at the crack tip to generate the relatively flat bottom of the crack profile. The noise in the experimental data was generated by the interaction between the laser-scanning profilometer and the crack side walls of the crack; it was ignored for fitting purposes.

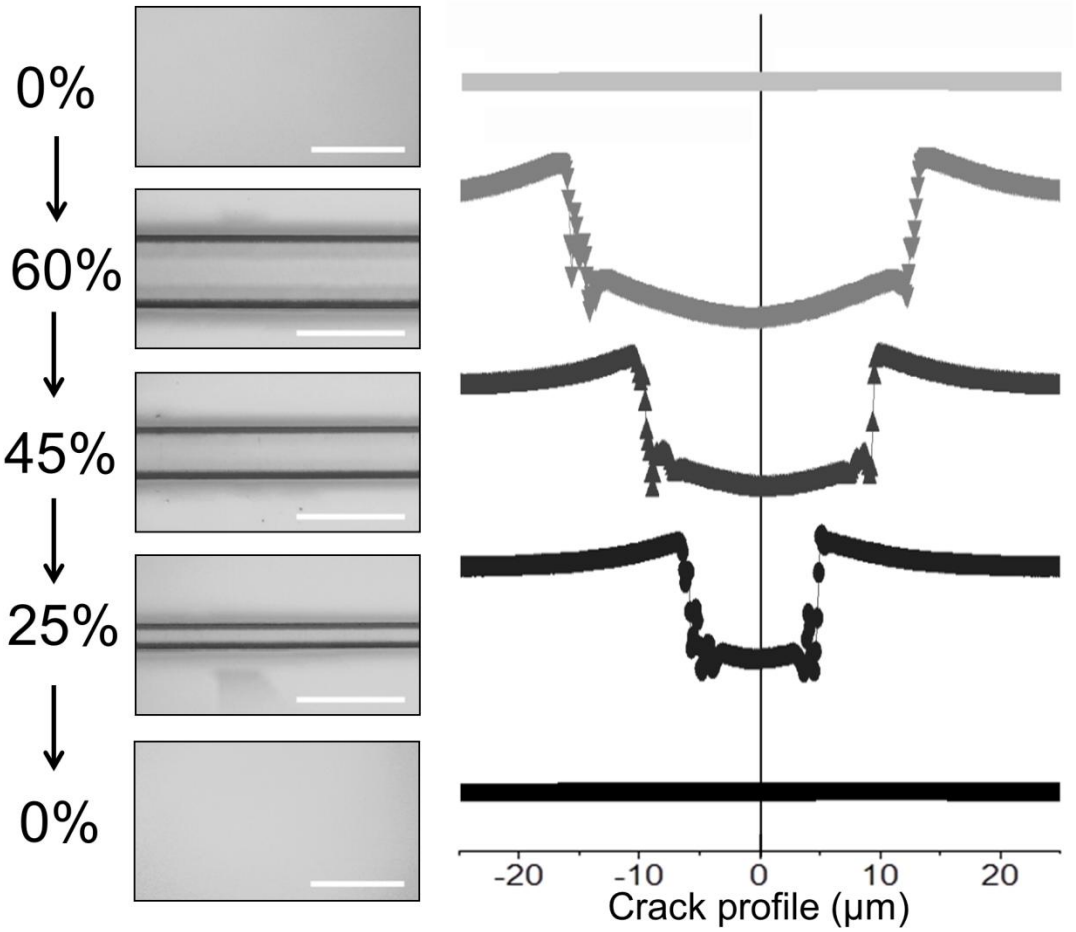

Figure 3.8 Reversible crack profile.

Cracks formed in h-PDMS/PDMS substrates reversibly close when the applied tension is removed. Optical images and high-resolution laser-based surface profilometry of single cracks are unable to detect surface features after a crack is formed and closed, indicating that cracks are completely reversible, and that no delamination occurs between the layers. Scale bar = 50 μm.

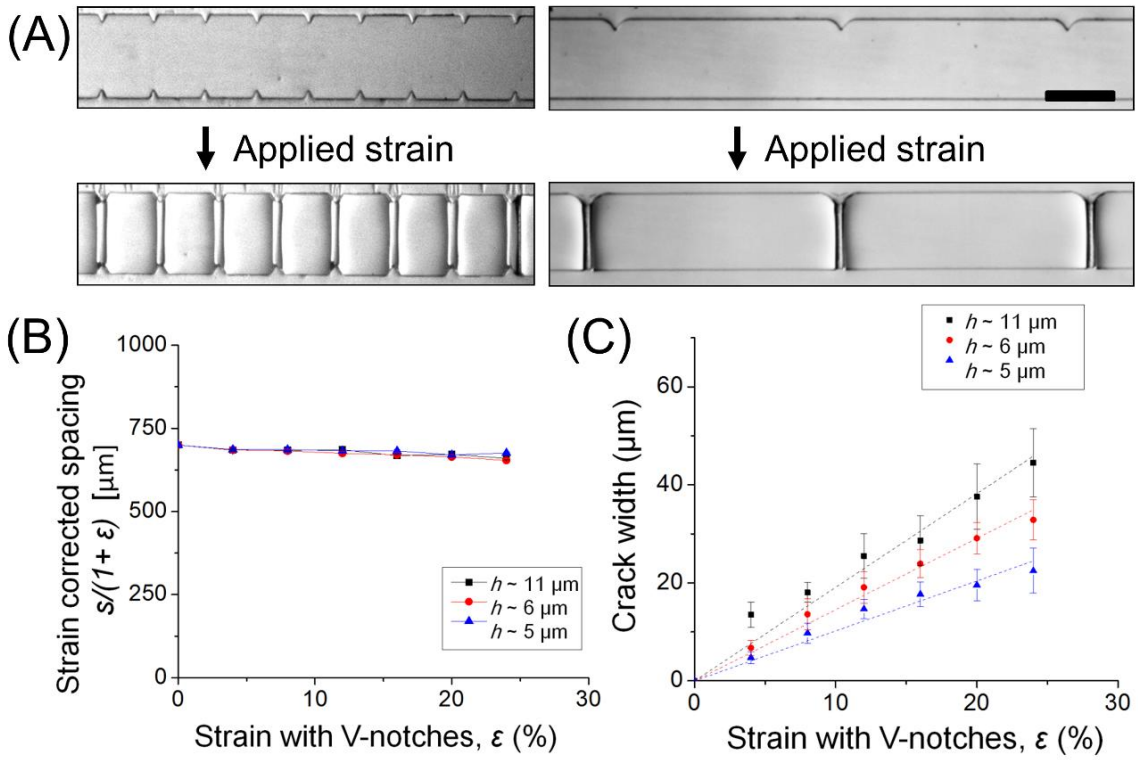

Figure 3.9 Crack position on the device surfaces can be predictively controlled by incorporating V-notch microstructures into the h-PDMS/PDMS substrates.

Cracks are initiated at these points because the notches shield any intrinsic flaws lying between them. (A) V-notches are fabricated at distinct spacings and an applied strain generates cracks at those locations (scale bar = 200 μm). (B) For V-notches spaced 700 μm apart, cracks can be formed at the notch sites. Applied widening strains up to 25% then provide a stable, normalized spacing without generating additional cracks, enabling the formation of adjustable crack structures at specified locations on the substrate. (C) The cracks at these precisely defined locations have well-controlled widths that depend on the applied strain (linear fit R^2 value > 0.97 for all data sets). Hence, the position and width of the reversible cracks can be prescribed accurately.

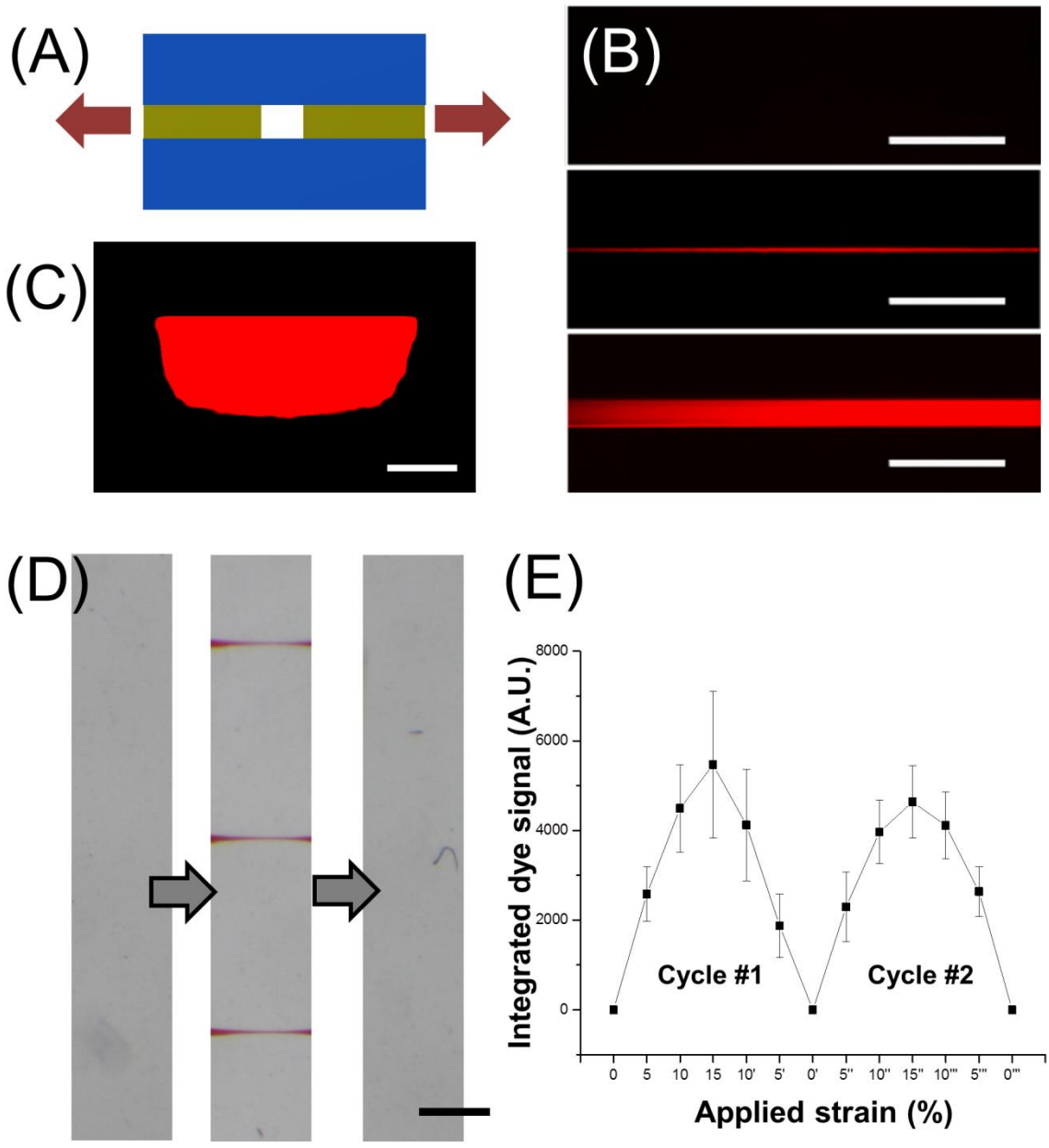
(A)
(B)
(C)
(D)
(E)
Integrated dye signal (A.U.)
8000
6000
4000
2000
0
Cycle #1
Cycle #2
0
5
10
15
10'
5'
0'
5''
10''
15''
10'''
5'''
0'''
Applied strain (%)

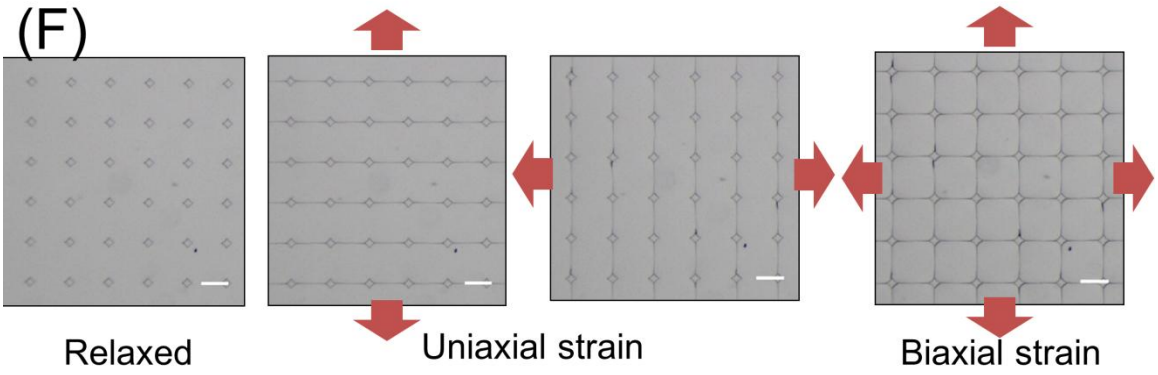

Figure 3.10 Adjustable and reversible microfluidic structures.

(A) A schematic cross-section demonstrating the spontaneous formation of a microfluidic crack structure within an h-PDMS layer embedded in a PDMS substrate. (B) Fluorescent dye is flowed through the microfluidic structures to demonstrate fluidic connections and the ability to adjust the size of fracture-based channels. Scale bar: 50 µm. (C) Representative confocal image of the cross-sectional area of a fracture-fabricated microfluidic channel at 20% strain, filled with fluorescent dye. Scale bar: 5 µm. (D) Optical micrograph showing that multiple cracks can be simultaneously generated and reversibly closed to expel liquid from the microfluidic channels. Scale bar: 100 µm. (E) Integrated signal from the red dye is measured over two repeated open-and-close strain cycles, demonstrating that no measurable level of liquid remains within the channel after closure. This finding further establishes that no delamination occurs between the material layers. (F) Diamond-shaped microfabricated cavities in the h-PDMS layer may be used to simultaneously direct crack formation and provide addressable fluid compartments for a variety of applications requiring valved reaction chambers.

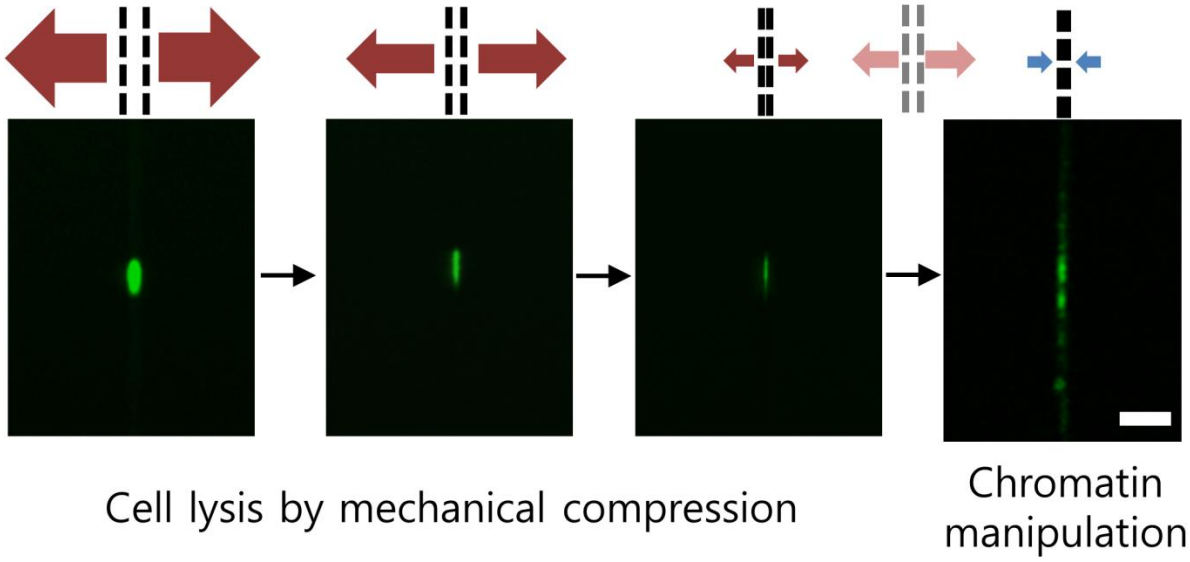

Figure 3.11 Application of adjustable reversible microstructures to lyse single cells and manipulate released chromatin.

A single HeLa cell with a GFP-labeled H2B histone is trapped in enlarged crack-fabricated microchannels and lysed by compression applied via tension release. Once lysed, the channel is opened and closed, forcing the GFP-labeled chromatin to linearize due to elongational shear forces imposed by the fluid, thereby confirming cell lysis. Scale bar = 25 μm.

TABLES

Table 3.1 Mechanical characterization of materials

	PDMS	h-PDMS
Young's modulus	3.7 ± 0.3 MPa	9.2 ± 0.6 MPa
Mode I toughness	460 ± 50 J/m^2 *	12.9 ± 2.7 J/m^2

* data previously published in Mills et al., J. Mater Res. 2008

3.6 REFERENCES

Abate, A.R., Romanowsky, M.B., Agresti, J.J., and Weitz, D.A. (2009). Valve-based flow focusing for drop formation. Applied Physics Letters *94*, 023503.

Adrega, T., and Lacour, S. (2010). Stretchable gold conductors embedded in PDMS and patterned by photolithography: fabrication and electromechanical characterization. Journal of Micromechanics and Microengineering *20*, 055025.

Béfahy, S., Lipnik, P., Pardoen, T., Nascimento, C., Patris, B., Bertrand, P., and Yunus, S. (2009). Thickness and elastic modulus of plasma treated PDMS silica-like surface layer. Langmuir *26*, 3372-3375.

Beuth, J., and Klingbeil, N. (1996). Cracking of thin films bonded to elastic-plastic substrates. Journal of the Mechanics and Physics of Solids *44*, 1411-1428.

Chantiwas, R., Park, S., Soper, S.A., Kim, B.C., Takayama, S., Sunkara, V., Hwang, H., and Cho, Y.-K. (2011). Flexible fabrication and applications of polymer nanochannels and nanoslits. Chemical Society Reviews *40*, 3677-3702.

Cheng, M.-C., Leske, A.T., Matsuoka, T., Kim, B.C., Lee, J., Burns, M.A., Takayama, S., and Biteen, J.S. (2013). Super-Resolution Imaging of PDMS Nanochannels by Single-Molecule Micelle-Assisted Blink Microscopy. The Journal of Physical Chemistry B *117*, 4406-4411.

Dixon, A.R., Moraes, C., Csete, M.E., Thouless, M., Philbert, M.A., and Takayama, S. (2014). One-dimensional patterning of cells in silicone wells via compression-induced fracture. Journal of Biomedical Materials Research Part A *102*, 1361-1369.

Douville, N.J., Li, Z., Takayama, S., and Thouless, M. (2011). Fracture of metal coated elastomers. Soft Matter *7*, 6493-6500.

Futai, N., Gu, W., and Takayama, S. (2004). Rapid Prototyping of Microstructures with Bell-Shaped Cross-Sections and Its Application to Deformation-Based Microfluidic Valves. Adv Mater *16*, 1320-1323.

Grover, W.H., Skelley, A.M., Liu, C.N., Lagally, E.T., and Mathies, R.A. (2003). Monolithic membrane valves and diaphragm pumps for practical large-scale integration into glass microfluidic devices. Sensors and Actuators B: Chemical *89*, 315-323.

Gu, W., Zhu, X., Futai, N., Cho, B.S., and Takayama, S. (2004). Computerized microfluidic cell culture using elastomeric channels and Braille displays. Proceedings of the National Academy of Sciences of the United States of America *101*, 15861-15866.

Huang, J., Kim, B.C., Takayama, S., and Thouless, M. (2014). The control of crack arrays in thin films. J Mater Sci *49*, 255-268.

Huh, D., Mills, K., Zhu, X., Burns, M.A., Thouless, M., and Takayama, S. (2007). Tuneable elastomeric nanochannels for nanofluidic manipulation. Nature materials *6*, 424-428.

Kang, E., Ryoo, J., Jeong, G.S., Choi, Y.Y., Jeong, S.M., Ju, J., Chung, S., Takayama, S., and Lee, S.H. (2013). Large-Scale, Ultrapliable, and Free-Standing Nanomembranes. Adv Mater *25*, 2167-2173.

Kim, B.C., Matsuoka, T., Moraes, C., Huang, J., Thouless, M., and Takayama, S. (2013). Guided fracture of films on soft substrates to create micro/nano-feature arrays with controlled periodicity. Sci Rep-Uk *3*.

Kim, B.C., Moraes, C., Huang, J., Thouless, M., and Takayama, S. (2014). Fracture-based micro-and nanofabrication for biological applications. Biomaterials science *2*, 288-296.

Kim, Y.C., Kang, J.H., Park, S.-J., Yoon, E.-S., and Park, J.-K. (2007). Microfluidic biomechanical device for compressive cell stimulation and lysis. Sensors and Actuators B: Chemical *128*, 108-116.

Lacour, S.P., Wagner, S., Huang, Z., and Suo, Z. (2003). Stretchable gold conductors on elastomeric substrates. Applied Physics Letters *82*, 2404-2406.

Lai, D., Labuz, J.M., Kim, J., Luker, G.D., Shikanov, A., and Takayama, S. (2013). Simple multi-level microchannel fabrication by pseudo-grayscale backside diffused light lithography. RSC Advances *3*, 19467-19473.

Lenshof, A., and Laurell, T. (2010). Continuous separation of cells and particles in microfluidic systems. Chemical Society Reviews *39*, 1203-1217.

Matsuoka, T., Kim, B.C., Huang, J., Douville, N.J., Thouless, M., and Takayama, S. (2012). Nanoscale squeezing in elastomeric nanochannels for single chromatin linearization. Nano Lett *12*, 6480-6484.

Matsuoka, T., Kim, B.C., Moraes, C., Han, M., and Takayama, S. (2013). Micro-and nanofluidic technologies for epigenetic profiling. Biomicrofluidics *7*, 041301.

Melin, J., and Quake, S.R. (2007). Microfluidic large-scale integration: the evolution of design rules for biological automation. Annu Rev Biophys Biomol Struct *36*, 213-231.

Mills, K., Zhu, X., Takayama, S., and Thouless, M. (2008). The mechanical properties of a surface-modified layer on polydimethylsiloxane. J Mater Res *23*, 37-48.

Moraes, C., Kim, B.C., Zhu, X., Mills, K.L., Dixon, A.R., Thouless, M., and Takayama, S. (2014). Defined topologically-complex protein matrices to manipulate cell shape via three-dimensional fiber-like patterns. Lab Chip *14*, 2191-2201.

Moraes, C., Sun, Y., and Simmons, C.A. (2009). Solving the shrinkage-induced PDMS alignment registration issue in multilayer soft lithography. Journal of Micromechanics and Microengineering *19*, 065015.

Moraes, C., Sun, Y., and Simmons, C.A. (2011). (Micro) managing the mechanical microenvironment. Integrative Biology *3*, 959-971.

Odom, T.W., Love, J.C., Wolfe, D.B., Paul, K.E., and Whitesides, G.M. (2002). Improved pattern transfer in soft lithography using composite stamps. Langmuir *18*, 5314-5320.

Schmid, H., and Michel, B. (2000). Siloxane polymers for high-resolution, high-accuracy soft lithography. Macromolecules *33*, 3042-3049.

Sun, Y., Jiang, L.-T., Okada, R., and Fu, J. (2012). UV-Modulated Substrate Rigidity for Multiscale Study of Mechanoresponsive Cellular Behaviors. Langmuir *28*, 10789-10796.

Thouless, M., Li, Z., Douville, N., and Takayama, S. (2011). Periodic cracking of films supported on compliant substrates. Journal of the Mechanics and Physics of Solids *59*, 1927-1937.

Tooley, W.W., Feghhi, S., Han, S.J., Wang, J., and Sniadecki, N.J. (2011). Thermal fracture of oxidized polydimethylsiloxane during soft lithography of nanopost arrays. Journal of Micromechanics and Microengineering *21*, 054013.

Uchida, T., Mills, K., Kuo, C.-H., Roh, W., Tung, Y.-C., Garner, A.L., Koide, K., Thouless, M., and Takayama, S. (2009). External compression-induced fracture patterning on the surface of poly (dimethylsiloxane) cubes and microspheres. Langmuir *25*, 3102-3107.

Unger, M.A., Chou, H.-P., Thorsen, T., Scherer, A., and Quake, S.R. (2000). Monolithic microfabricated valves and pumps by multilayer soft lithography. Science *288*, 113-116.

Zhu, X., Mills, K.L., Peters, P.R., Bahng, J.H., Liu, E.H., Shim, J., Naruse, K., Csete, M.E., Thouless, M., and Takayama, S. (2005). Fabrication of reconfigurable protein matrices by cracking. Nature materials *4*, 403-406.

Chapter 4

Overcoming dilute concentrations and steric hindrance to efficiently capture rare DNA strands in nanochannels

4.1 INTRODUCTION

Nanochannels have demonstrated their utility for linearizing single strands of DNA for high resolution imaging (Aguilar and Craighead, 2013; Diana E. Streng 2009; Matsuoka et al., 2012; Matsuoka et al., 2013). While a technology inherently suited for the analysis of single molecules; the introduction of DNA into a nanochannel has traditionally been most efficient when the initial sample concentration is high or external force is applied (Cabodi et al., 2002; Han and Craighead, 2000; Reisner et al., 2012). This is owed to two fundamental challenges associated with the capture of DNA inside nanochannels from dilute solutions. The first is the entropic cost of concentrating DNA molecules within a small volume, while the second is the entropic cost associated with uncoiling DNA (Cabodi et al., 2002; Mannion et al., 2006). Here we report a device that overcomes both of these challenges by serially using nanochannel-based electrokinetic concentration to position single DNA molecules within a microchannel, and controlled

channel narrowing to induce uncoiling. This novel device utilizes fracture fabrication to create a hybrid micro-nanochannel structure with adjustable cross-sectional dimensions. Careful layering of different toughness and modulus poly(dimethylsiloxane) (PDMS) together with judicious positioning of stress-focusing structures allow differentially sized channels to be created by simply stretching the substrate in perpendicular directions (Kim et al., 2013). The fracture-based nanochannels induce an exclusion-enrichment effect (EEE) to concentrate DNA within the open microchannel region of the device. By subsequently narrowing this microchannel down to nanometer scale cross-sectional dimensions, the DNA strand is linearized and trapped. The methods and techniques described contribute to both the field of fracture-based fabrication a well as the field of nanochannel-based single molecule DNA analysis.

4.2 MATERIALS AND METHODS

Hybrid micro/nanocrack channel fabrication

A four-layer assembly comprised of directly apposed layers of PDMS, silica-like h-PDMS (SL-h-PDMS), hPDMS, and PDMS was designed to generate an array of cracks at pre-determined sites when subjected to applied strains (ε) exceeding the critical strain for each material layer, and was utilized to fabricate 'normally-closed' channels at the micron or nano-scale. Prior to crack induction, feature layers patterned with two pairs of symmetrical micro-features positioned orthogonal to one another (one pair having, sharp inward-pointing tips, and the other having blunt ends) were fabricated using conventional photolithographic techniques (Xia and Whitesides, 1998).

Briefly, micro-features were cast using a master-mold comprised of SU-8 (Microchem) patterned upon a polished silicon wafer. An h-PDMS elastomer mixture was prepared as previously-described (Kim et al., 2014), and cast directly upon the mold by spin-coating. This layer was then incubated at 120℃ for 120 s; after which, a 10:1

mixture of PDMS monomer and a Sylgard 184 cross-linker (Dow Corning) respectively, were deposited above the h-PDMS layer to a target thickness of 5 mm, and cured overnight at 60°C. The cured h-PDMS/PDMS bilayer was then carefully peeled off the SU-8 mold, and loaded into a stretcher (S.T. Japan USA LLC, FL, USA). When uniaxial strain ($\varepsilon \sim 15\%$) was applied in a direction aligned with the mirrored V-notch tips, a single crack was initiated at each tip, and propagated uni-directionally until a complete crack was formed between these tips. The applied strain was then removed, and the h-PDMS layer was covered with tape (3M, Inc) such that only the region between the blunt features remained uncovered. This allowed for the selective treatment of this region by plasma oxidation (200W, 600s), providing it a texture resembling silica. Uniaxial strain ($\varepsilon \sim 6\%$), applied in a direction aligned with these features (and perpendicular to the previously-formed crack) was then used to induce the formation of multiple nanocracks between the blunt micro-features. The resulting SL-h-PDMS/h-PDMS/PDMS tri-layer was then bonded to a PDMS membrane (target thickness: 200 μm) to create channels from the preformed single microcrack/multiple nanocrack pattern, and reservoirs from the sharp and blunt pre-cast micro-features.

Electrokinetic DNA stacking at adjustable microchannel/nanochannels interface

All reservoirs and channels were then perfused with 0.1x TBE buffer, and a λ DNA solution (100 pg/μl, New England Biolabs, Inc), stained with YOYO-1 intercalating dye at a ratio of 20 base pairs/1 dye molecule via one of the sharp-tip reservoirs. A cathode was then positioned within the same sharp-tip reservoir, accompanied by an anode positioned within one of the blunt tip reservoirs. The coincident application of horizontal uniaxial strain and an electric field (80V) was used to induce DNA pre-concentration at the juncture between the open microchannel and nanochannels. Electrokinetic DNA stacking was recorded with a 20x objective installed in a Nikon Ti-U microscope.

Single DNA capturing and elongation in hybrid micro-nanochannel structure

A low concentration DNA solution (1 pg/μl) was loaded into the four-layer assembly, and an electric field (40V) was applied while the adjustable channel was in its open state under an applied horizontal uniaxial strain. The application of the electric field caused the DNA molecule within the sample to migrate through the open microchannel toward the intersecting nanochannels. The inability for the DNA to enter the nanochannels, however, resulted in it becoming stranded at the juncture between these channels and the larger microchannel. The DNA molecule was then linearized by the controlled narrowing of the microchannel through the gradual release of the applied strain.

4.3 RESULTS AND DISCUSSION

Schematic of size-controllable channel structures for concentration, trapping, and elongation of DNA

The fabrication of this device was achieved in two stages. The first stage, during which the stress-focusing features (the sharp tip/blunt tip features) were fabricated, was achieved through casting upon a patterned SU-8 mold. The second stage, during which the microchannel and nanochannels were fabricated, was achieved through the application of controlled uniaxial strain in directions perpendicular to the axes delineated by the reservoir features (Figure 1a). The application of uniaxial strain in the direction perpendicular to the axis delineated by the sharp-tip features allowed for the opening of a microchannel oriented along the sharp-tip axis (Figure 1b). The subsequent application of an electric field between the microchannel and the perpendicularly-oriented

nanochannels allowed for the electrokinetic stacking of DNA molecules at the junctions between the nanochannels and the open microchannel (Figure 1c). The release of the applied strain, ultimately, then generates hydrodynamic forces within the channel network that function to elongate and linearize the DNA as the microchannel returns to its closed state (Figure 1d).

Development of adjustable microchannel/nanochannel hybrid system

The analytical system presented herein exploits the differential material properties of h-PDMS and SL-h-PDMS to generate intersecting cracks of differing scale. Previously, our group developed size controllable micro or nanochannel structures in multilayered materials based on fracture under an applied tensile strain (Huh et al., 2007; Kim et al., 2013; Kim et al., 2014; Matsuoka et al., 2012; Mills et al., 2010; Thouless et al., 2011). In particular, cracks produced in the elastomer PDMS and its variant h-PDMS have been successfully utilized to produce channel structures by subsequent sealing (Kim et al., 2014). An array of cracks produced on a brittle SL-PDMS thin layer on a PDMS slab was used to fabricate nanoscale channels (Huh et al., 2007; Matsuoka et al., 2012; Mills et al., 2010). Similarly, cracks in h-PDMS deposited on a PDMS slab were precisely patterned with stress focusing micro-features, allowing adjustable channels at the micron scale (Kim et al., 2014). Thus, in designing the multi-scale hybrid system, we hypothesized that intense plasma treatment could produce brittle, silica-like nanolayer in the h-PDMS as well, and that cracks of differing scale and orientation could be formed through the sequential application of uniaxial strain at specific magnitudes and directions relative to pre-patterned stress-focusing features (Huang et al., 2014; Kim et al., 2013; Kim et al., 2014). Practically, we sought to create a system wherein multiple nanochannels were patterned perpendicular to a single ‘normally-closed’ microchannel such that communication between these channels occurred only at their points of intersection using the sharp tips and a tape mask for crack localization (Figure 2 and see

Materials and method section). The resulting device included the nanochannels developed in the SL-h-PDMS layer remaining slightly open, even in the absence of an applied strain, due to a residual stress resulting from the plasma oxidation (Douville et al., 2011; Thouless et al., 2011), and the dynamically controllable single channel in the h-PDMS.

DNA stacking by ion concentration polarization (ICP)

In the hybrid channel structures, we demonstrated efficient pre-concentration of negatively charged DNA molecules exploiting exclusion-enrichment effect (EEE) induced by ion concentration polarization (ICP), previously applied for the selective pre-concentration of charged biomolecules (Kim et al., 2010a; Kim et al., 2010b; Wu et al., 2012). When the charged surface of a channel is exposed to an ionic solution, a thin layer of counter-ions forms at their interface to neutralize the existing surface-charge, a structure referred to as an electrical double layer (EDL). At the nanometer scale, the narrow confines of a nano-channel produce overlapping EDLs capable of defining the directionality of ion transfer through the channel under an applied external electric potential (Chantiwas et al., 2011; Kim et al., 2010b; Sparreboom et al., 2009).

Increased negative surface charge on the h-PDMS layer by an intense plasma treatment as well as the nanochannel structures provided a relevant condition to generate ICP. While the adjustable channel was open (by 10% strain), a strong electric field (80V) was applied to lead DNA molecules in the top sharp tip reservoir connected with the cathode to the nanochannel region, and to restrict it at the entrance of the nanochannels due to electric repulsion (Figure 3a). Time lapse images in Figure 3b demonstrated accumulated DNA molecules at the channel interface. This is characterized by the measured intensity of the stained DNA. After one minute of applied voltage, the intensity of fluorescently-stained DNA dramatically increased in the device with nanochannels to the extent that the fluorescence-intensity readings saturate the camera.

Single DNA capturing and linearization in the adjustable channel

Next, we tested the system for efficient capture and elongation of DNA from a dilute solution. The adjustable microchannel could be opened to approximately 70 μm^2 at 10% strain and closed down to 1220 nm^2 by release of the strain (Figure 5A). This cross-sectional size-adjustability of the channel can avoid the entropic cost of uncoiling DNA for introduction into conventional nanochannels, by widening for DNA introduction and narrowing later to linearize DNA by nanoconfinement. We introduced a very low concentration DNA solution (1 pg/μl) into one reservoir. The adjustable microchannel extending from this reservoir was then opened through the application of uniaxial strain applied in a direction perpendicular to the channel to widen it. A mild electric field (approximately 40V) was then applied to localize a single DNA molecule at the junction between the microchannel and nanochannels. The applied field was then removed, and the applied strain was gradually decreased, trapping and stretching the single DNA molecule (Figure 5B). Calculated DNA concentration in the closed state was approximately 145 ng/μl, which is nearly 145,000 times higher relative to the concentration of the initial stock solution. This result indicates that the entropic barrier to load a DNA molecule in such dilute solution into the nanochannel was efficiently overcome by narrowing channel profiles – as opposed to via the use of a highly concentrated DNA stock, or the application of external forces. In addition, the narrowing of the channel created hydrodynamic squeezing flow as well as nano-confinement to efficiently un-coil DNA. The calculated degree of linearization of the trapped DNA (n = 39) in the closed channel was 52 ± 20% regarding the contour length of λ-DNA and the intercalating dye effect (resulting full length of λ-DNA is approximately 17.5 μ) (Figure 5C). This DNA extension results can successfully reveal that the entropic challenge to un-coil DNA is also overcome regardless of less extension (< 3 μl) resulting from DNA adsorption to the channel wall or partial channel collapses before the complete fluid flush.

4.4 CONCLUSIONS

We have developed a fluidic platform capable of overcoming inherent entropic barriers to efficiently pre-concentrate and linearize single DNA molecules isolated from a sample with low initial concentration. These barriers, the entropic costs of concentrating and uncoiling DNA, are overcome through exploitation of the exclusion-enrichment effect and ion concentration polarization, to produce electrokinetic pre-concentration; and the use of hydrodynamic shear, generated by the controlled release of an applied strain, to produce DNA uncoiling within size-adjustable microchannel. Furthermore, the platform itself is manufactured using a fracture-based fabrication technique that enables the reliable fabrication of nanochannel features using standard micropatterning equipment and techniques.

In practice, this platform may be utilized for the capture of DNA, and for the analysis of genetic and epigenetic information at the single molecule level. Such analyses may include the characterization of genetic and epigenetic variation within clonal, or polyclonal, cell populations. Whereas genetic information derived from the study of bulk cell populations inevitably masks the underlying heterogeneity that may distinguish a healthy and diseased cell; the ability to extract information from low concentrations of DNA may represent an opportunity to pursue a more consummate understanding of single-cell genetic heterogeneity, and the mechanisms which may underlie it.

FIGURES

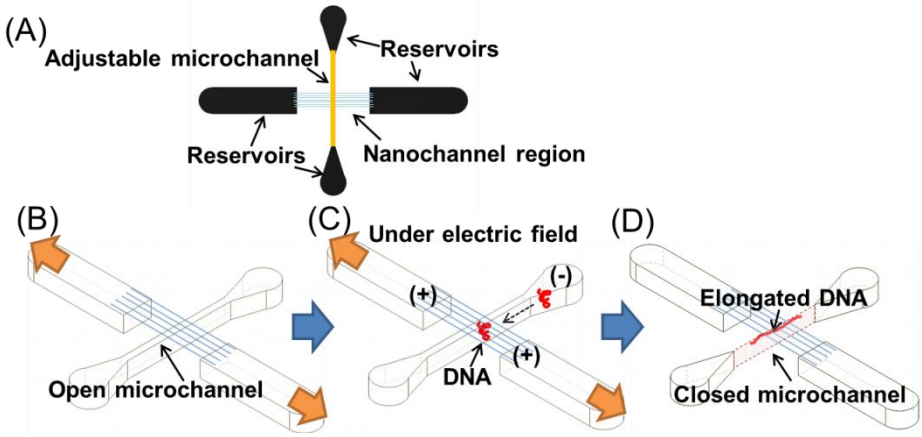

Figure 4.1 Schematics of DNA concentration and squeezing system

(A) a single adjustable microchannel and multiple perpendicularly oriented nanochannels. Each fracture-formed structure originates, and terminates, within a reservoir where nanochannels effectively connect the blunt-tip reservoirs while the microchannel connects the sharp-tip reservoirs. In its operation, (B) the adjustable microchannel is transitioned from a closed to an open-state through the application of a uniaxial strain along an axis perpendicular to the microchannel itself. When in its open state, (C) DNA introduced via one of the sharp-tip reservoirs will migrate and become localized at the juncture between the microchannel and its intersecting nanochannels through ion concentration polarization. (D) The subsequent release of the previously-applied uniaxial strain will then allow the channel to return to its closed-state, and in doing so, generate hydrodynamic shear within the channel sufficient to linearize the trapped DNA molecule.

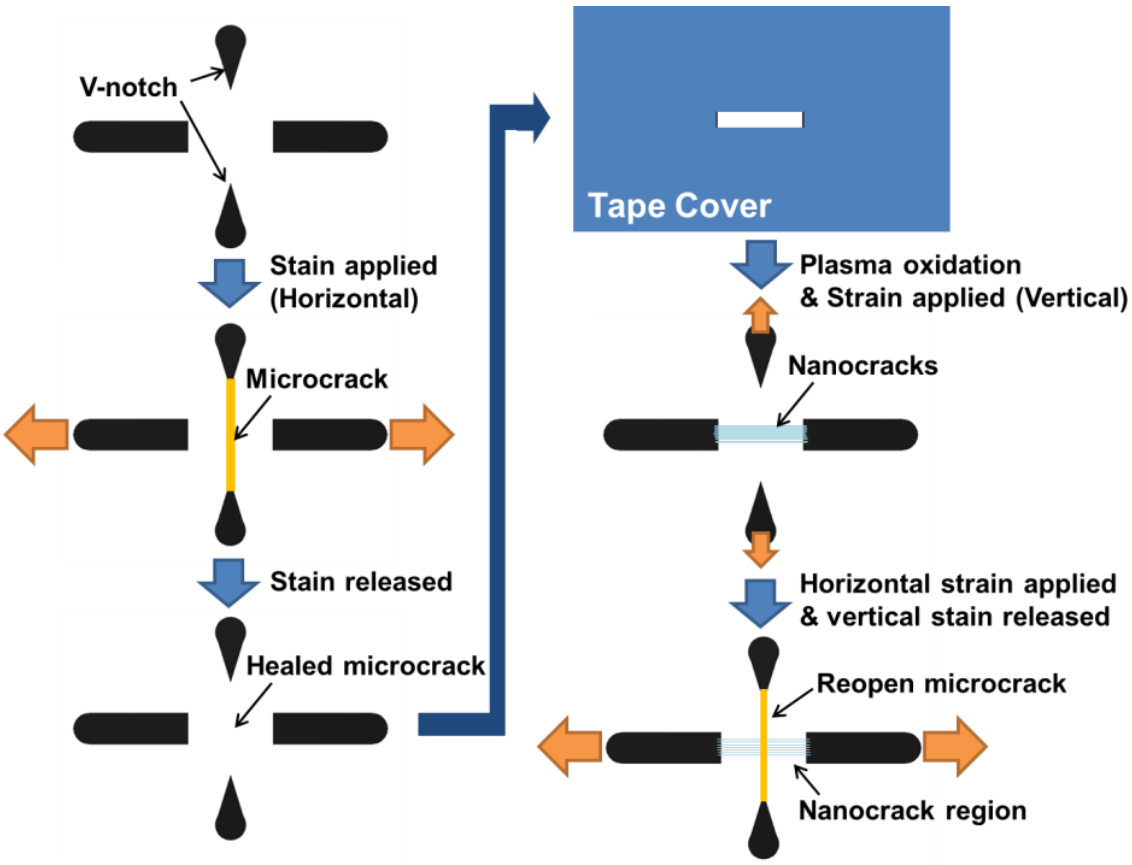

Figure 4.2 Fabrication process of the adjustable channel system for DNA manipulation.

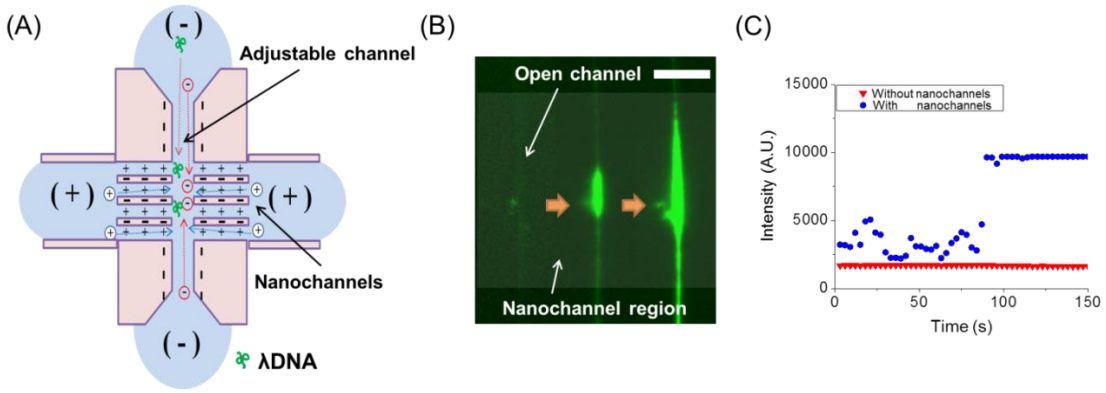

Figure 4.3 Electrokinetic stacking of DNA in hybrid adjustable channel/nanochannel interface.

(A) schematics of ion polarization and stacking generated in the micro/nano junction under the electric field. (B) DNA stacking at the entrance of the nanochannel region. Scale bar is 100 μm. (C) measured intensity of DNA at the nanochannel region.

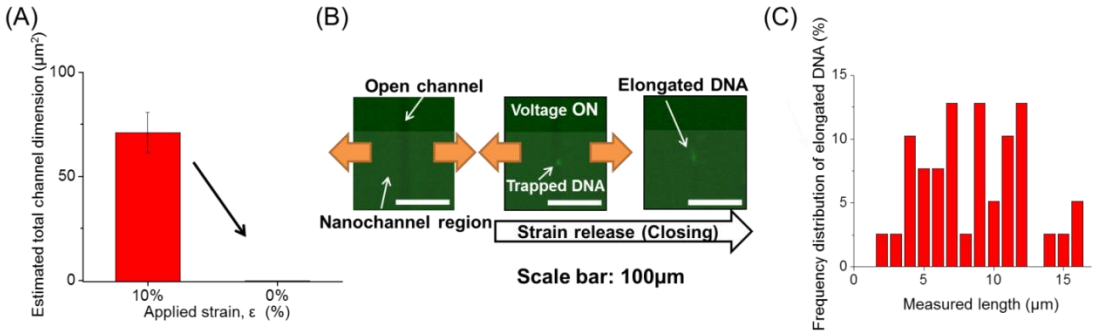

Figure 4.4 Application of the adjustable channel system for single DNA capturing and elongation.

(A) Cross-sectional dimension changes of the adjustable microchannel in response to the applied strain. (B) A diagram depicting the multi-step process of DNA concentration, trapping, and linearization in the adjustable crack channel. Gray color represents the nanochannel region. Scale bar is 100 μm. (C) A plot of the frequency distribution of the lengths of elongated λ-DNA in the closed channel.

4.5 REFERENCES

Aguilar, C.A., and Craighead, H.G. (2013). Micro-and nanoscale devices for the investigation of epigenetics and chromatin dynamics. Nature Nanotechnology *8*, 709-718.

Cabodi, M., Turner, S.W., and Craighead, H.G. (2002). Entropic recoil separation of long DNA molecules. Analytical chemistry *74*, 5169-5174.

Chantiwas, R., Park, S., Soper, S.A., Kim, B.C., Takayama, S., Sunkara, V., Hwang, H., and Cho, Y.-K. (2011). Flexible fabrication and applications of polymer nanochannels and nanoslits. Chemical Society Reviews *40*, 3677-3702.

Diana E. Streng , S.F.L., Junhan Pan , Alena Karpusenka and Robert Riehn (2009). Stretching chromatin through confinement. Lab on a Chip *9*, 2772-2774.

Douville, N.J., Li, Z., Takayama, S., and Thouless, M.D. (2011). Fracture of metal coated elastomers. Soft Matter *7*, 6493-6500.

Han, J., and Craighead, H. (2000). Separation of long DNA molecules in a microfabricated entropic trap array. Science *288*, 1026-1029.
Huang, J., Kim, B.C., Takayama, S., and Thouless, M. (2014). The control of crack arrays in thin films. Journal of Materials Science *49*, 255-268.

Huh, D., Mills, K., Zhu, X., Burns, M.A., Thouless, M., and Takayama, S. (2007). Tuneable elastomeric nanochannels for nanofluidic manipulation. Nature materials *6*, 424-428.

Kim, B.C., Matsuoka, T., Moraes, C., Huang, J., Thouless, M., and Takayama, S. (2013). Guided fracture of films on soft substrates to create micro/nano-feature arrays with controlled periodicity. Scientific reports *3*.

Kim, B.C., Moraes, C., Huang, J., Matsuoka, T., Thouless, M., and Takayama, S. (2014). Fracture-Based Fabrication of Normally Closed, Adjustable, and Fully Reversible Microscale Fluidic Channels. Small.

Kim, H., Kim, J., Kim, E.-G., Heinz, A.J., Kwon, S., and Chun, H. (2010a). Optofluidic in situ maskless lithography of charge selective nanoporous hydrogel for DNA preconcentration. Biomicrofluidics *4*, 043014.

Kim, S.J., Song, Y.-A., and Han, J. (2010b). Nanofluidic concentration devices for biomolecules utilizing ion concentration polarization: theory, fabrication, and applications. Chemical Society Reviews *39*, 912-922.
Mannion, J., Reccius, C., Cross, J., and Craighead, H. (2006). Conformational analysis of single DNA molecules undergoing entropically induced motion in nanochannels. Biophysical journal *90*, 4538-4545.

Matsuoka, T., Kim, B.C., Huang, J., Douville, N.J., Thouless, M., and Takayama, S. (2012). Nanoscale squeezing in elastomeric nanochannels for single chromatin linearization. Nano letters.

Matsuoka, T., Kim, B.C., Moraes, C., Han, M., and Takayama, S. (2013). Micro-and nanofluidic technologies for epigenetic profiling. Biomicrofluidics *7*, 041301.

Mills, K.L., Huh, D., Takayama, S., and Thouless, M.D. (2010). Instantaneous fabrication of arrays of normally closed, adjustable, and reversible nanochannels by tunnel cracking. Lab Chip *10*, 1627-1630.

Reisner, W., Pedersen, J.N., and Austin, R.H. (2012). DNA confinement in nanochannels: physics and biological applications. Reports on Progress in Physics *75*, 106601.

Sparreboom, W., Van Den Berg, A., and Eijkel, J. (2009). Principles and applications of nanofluidic transport. Nature Nanotechnology *4*, 713-720.

Thouless, M.D., Li, Z., Douville, N., and Takayama, S. (2011). Periodic cracking of films supported on compliant substrates. Journal of the Mechanics and Physics of Solids.

Wu, Z.-Y., Li, C.-Y., Guo, X.-L., Li, B., Zhang, D.-W., Xu, Y., and Fang, F. (2012). Nanofracture on fused silica microchannel for Donnan exclusion based electrokinetic stacking of biomolecules. Lab Chip *12*, 3408-3412.

Xia, Y., and Whitesides, G.M. (1998). Soft lithography. Annual review of materials science *28*, 153-184.

Chapter 5

Exploration of material combinations and geometries for efficient electrokinetic stacking of bio-molecule in fracture-based nanofluidics

5.1 INTRODUCTION

Fluidic platforms at the micro/nano-scale have enabled the efficient manipulation of biological fluids, even when present in small volumes and at low concentrations (Matsuoka et al., 2013; Whitesides, 2006). One of powerful applications using such micro/nano-fluidic device is pre-concentration of biomolecules by ion concentration polarization (ICP) that occur in nanofeatures, to increase sensitivity for accurate and precise bioassays (Plecis et al., 2008; Plecis et al., 2005). When the charged surface of a channel is exposed to an ionic solution, a thin layer of counter-ions forms at their interface to neutralize the existing surface-charge, a structure referred to as an electrical double layer (EDL) (Chantiwas et al., 2011; Kim et al., 2010). Within the narrow confines of a nano-channel overlapping EDLs define the directionality of ion transfer through the channel under an applied external electric potential. Such phenomenon has been applied for selective pre-concentration of charged biomolecule pre-concentration

using various charged porous, or channel material systems at the nanoscale (Cheow and Han, 2011; Chou et al., 2002; Chun et al., 2010; Dhopeshwarkar et al., 2005; Jeon et al., 2013; Kirby and Hasselbrink, 2004; Plecis et al., 2008; Wang et al., 2005; Zhang et al., 2013).

One barrier inherent in nanofabrication is the requirement for sophisticated equipment and skills, or complex processing steps including careful alignment and bonding with additional materials. As an efficient, robust, and reliable approach, our group has developed a fracture-based nanofabrication technique using the elastomer polydimethylsiloxane (PDMS), and its variant hard-PDMS (h-PDMS), assembled to form multi-layered systems (Kim et al., 2014). Once assembled, nano-'cracks' may then be generated within these layers through the controlled application of a tensile strain exceeding the critical strain. The resulting channels are functioned as a 'normally closed' channel, capable of undergoing tuneable modulation of channel geometry through varying the magnitude of applied strain (Kim et al., 2014; Matsuoka et al., 2012; Mills et al., 2010). In their 'closed' state, achieved through the release of the applied strain, these channels render adequate nanoconfinement for single molecular capturing and linearization (Huh et al., 2007; Matsuoka et al., 2012). Here, we evaluate fracture based nanochannel systems prepared with different material layers, and differing geometries, for their ability to utilize ICP to efficiently pre-concentrate DNA. Nanochannel structures were formed within a four-layer assembly comprised of PDMS, silica-like hard-PDMS (SL-h-PDMS), h-PDMS, and PDMS by an applied tensile strain.

5.2 MATERIALS AND METHODS

Nanochannel fabrication

Multilayered material systems were designed to generate an array of cracks under applied strains (ε) exceeding the critical strain, and were utilized to fabricate 'normally-closed' nanochannels. Three material-layering combination; PDMS/Silica like PDMS

(SL-PDMS)/PDMS, PDMS/h-PDMS/PDMS, and PDMS/SL-h-PDMS/hPDMS/PDMS (two cases), were characterized for their ability to induce EEE.

Devices with two parallel microgrooves and V-shaped stress concentrator notches at their midpoints were fabricated via standard photolithographic techniques (Xia and Whitesides, 1998). Briefly, channels were cast using a master-mold comprised of SU-8 (Microchem) patterned upon a polished silicon wafer. The master mold was utilized to transfer the micropatterns to each material pairings in common.

1) PDMS/SL-PDMS/PDMS device: Standard PDMS elastomer was prepared by combining a monomer solution and a Sylgard 184 cross-linker (Dow Corning) in a 10:1 ratio. This mixture was then degassed and cast directly upon the master-mold at a thickness of 5 mm, and cured overnight at 60℃. Cured PDMS layers were then carefully removed from the master mold, and covered using tape (3M, Inc), such that only a limited area of the PDMS surface within the vicinity of the V-notch region was left uncovered. The multilayer assembly was then treated by intense plasma oxidation (200W, 600s), forming an oxidized silica-like (SL) layer restricted to only the exposed region. Following oxidation, the tape was removed, and the resulting SL-PDMS/PDMS system was loaded into a stretcher (S.T. Japan USA LLC, FL, USA), and subjected to uniaxial strain ($\varepsilon \sim 6\%$), producing an array of nano-cracks within the brittle oxidized region. The nano-cracks were sealed with a PDMS membrane by plasma bonding, forming nanochannels within the sandwiched structures.

2) PDMS/h-PDMS/PDMS: An h-PDMS elastomer mixture was prepared and cast directly upon the mold by spin-coating, followed by incubation at 120℃ for 120 s. A mixture of 1:10 PDMS was then deposited above the h-PDMS layer to a target thickness of 5 mm, and cured overnight at 60℃. The resulting h-PDMS/PDMS bilayer was then removed from the mold, and subjected to uniaxial strain ($\varepsilon \sim 15\%$), to induce a crack at the V-notch region. The crack in the h-PDMS layer was sealed with a PDMS membrane to form the single nanochannel at 0% strain.

3-1) PDMS/SL-h-PDMS/h-PDMS/PDMS (the first case; a crack generation only in the h-PDMS layer): A single crack in the h-PDMS was fabricated following the

protocol used for the h-PDMS/PDMS system described above. Subsequently, the h-PDMS/PDMS bilayer was exposed to the intense plasma treatment (200W, 600s) to form an SL-h-PDMS layer. The resulting tri-layer SL-h-PDMS/h-PDMS/PDMS system had only the single crack within the h-PDMS layer. Consequent plasma bonding with a PDMS membrane produced the single nanochannel.

3-2) PDMS/SL-h-PDMS/h-PDMS/PDMS (the second case; a single crack within the h-PDMS layer and multiple cracks within the brittle, SL-h-PDMS layer): This system, fabricated in a manner similar to the SL-PDMS/PDMS system, differs in that the layer taped and selectively exposed to plasma oxidation was the h-PDMS layer. The resulting tri-layer SL-h-PDMS/h-PDMS/PDMS system was subjected to uniaxial strain ($\varepsilon \sim 15\%$), producing an array of nano-cracks within the SL-h-PDMS layer, and a single crack within the h-PDMS layer. Thus, multiple nanochannels were fabricated within the material layers sealing with a PDMS membrane.

Estimation of cross-sectional area of each crack-based channels

The total cross-sectional area of each fracture-based channel array was estimated using electrical impedance measurements. Channels were then filled with a 0.1M KCl solution, and Ag/AgCl electrodes were positioned in each reservoir microchannel. Impedance values were recorded when the phase angle was close to 0. The resistance of each system was measured at 0%.

Estimation of charge density depending on geometries

The charge densities depending on each geometry (flat, shallow, and deep notches) were calculated using commercially available multiphysics software, Comsol (COMSOL, Inc). The resulting charge densities across the designed geometries were normalized using the highest charge density value, and then visualized on the geometries.

DNA pre-concentration at micro/nanochannel interface

The nanochannels formed between the two micro-reservoirs in each system were perfused with a 0.1x TBE ionic buffer solution while in their open state, and slowly closed. λ DNA (New England Biolabs, Inc) stained with YOYO-1 intercalating dye at a ratio of 20 base pairs/1 dye molecule was loaded into one of the reservoirs; and this reservoir was then directly connected to the cathode, while the remaining microchannel was connected to anode. Four different electric fields (20V, 40V, 60V, and 80V) were then applied to induce DNA preconcentration. DNA stacking was observed at the micro/nanochannel juncture under all applied fields using a 20x objective installed in a Nikon Ti-U microscope. Final DNA concentrations were quantified based upon a direct comparison between their measured intensity, and the intensity of reference DNA concentrations (100 ng/µl and 10 ng/µl).

5.3 RESULTS AND DISCUSSION

Characterization of nanochannels formed in SL-h-PDMS layer.

Prior to performing DNA pre-concentration, we experimentally assessed and validated our method for the predictable formation and patterning of nano-cracks on an SL-h-PDMS layer, similar to our earlier work characterizing crack formation within a SL-PDMS layer (Huh et al., 2007; Mills et al., 2010; Zhu et al., 2005). The direct exposure of a PDMS surface to intense plasma treatment for 6 min at 200 W is sufficient to render this surface brittle, and activate existing surface defects to produce an array of nanofractures when a uniaxial strain exceeding the critical strain is applied. This unique property is owed to the modulus mismatch between the plasma-treated PDMS surface, and the non-treated PDMS layer beneath it (Shenoy et al., 2000; Thouless et al., 2011).

The deposition of h-PDMS upon a PDMS substrate such that a bilayered (h-PDMS/PDMS) system is formed, allows for the fabrication of a crack within the h-PDMS layer when subjected to uniaxial strain (Kim et al., 2014). By extension, exposing h-PDMS to plasma treatment, and subjecting the resulting surface to uniaxial strain, allows for the fabrication of 'nano-scale cracks' similar to those formed within an SL-PDMS layer (Huh et al., 2007; Mills et al., 2010) (Figure 1a-b). The position and orientation of these nano-cracks may, furthermore, be predetermined by the patterning of stress-focusing features within the multilayered system (Huang et al., 2014; Kim et al., 2014).

In fabricating the SL-h-PDMS/h-PDMS/PDMS system described, an SU-8 mold with a pair of mirrored micro-features having sharp inward-pointing tips, was used to serially cast layers of h-PDMS and PDMS with target thicknesses of approximately 15 μm and 5 mm, respectively. Following curing, the two-layer system was removed from the mold, and prepared for plasma treatment by covering the entire h-PDMS surface with tape, with the exception of the region extending between the two notch features. This region of the h-PDMS surface was left bare to allow to be exposed during plasma treatment. Following plasma oxidation, the application of 6% uniaxial strain, induced the formation of multiple nano-cracks within the SL-h-PDMS layer (Figure 1c); and upon the subsequent application of 15% strain, induced the formation of a single crack within the h-PDMS layer extending between the sharp-tip features. Differences in crack density and the magnitude of the critical strain required to induce cracking within each layer, are derived from difference in modulus mismatch between each pair of apposed material layers (SL-h-PDMS/h-PDMS and h-PDMS/PDMS) as well as the relative thickness of each layer (Kim et al., 2014).

The cracks generated through our controlled-fracture technique were sealed to form 'normally closed' channels respectively, by plasma bonding the patterned surface to a thin PDMS membrane. The connectivity of these channels through the fluid reservoirs as well as the total cross-sectional area of the crack channels were estimated using electrical impedance measurement (Matsuoka et al., 2013; Mills et al., 2010). We prepared three groups of multi-layered systems, each characterized by the materials

which comprise its layers: PDMS/SL-PDMS/PDMS, PDMS/SL-h-PDMS/h-PDMS/PDMS, and PDMS/h-PDMS/PDMS systems.

Devices in each group were individually loaded into a stretcher, and subjected to uniaxial strain (≤ 15% strain) sufficient to induce crack-formation between the paired stress-focusing features. Following crack-formation, the applied strain was removed, devices were bonding with a thin PDMS membrane, and the resulting channels were filled with a 0.1M KCl solution. At 0%, nearly closed channel state, the respective impedance values for devices in each group (n = 3) were recorded to quantitatively estimate the crack channel dimensions. The impedance values of channels formed within h-PDMS-based systems (PDMS/h-PDMS/PDMS and PDMS/SL-h-PDMS/h-PDMS/PDMS) were measured, then the estimated channel dimensions were calculated as below, where D is the total cross-sectional area of channels, ρ is the resistivity of 0.1 M KCl (0.3 Ωm), L is the length of the crack channel (50 μm), $R_m$is the resistance of the each micro-reservoirs, approximately 9 MΩ:

$$R = \frac{\rho L}{D} + 2R_m.$$

By applying this equation, large differences in total cross sectional area when in a closed state were found across the systems examined (Table 1): approximately 26,000 nm^2 (in SL-PDMS/PDMS), 1,200 nm^2 (in SL-h-PDMS/h-PDMS/PDMS), and 30 nm^2 (in h-PDMS/PDMS). These results suggested that crack recovery in the h-PDMS, or SL-h-PDMS, layers was typically superior to that in SL-PDMS due to higher modulus of the h-PDMS that could resist the residual stress compared to the PDMS. In addition, the multiple nano-cracks formed in the SL-h-PDMS layer were less closed, compared to the single crack in the h-PDMS layer.

DNA stacking by ion concentration polarization (ICP) depending on channel geometries

To characterize the practical utility of the fabricated nanochannels for our intended purposes, we attempted to perform an efficient DNA pre-concentration by exploiting the phenomenon of ion concentration polarization (ICP). The theoretical basis for these experiments lay in our awareness that plasma treatment of PDMS and h-PDMS produces negatively charged surfaces with which selective ion separation may be achieved through the restriction of ion transport by overlapping EDLs formed under an electric field. In addition, we hypothesized that the sharp tip features initially designed for controlled crack formation work as DNA focusing region as well, due to larger electric field at the points. The dynamic equilibrium between the electrophoretic force and electric exclusion from the nanochannels allow for efficient stacking of negatively-charged DNA molecules at the juncture between two micro-reservoirs and the perpendicularly-intersecting nanochannels (Figure 2a).

Utilizing the concept and geometrical design, each reservoir was first filled with 0.1x TBE buffer solution, and electrodes were positioned within each reservoirs. A solution containing λ DNA (final concentration: 100 pg/μl) was then added to the reservoir housing the cathode, and an electric field was applied across the channel network. Application of the electric field initiated the electrophoretic movement of ion or charged molecules toward counter electrodes, and consequently, drew the negatively-charged DNA molecules toward the nanochannel region. These molecules, however, were unable to enter the nanochannels due to the presence of electric repulsion produced by the overlapping EDLs present throughout the nanochannels. Consequently, DNA molecules accumulated at the micro/nanochannel interface under the applied electric field, and became concentrated as time passed (Figure 2b-d and See Supporting Information video 1). Compared to randomly distributed DNA stacking along the horizontal interface in the absence of the notch (Figure 2b), distinct DNA focusing was demonstrated in the other two cases having notches (Figure 2c-d). This is because higher charge density at the notches resulting from shorter distances from the opposite micro-grooves induced DNA molecules more concentrated at the tips. Assuming the consistent crack channel densities in the defined nanochannel regions, shorter nanochannels might function as smaller

resistances under the applied electric field. Analytical analysis to calculate the charge density across the geometries supported the experimental results (Figure 2e-g). The highest value was found at the tips, whereas charge density along the interface was identical in the absence of the notch. Charge density at the tip of the deep notch was almost twelve times larger than at the flat interface and twice lager than at the tips of the shallow notch. The resulting charge density differences affected the performance of the DNA stacking. Therefore, micro-grooves with the notches had been utilized to enhance the performance of DNA stacking in the device system.

Quantification of DNA stacking capacity

To quantify the DNA stacking capacity of each multi-layered systems, we measured the DNA concentration as a product of the applied electric field, the time required to complete the stacking process, and the materials present within the multi-layer assembly for five systems: PDMS (alone), PDMS/SL-PDMS/PDMS, PDMS/h-PDMS/PDMS, PDMS/SL-h-PDMS/h-PDMS/PDMS (only a crack in the h-PDMS), and PDMS/SL-h-PDMS/h-PDMS/PDMS (cracks in the h-PDMS and the SL-h-PDMS) (Figure 3a-e). We observed the subsequent application of a strong electric field (> 80V) was capable of producing device failure through a reduction in the integrity of the bond between the PDMS membrane and the cracked surface layer. This effect was not observed under the application of lower field strengths. As efficient DNA concentration was not observed under applied fields < 20V, four electric fields were selected for empirical analysis (20V, 40V, 60V, and 80V). DNA concentrations occurring within designated regions of each system were recorded for 7 min.

Initially, we observed slight differences in background intensity that prevented direct measurement of DNA concentration. In addition, the measured intensities of reference DNA solutions were not linearly proportional to the DNA concentrations they represented. To compensate, the background intensity of each device was reduced

through prolonged exposure to strong UV light for 5 min prior to their use; and the measured intensity of the concentrated DNA (I) was normalized to a reference intensity value (I_0, 10 ng/µl; 100x higher than the test DNA solution). Thus, a relative intensity of 1 (calculated as the ratio of I and I_0), corresponds to a DNA concentration 100x higher than the initial stock solution (Figure 3a-e). Efficient DNA concentration was initially not observed in the PDMS (only), PDMS/h-PDMS/PDMS, and PDMS/SL-h-PDMS/h-PDMS/PDMS systems (only a crack in the h-PDMS layer) under an applied electric field due to the complete absence of fracturing observed within the PDMS (only) system (Figure 3a) and PDMS/h-PDMS/PDMS (Figure 3b). Discontinuities resulting from high crack recovery or too high resistance of a channel in the h-PDMS layer also prevent DNA pre-concentration under the applied electric field (Figure 3c). In the remaining systems, higher DNA concentration was typically detected as the strength of the applied electric field, or the time duration for which it was applied, was increased. Nanochannels formed within the PDMS/SL-PDMS/PDMS system achieved 100x DNA concentration within 7 min under an applied field of 80V (Figure 3d). Similarly, 100x concentrated DNA was produced within 3 min under an applied field of 80V or within 7 min under 60V in the PDMS/SL-h-PDMS/h-PDMS/h-PDMS/PDMS system with multiple nano-cracks in the SL-h-PDMS layer (Figure 3e). The outcome of DNA stacking in the both nanochannel systems did not make significant difference under weak electric fields (below 40V), however, at least two times faster DNA concentration was achieved in the PDMS/SL-h-PDMS/h-PDMS/h-PDMS/PDMS system. These observations suggest the multiple nanochannels formed in the SL-h-PDMS layer to be the superior platform for efficient DNA stacking. This is presumably owing to complex effects of the smaller total dimensions of the patterned nanochannels formed in the SL-h-layer and its surface chemistry. Approximately 13 times smaller total channel dimensions in the PDMS/SL-h-PDMS/h-PDMS/h-PDMS/PDMS system described in Table 1 might render a better condition to produce efficient overlapped electric double layer, which is a basic requirement for ICP.

Moreover, within the latter multi-layer system, the PDMS/SL-h-PDMS/h-PDMS/PDMS system with multicracks in the h-PDMS and the SL-h-PDMS layers, considerable DNA concentration at the defined location was achieved despite of a lower initial concentration (10 pg/µl) that is similar to DNA concentration extracted from few cells. More than 10,000x concentrated DNA was observed, when subjected to an applied field of 80V for a longer time duration (approximately 20 min) (the relative intensity of 1 corresponds to 100 ng/µl, calculated as the ratio of I (measured intensity) and I_0' (10,000x concentrated DNA solution)) (Figure 4). This observation presents potential applications, not only for efficient DNA manipulation and handling extracted from few cells, but also for charged biomolecules in low concentration.

5.4 CONCLUSIONS

We have developed a fluidic platform capable of efficiently pre-concentrating charged molecules at the junction between a 'source' microchannel, and intersecting nanochannels through the controlled application of an electric field sufficient to produce overlapping EDLs within the nanochannel itself. The presence of these overlapping EDLs, consequently, prevents the free movement of negatively charged biomolecules into the channels when in their 'closed' state, and the resulting dynamic equilibrium between the electrophoretic force drawing the charged biomolecules into the nanochannels, and the electric exclusion preventing their passage into the nanochannels, produces stacking of these molecules at the nanochannel-microchannel juncture. In the experiments presented herein, we describe the application of this technique for the efficient pre-concentration of DNA. The practical utility of this technique, however, is not restricted to DNA pre-concentration, and may be applied for the pre-concentration of numerous charged biomolecules including proteins.

FIGURES

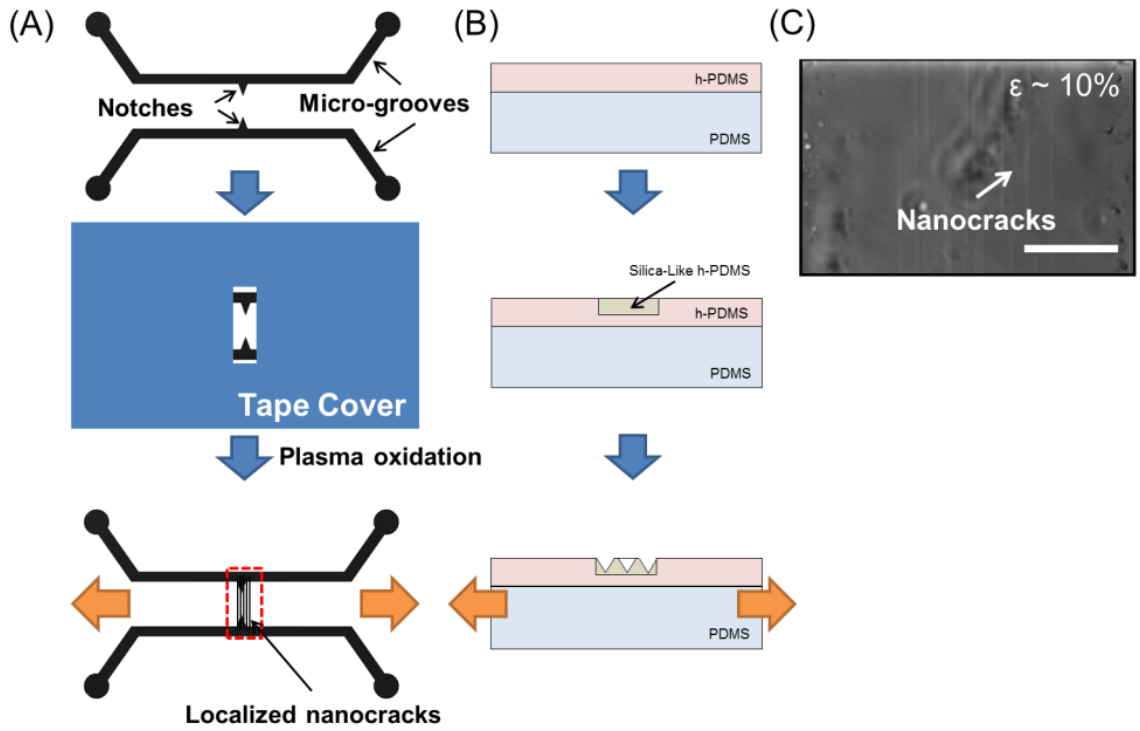

Figure 5.1 Schematics of nanofracture formation in multi-layered system.

(A) localized nano-scale cracks on multi-layered materials. The partial plasma treatment using a tape mask allowed brittle silica like layer formation and nano-cracks were produced at the region under uniaxial tensile strain above critical strain. (B) cross-sectional view of the multi-layered system. (C) nano-cracks on SL-h-PDMS surface at 10% strain. Scale bar is 50 μm.

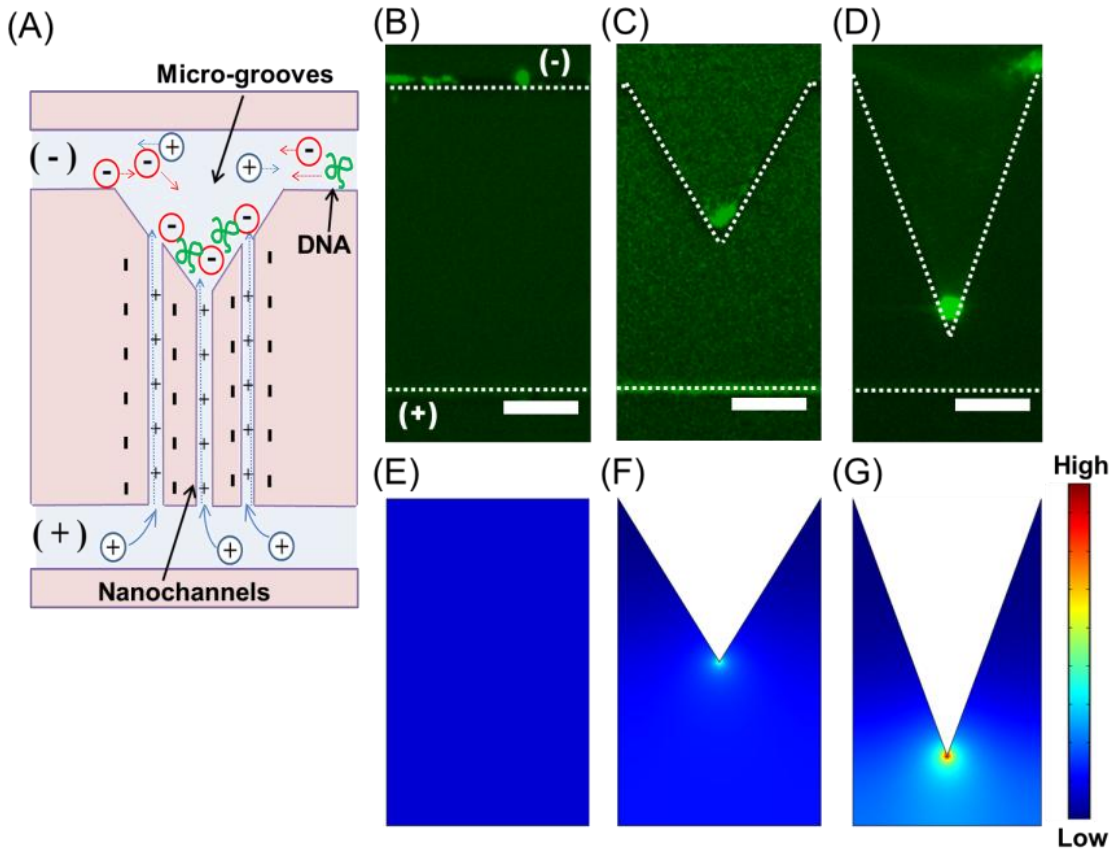

Figure 5.2 Electrokinetic stacking of DNA in nanochannels device.

(A) Schematics of ion polarization and stacking generated in charged nanochannels under the electric field. Anions and negatively charged DNA molecules in top microgroove are concentrated at entrance of nanochannels, while cations freely penetrate the ion-selective barrier formed in nanochannels. (B-D) Concentrated DNA at different notch geometries; (B) flat, (C) shallow, and (D) deep notch. (E-G) Estimated charge density at different notch geometries. Red color represents higher charge density.

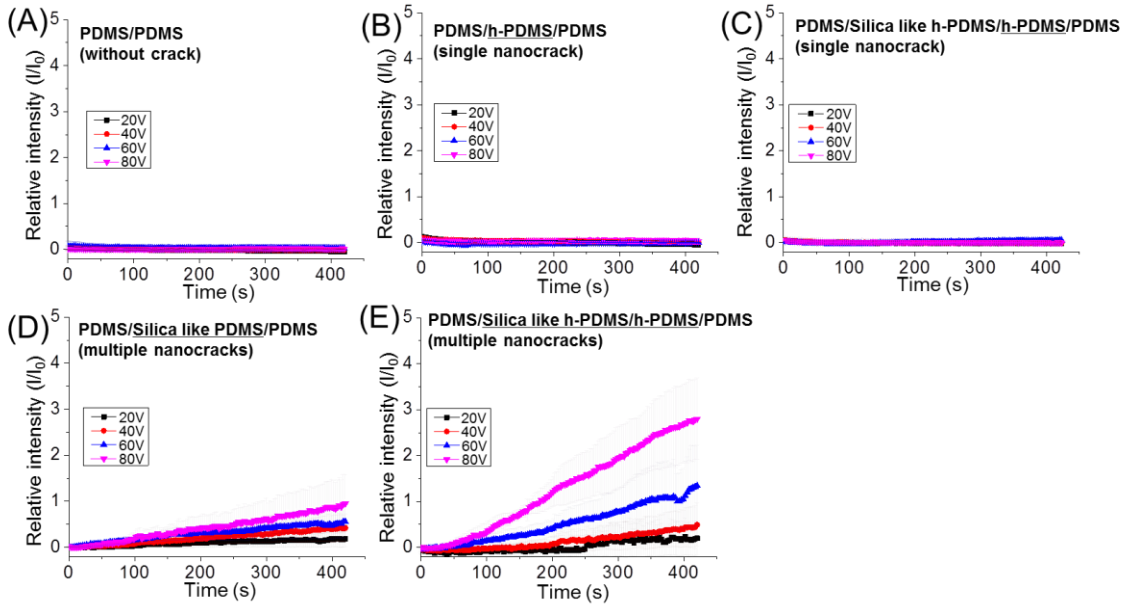

Figure 5.3 Measurement of DNA concentration depending on each material pairings, time, and applied voltage.

Measured DNA concentration was normalized by a reference DNA concentration, 100 times higher concentration (A) in the PDMS, (B) in the h-PDMS/PDMS, (C) in the SL-h-PDMS/PDMS/PDMS (a crack only in the h-PDMS layer), (D) in the SL-PDMS/PDMS, (E) in the SL-h-PDMS/h-PDMS/PDMS (cracks in the h-PDMS and the SL-h-PDMS). (A-E) Relative intensity of 1 presents 100 time higher concentration than the stock DNA concentration. Cracks exist at underline layers.

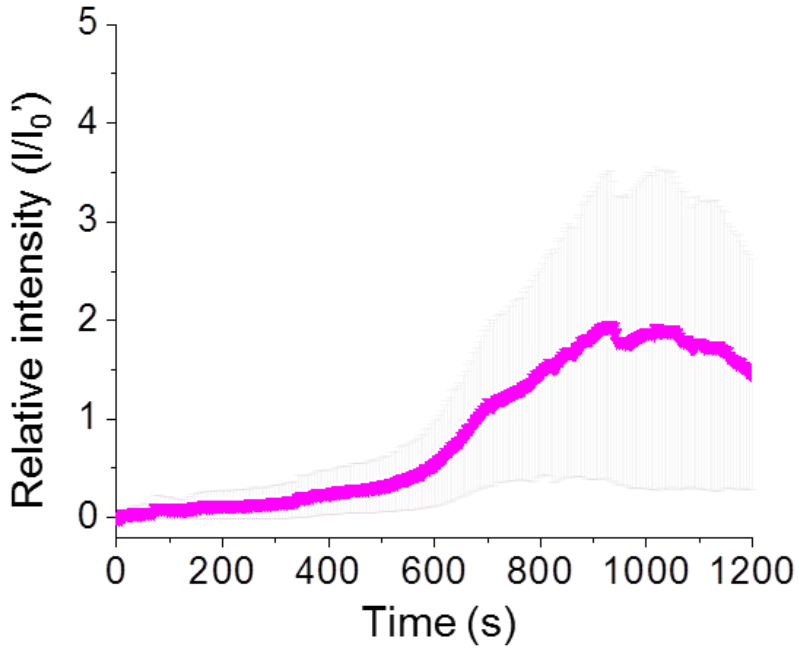

Figure 5.4 Effective DNA stacking at PDMS/SL-h-PDMS/h-PDMS/PDMS system.

Relative intensity of 1 presents 10,000 time higher concentration than the stock DNA concentration.

TABLE

Table 5.1 Estimated total channel dimensions of each material parings system at 0% strain.

	PDMS/Silica-like PDMS/PDMS (multiple nanochannels)	PDMS/Silica-like h-PDMS/h-PDMS/PDMS (multiple nanochannels)	PDMS/h-PDMS/PDMS (single nanochannel)
Estimated total channel dimension (nm^2)	26247.8	1216.4	29.3
S.D.	4320.9	167.7	9.2

Supporting information, Video 1. DNA stacking in PDMS/SL-h-PDMS/h-PDMS/PDMS system under 80V.

5.5 REFERENCES

Chantiwas, R., Park, S., Soper, S.A., Kim, B.C., Takayama, S., Sunkara, V., Hwang, H., and Cho, Y.-K. (2011). Flexible fabrication and applications of polymer nanochannels and nanoslits. Chemical Society Reviews *40*, 3677-3702.

Cheow, L.F., and Han, J. (2011). Continuous signal enhancement for sensitive aptamer affinity probe electrophoresis assay using electrokinetic concentration. Analytical chemistry *83*, 7086-7093.

Chou, C.-F., Tegenfeldt, J.O., Bakajin, O., Chan, S.S., Cox, E.C., Darnton, N., Duke, T., and Austin, R.H. (2002). Electrodeless dielectrophoresis of single-and double-stranded DNA. Biophysical journal *83*, 2170-2179.

Chun, H., Chung, T.D., and Ramsey, J.M. (2010). High yield sample preconcentration using a highly ion-conductive charge-selective polymer. Analytical chemistry *82*, 6287-6292.

Dhopeshwarkar, R., Sun, L., and Crooks, R.M. (2005). Electrokinetic concentration enrichment within a microfluidic device using a hydrogel microplug. Lab Chip *5*, 1148-1154.

Huang, J., Kim, B.C., Takayama, S., and Thouless, M. (2014). The control of crack arrays in thin films. Journal of Materials Science *49*, 255-268.

Huh, D., Mills, K., Zhu, X., Burns, M.A., Thouless, M., and Takayama, S. (2007). Tuneable elastomeric nanochannels for nanofluidic manipulation. Nature materials *6*, 424-428.

Jeon, H., Lee, H., Kang, K.H., and Lim, G. (2013). Ion concentration polarization-based continuous separation device using electrical repulsion in the depletion region. Scientific reports *3*.

Kim, B.C., Moraes, C., Huang, J., Matsuoka, T., Thouless, M., and Takayama, S. (2014). Fracture-Based Fabrication of Normally Closed, Adjustable, and Fully Reversible Microscale Fluidic Channels. Small.

Kim, S.J., Song, Y.-A., and Han, J. (2010). Nanofluidic concentration devices for biomolecules utilizing ion concentration polarization: theory, fabrication, and applications. Chemical Society Reviews *39*, 912-922.

Kirby, B.J., and Hasselbrink, E.F. (2004). Zeta potential of microfluidic substrates: 2. Data for polymers. Electrophoresis *25*, 203-213.

Matsuoka, T., Kim, B.C., Huang, J., Douville, N.J., Thouless, M., and Takayama, S. (2012). Nanoscale squeezing in elastomeric nanochannels for single chromatin linearization. Nano letters.

Matsuoka, T., Kim, B.C., Moraes, C., Han, M., and Takayama, S. (2013). Micro-and nanofluidic technologies for epigenetic profiling. Biomicrofluidics *7*, 041301.

Mills, K.L., Huh, D., Takayama, S., and Thouless, M.D. (2010). Instantaneous fabrication of arrays of normally closed, adjustable, and reversible nanochannels by tunnel cracking. Lab Chip *10*, 1627-1630.

Plecis, A., Nanteuil, C.m., Haghiri-Gosnet, A.-M., and Chen, Y. (2008). Electropreconcentration with charge-selective nanochannels. Analytical chemistry *80*, 9542-9550.

Plecis, A., Schoch, R.B., and Renaud, P. (2005). Ionic transport phenomena in nanofluidics: experimental and theoretical study of the exclusion-enrichment effect on a chip. Nano letters *5*, 1147-1155.

Shenoy, V., Schwartzman, A., and Freund, L.B. (2000). Crack patterns in brittle thin films. International journal of fracture *103*, 1-17.

Thouless, M.D., Li, Z., Douville, N., and Takayama, S. (2011). Periodic cracking of films supported on compliant substrates. Journal of the Mechanics and Physics of Solids.

Wang, Y.-C., Stevens, A.L., and Han, J. (2005). Million-fold preconcentration of proteins and peptides by nanofluidic filter. Analytical chemistry *77*, 4293-4299.

Whitesides, G.M. (2006). The origins and the future of microfluidics. Nature *442*, 368-373.

Xia, Y., and Whitesides, G.M. (1998). Soft lithography. Annual review of materials science *28*, 153-184.

Zhang, D.-W., Zhang, H.-Q., Tian, L., Wang, L., Fang, F., Liu, K., and Wu, Z.-Y. (2013). Microfabrication-free fused silica nanofluidic interface for on chip electrokinetic stacking of DNA. Microfluidics and nanofluidics *14*, 69-76.

Zhu, X., Mills, K.L., Peters, P.R., Bahng, J.H., Liu, E.H., Shim, J., Naruse, K., Csete, M.E., Thouless, M., and Takayama, S. (2005). Fabrication of reconfigurable protein matrices by cracking. Nature materials *4*, 403-406.

Chapter 6

Chromatin inheritance: transmission of histones during DNA replication in nanofluidics

6.1 INTRODUCTION

Epigenetic studies are concerned about inheritable changes that are not dependent on the primary sequence of DNA (Bird, 2007). In this post-genomic era, there is an increased focus on mechanisms of epigenetic inheritance, which are mediated by histone modifications as well as DNA methylation and non-coding RNA (Bird, 2007). In eukaryotic cells, nuclear DNA is packaged into chromatin. Nucleosome is the most basic unit of chromatin, with about 150 bp of DNA wrapped around a protein core comprised of two copies of each of the four histones: H2A, H2B, H3, and H4 (Kornberg, 1974). The assembly of chromatin directly affects the accessibility of the genetic information (Kouzarides, 2007). In a cell cycle, epigenetic information carried by histone modifications as well as genetic information carried by DNA must be duplicated and transmitted from the mother cell to daughter cells. Indeed, these two processes must be

coordinated, as nucleosomes disassemble then re-assemble during DNA replication. A critical question is how the old and new histones are distributed to the two daughter DNAs. There has long been a standing controversy concerning the conservative or dispersive segregation of nucleosomes: the former argues that old histones reassemble preferentially on one arm of DNA replication forks (often posited as derived from the leading-strand synthesis) and new histones on the other, while the latter argues for random reassembly (Annunziato, 2012). A series of results in 1980s has shifted the general opinion in favour of the dispersive segregation model: 1) old histones are reassembled on both arms of replicating simian virus 40 (SV40) chromatin in the absence of new histone synthesis (Cusick et al., 1984); 2) density labelling reveals no preference for tandemly arranged nucleosomes with new histones (Jackson, 1988). However, recent progress has revealed complexities in chromatin dynamics (Zentner and Henikoff, 2013), delineated the histone chaperone pathways (MacAlpine and Almouzni, 2013), and emphasized important roles played by histone PTMs in DNA replication (Alabert and Groth, 2012). There is growing consensus that 1) histone supply and nucleosome assembly are tightly coupled with DNA replication, 2) DNA replication machinery (replisome) are actively involved in disassembly of old nucleosomes and reassembly of new ones, and 3) nucleosome dynamics are affected by multiple processes, most prominently replication-coupled (RC) and replication-independent (RI) deposition of histones. All this recently acquired insight sheds new light on and allows for alternative interpretations of previous experimental analyses of histone segregation, in which these complications are not effectively addressed, or are even intrinsic to the methodologies or systems employed. Framed in the general background of epigenetics and facilitated by technical innovations unforeseeable 30 years ago, there is renewed interest and urgency to revisit these critical issues. This dissertation will clarify mechanisms underlying transmission of histones and epigenetic inheritance.

To study chromatin inheritance under physiological conditions and provide the most biologically-relevant mechanistic insights, we investigate histone transmission during ribosomal DNA replication in a ciliate protozoan, *Tetrahymena*, taking advantage

of nanofluidic chromatin linearization and super resolution optical microscopy. We utilize a fracture-based size-controllable nanochannel device developed previously to visualize histone modification markers on linearized chromatin using a hydrodynamic squeezing flow with nanoconfinement (Kim et al., 2014; Matsuoka et al., 2012). To enable accurate analysis of the chromatin structure I newly combine this technique with the super resolution optical microscopy method of stimulated emission depletion (STED) that can resolve structures within resolutions of tens of nanometers (Rittweger et al., 2009).

The rDNA mini chromosome in *Tetrahymena* was selected as our biological model system to study replication related histone transmission for several reasons. Replication-coupled deposition of canonical H3 and replication-independent deposition of H3.3 expressed in *Tetrahymena* has been well characterized and its genetic manipulation is robust and facile (Cui et al., 2006). In addition, rDNA is a short palindromic structure of approximately 21kb, containing two replication origins located in each side near the center, limits the direction of replication from the center to each telomere-decorated terminus, in contrast to the stochastic replication occurring in higher eukaryotes (Engberg et al., 1974; Yao et al., 1974). A large number of the rDNA mini chromosomes, approximately 9,000 copies, exist in each cell. These unique characteristics of rDNA mini chromosome make it an ideal target for nanofluidic analysis of epigenetic inheritance during DNA replication (Engberg et al., 1974; Yao et al., 1974).

In this study, I additionally utilize a genetically engineered *Tetrahymena* with inducible/repressible expression of hemagglutinin (HA)-tagged histone H3 during DNA replication to visualize and analyze patterns of histone segregation. With nanofluidic chromatin fiber linearization and super resolution localization of newly synthesized histone H3, I expect to address a long standing question concerning epigenetic inheritance.

6.2 METHODS

Strains and culture conditions

Tetrahymena strains (derived from CU428, Tetrahymena Stock Center) were grown in the SPP medium (2% Protease Peptone, 0.2% Dextrose, 0.1% Yeast Extract, 0.003% Fe-EDTA) at 30℃ with gentle shaking (Sweet and Allis, 1998). Logarithmic-phase cells (2×10^5/ml) were collected for subsequent experiments.

Inducidble/repressible expression of hemagglutinin (HA)-tagged H3 in Tetrahymena

For differential labeling of old and new histone H3, the coding sequence of the Cd^{2+}-inducible MTT3 gene was replaced by recombinant DNA encoding a C-terminal HA-tagged canonical H3. Tetrahymena transformants were generated by particle bombardment (Hai and Gorovsky, 1997), with paromomycin resistance conferred by a neo cassette (Mochizuki, 2008). The somatic transformants were assorted to complete replacement, as confirmed by quantitative-PCR. The Cd^{2+}-dependent expression of H3-HA was validated by immuno-fluorescence staining and immuno-blotting (Figure 2b,c).

Chromatin extraction

The genetically engineered Tetrahymena strain was incubated with Cd^{2+} to selectively express HA-tagged H3. To allow for the investigation of histone transmission during DNA replication, Cd^{2+} treatment was limited to 2 hours, so that it covers only one round of DNA replication. The rDNA mini-chromsome resides in nucleoli, which are

localized at the periphery of macronuclei (Gorovsky, 1973). This allows easy separation of nucleoli from the rest of the macronuclei by gentle mechanism shearing (Engberg and Pearlman, 1972). I also optimized procedures for disentanglement and isolation of individual rDNA chromosomes, which involve RNase A treatment to remove rRNA, and high salt solubilisation of non-histone proteins (Borkhardt and Nielsen, 1981). The extracted rDNA chromatin was sequentially diluted in pure water to minimize ionic interactions, and ensure the maintenance of an unfolded conformation.

DNA electrophoresis

rDNA was isolated from chromatin extract by phenol/chloroform extraction and ethanol precipitation. The purity of extracted rDNA was assessed via gel electrophoresis in a 1x TBE buffer solution at 100V. Length of the rDNA was compared with λDNA fragments markers cut by the restriction enzyme *HindIII*.

Immuno-staining

Immunofluorescence staining of *Tetrahymena* cells were conducted by first fixing cells in 2% paraformaldehyde in PBS and permeabilizing with 0.4% Triton X-100 (in PBS). Fixed cells were then incubated with Alexa 488 conjugated-anti-HA antibody overnight. Cells were then stained with DAPI to allow for the visualization of the nucleus, and images were acquired using an inverted microscope, Nikon Ti-U (Nikon, inc).

Fabrication of tunable channel device

Controlled application of strain (ε) to an appropriately layered elastomer-brittle thin film composite was utilized to develop a single ‘normally-closed’, cross-sectional

size controllable nanochannel as described in previous work (Kim et al., 2013). More specifically, two parallel microgrooves with sharp tips and a pair of stress release microfeatures were fabricated on a wafer using conventional soft lithography techniques, and the resulting mold was used to transfer these patterns to multi-layered soft materials. An h-PDMS mixture was spin-coated on the mold to a target thickness of approximately 5 μm and incubated at 120℃ for 120 s. PDMS was then casted above the h-PDMS, and cured at 60℃ overnight.

Preparation of the h-PDMS pre-polymer and cross-linker was conducted by first combining 3.4g of vinyl PDMS pre-polymer (VDT-731, Gelest Corp.), 18 μl of a platinum catalyst (platinum-divinyltetramethyldisiloxane, SIP6831.2, Gelest Corp.), and a drop of a modulator (2,4,6,8-tetramethyl-tetravinylcyclotetrasiloxane, 396281, Sigma-Aldrich). The mixture was then degassed, combined with 1g of a hydrosilane prepolymer (HMS-301; Gelest Corp.) and degassed for a second time. The PDMS mixture was prepared by combining the PDMS pre-polymer and a Sylgard 184 cross-linker (Dow Corning) in a 10:1 ratio.

The cured h-PDMS/PDMS bi-layer was then peeled from the mold and loaded into a stretcher (S.T. Japan USA LLC, FL, USA). Using this device, the bi-layer assembly was then subjected to uniaxial strain ($\varepsilon \sim 20\%$) to generate a single crack originating at the sharp tip features. The resulting fracture pattern was sealed by plasma bonding the assembly to a PDMS membrane to produce a 'normally closed' channel sandwiched between the bi-layer assembly and the membrane.

Chromatin elongation and super-resolution imaging

The rDNA mini-chromatin solution was loaded in one reservoir and allowed to passively enter the size-controllable fracture-fabricated channel while in its open state. The controlled release of the strain holding this channel open allowed the channel to return to its closed-state, resulting in elongation of chromatin through hydrodynamic

shear and nanoconfinement. Histone distribution along the elongated chromatin was observed using a STED microscope (Leica TCS SP8 STED). The signal to noise ratio of images was enhanced by deconvolution using an option available in the associated image analysis software (Huygens Professional) (Schoonderwoert et al., 2013). A point spread function (PSF) of the STED was measured with 100 nm polystyrene beads, and used for the deconvolution process.

6.3 RESULTS AND DISCUSSION

Histone inheritance and development of tuneable nanochannel.

In order to address the fundamental epigenetic question of histone inheritance during DNA replication described above (Figure 1a), I designed a cross-sectional dimension-adjustable fluidic system that is large enough to readily accommodate the relatively bulky (compared to naked DNA) coiled chromatin, while being able to become small enough to effectively linearize the chromatin by changing the magnitude of the applied strain and narrowing the channel (Figure 1b). A fracture-induced channel generated within a hard-polydimethysiloxane (h-PDMS) layer sandwiched between two polydimethysiloxane (PDMS) layers, was used (Kim et al., 2014). The normally closed channel within the triple layer system was precisely produced at a pre-defined location via the use of stress-focusing sharp-tips and adjacent stress-releasing microfeatures (Kim et al., 2013). Using this channel system, rDNA mini-chromatin was loaded into the channel while in its open state, and then elongated by nanoconfinement and hydrodynamic squeezing flow generated as the channels narrowed.

Characterization of rDNA mini-chromosome

In addition to fabricating a novel nanofluidic platform, we also developed a technique for differentiating between old and new histones by the controlled expression of HA tagged H3. The term, nucleosome refers to a basic unit of packaged DNA comprised of an octamer of histone proteins (two (H2A/H2B) dimers, and an $(H3/H4)_2$ tetramer) supporting a wrapped region of DNA containing approximately 150 base pairs (Kornberg, 1974). As the distribution of H2A/H2B-dimers is significantly affected by transcription-dependent turnover, the $(H3/H4)_2$ tetramer has served as the primary focus of investigations concerning histone segregation during DNA replication (Belotserkovskaya et al., 2003; Kireeva et al., 2002). In *Tetrahymena*, the deposition of the canonical histone-H3 is strictly replication-coupled; whereas the deposition of the histone-H3.3 variant is replication-independent; and the canonical histone-H4 is subject to both replication-dependent and replication-independent histone deposition (Cui et al., 2006; Yu and Gorovsky, 1997). For this reason, we chose to position our HA- tag upon H3 rather than on H4, to allow for the effective discrimination of replication dependent histone deposition. To distinguish between old and new histones during DNA replication, an inducible HA-tagged canonical H3 was constructed such that expression could be controlled through activation of the MTT3 promoter by Cd^{2+} treatment (Figure 2a). Indeed, expression of HA-tagged H3 was observed to be rapidly induced and repressed in response to the application and withdrawal of Cd^{2+} in the culture media. As the pool of 'free' H3 in *Tetrahymena* is very small, and subjected to active turnover, our inducible/repressible system essentially served as an on/off switch controlling its availability (Figure 2b-c). We next characterized the optimal dose of Cd^{2+} to both prevent over-expression and ensure its availability minimally perturbed the natural mechanisms of cell growth. We also optimized a protocol to increase the purity of the extracted rDNA mini chromosome by sequential treatment of ethylenediaminetetraacetic acid (EDTA), RNase A, and ammonium sulfate. Respectively, these reagents functioned to chelate metal cations, remove RNA, and solubilize non-histone proteins; ultimately

this treatment retained a disentangled chromosome structure for later elongation. Moreover, purity of the rDNA mini-chromosome was assessed via DNA electrophoresis. Defined length of the extracted rDNA, 21kb, was confirmed through comparison to control ladders (Figure 2d).

Chromatin elongation in nanofluidics

Assuming the 'beads-on-a-string' model, where a linear 'string' of DNA bridges the 'bead'-like nucleosomes, the elongated rDNA mini-chromosome length is estimated to be approximately 2.1-2.6 μm (Luger et al., 1997). These values were then used as a reference to evaluate the degree of stretching achieved within our system. The average length of the linearized chromosome was smaller than the estimated full length. The difference between the observed and expected lengths may be due to residual entanglement within the chromosome by inter-nucleosome interaction, or to ionic interactions which may stabilize folded or higher-order structures.

To characterize the transmission of histones during DNA replication, HA-tagged H3 was expressed by Cd^{2+} treatment for a period of time insufficient for a cell to undergo a complete cell cycle. Subsequent anti-HA antibody treatment enabled the visualization (using STED super-resolution microscopy) of the spatial positions of newly synthesized histones (Fig. 3). In contrast to the globular shaped chromosome clump within bulk solution (Figure 3a-b), linearized chromatin fibers were observed in the closed nanochannel (Figure 3c-d). Subsequently, a single chromatin fiber acquired from the reduced ionic strength solution was elongated in the closed nanochannel (Figure 3e). As the small size of the linearized chromatin fiber was beyond the resolving power of conventional optical microscopy, visualization was only possible via STED microscopy.

Demonstration of the chromatin inheritance

From these images, we detected green fluorescence tags that were distributed in an ostensibly randomized manner upon a background of blue fluorescent tags; suggesting that newly synthesized histones are randomly deposited along the stretched chromosome (Figure 3e). This observation led us to conclude that newly-synthesized histones are dispersively segregated during DNA replication assuming that it was a single chromatin fiber.

6.4 CONCLUSIONS

The use of unique nanofluidics, a biological model system, and super-resolution imaging combined enabled addressing of a long standing question about epigenetic inheritance. Single rDNA mini chromosomes were efficiently captured and linearized within cross-sectional size-adjustable channel, enabling the subsequent visualization of histone deposition within elongated chromatin isolated from the *in vivo* system *Tetrahymena* as compared to *in vitro* system based on reconstructed chromatin fiber. This allowed us to investigate histone transmission during replication in presence of the DNA replication machinery (replisome). Our understanding, gleaned from this platform, supports the hypothesis that new histones are dispersively segregated upon newly synthesized DNA strands. Furthermore, our observation with this platform, used in concert with nano-imaging, suggests that it may be utilized in the future for deeper studies of higher-order chromatin structure including DNA methylation, histone modification, histone variants, and the architectural proteins involved in the formation and regulation of chromatin structures.

FIGURES

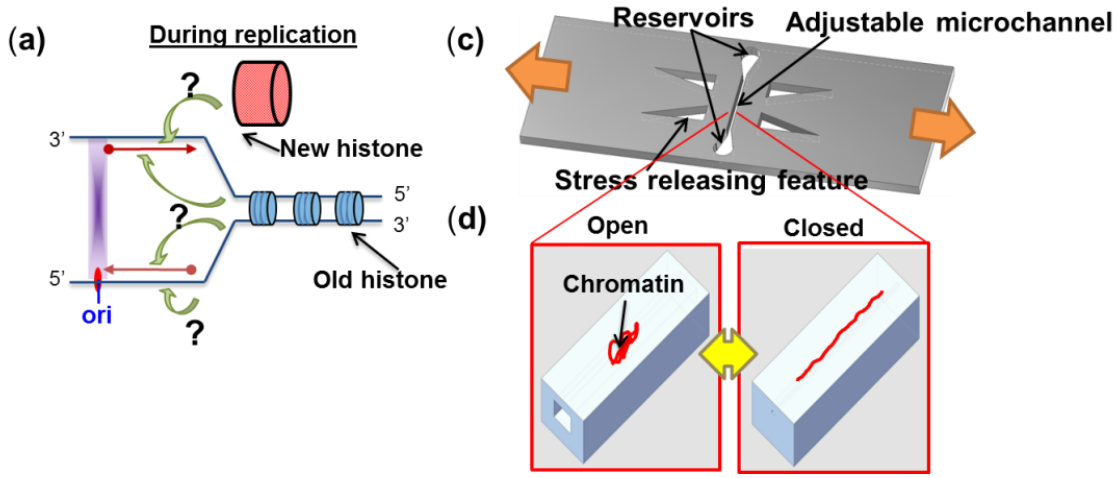

Figure 6.1 schematics of histone inheritance during DNA replication and nanofluidics.

(a) Histone transmission of old and new histones during DNA replication in a half of rDNA structure. Replication initiates at the replication origin, and old and new histones are arranged along two synthesized DNA strands. (b) Cross-sectional shape-adjustable nanofluidic device. The channel was stretch-opened to uptake chromatin and the strain subsequently relaxed to close the channel and linearize the chromatin by a combination of hydrodynamic forces and nanoconfinement.

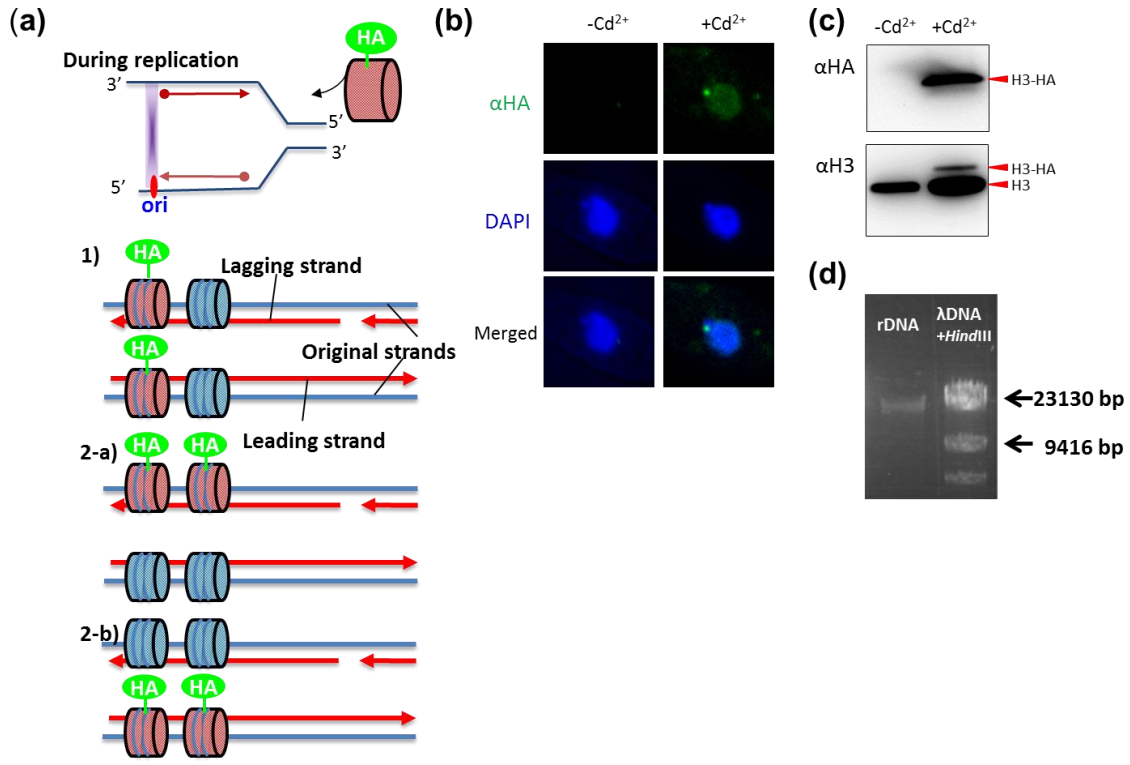

Figure 6.2 Development of a selective HA-tagged H3 expression system.

(a) Scheme depicting newly synthesized histone inheritances. 1) dispersive segregation on both DNA strands, old and new histones are randomly distributed on two DNA strands. 2) two-conservative distribution. Either an old or new histone is preferentially localized at one arm, either leading or lagging of replicated DNA strands. (b) Optical images of Cd^{2+} inducible HA-tagged H3 expression during DNA replication. The genetically modified strain was used to selective expression of HA-tagged H3 in presence of Cd^{2+} in culture media. HA expression was detected by anti-HA antibody conjugated with Alexa 488 fluorophore (Green) and DNA in the nucleus was stained with DAPI (blue). (c) Western blotting. Selective expression of HA-tagged H3 in presence of Cd^{2+} in culture media was analyzed. (d) DNA electrophoresis indicating extracted rDNA length. Length of rDNA extracted from *Tetrahymena* was confirmed with control ladders, λDNA fragments markers cut by *HindIII* restriction enzyme.

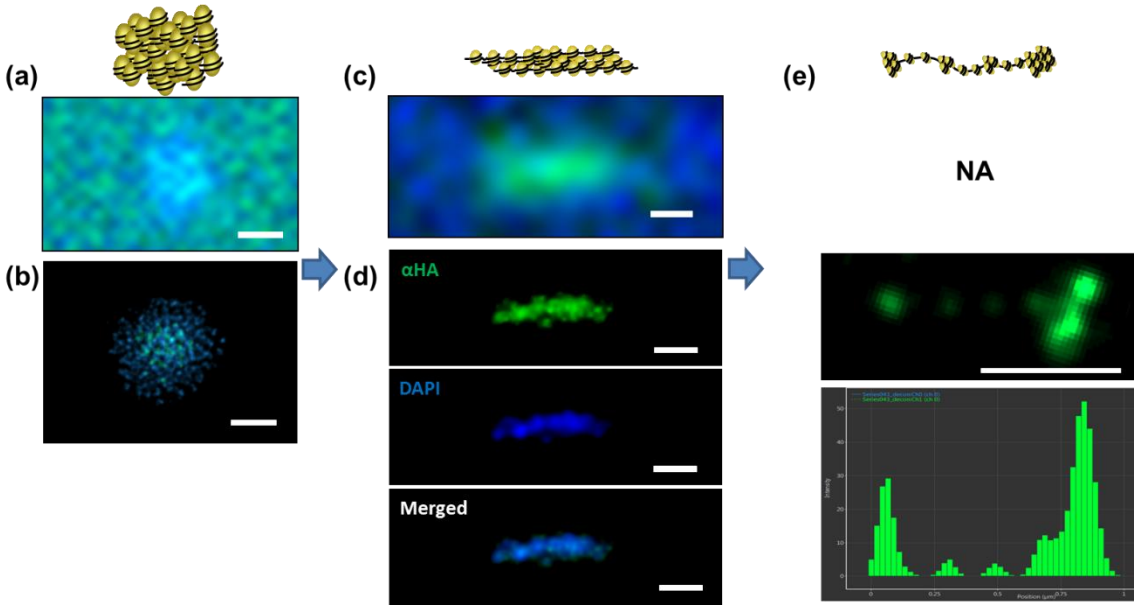

Figure 6.3 Visualized histone inheritance in nanofludics.

(a,b) Tangled chromatin fibers in bulk solution taken by optical microscope (a) and by super-resolution imaging (b). Scale bar is 1 μm. (c, d) elongated chromatin fibers in nanochannel while in a closed state taken by optical microscope (c) and by super resolution imaging (d). Blue color represents DNA stained by DAPI and green color indicates new histone detected by anti-HA antibody. (e) Distribution of new histones along the single linearized chromatin fiber was observed by STED (image), and plotted in the bottom graph. Scale bar is 500 nm.

6.5 References

Alabert, C., and Groth, A. (2012). Chromatin replication and epigenome maintenance. Nature reviews Molecular cell biology *13*, 153-167.

Annunziato, A.T. (2012). Assembling chromatin: The long and winding road. Biochimica et biophysica acta *1819*, 196-210.

Belotserkovskaya, R., Oh, S., Bondarenko, V.A., Orphanides, G., Studitsky, V.M., and Reinberg, D. (2003). FACT facilitates transcription-dependent nucleosome alteration. Science *301*, 1090-1093.

Bird, A. (2007). Perceptions of epigenetics. Nature *447*, 396-398.

Borkhardt, B., and Nielsen, O.F. (1981). An electron microscopic analysis of transcription of nucleolar chromatin isolated from Tetrahymena pyriformis. Chromosoma *84*, 131-143.

Cui, B., Liu, Y., and Gorovsky, M.A. (2006). Deposition and function of histone H3 variants in Tetrahymena thermophila. Molecular and cellular biology *26*, 7719-7730.

Cusick, M.E., DePamphilis, M.L., and Wassarman, P.M. (1984). Dispersive segregation of nucleosomes during replication of simian virus 40 chromosomes. J Mol Biol *178*, 249-271.

Engberg, J., Nilsson, J.R., Pearlman, R.E., and Leick, V. (1974). Induction of nucleolar and mitochondrial DNA replication in Tetrahymena pyriformis. P Natl Acad Sci USA *71*, -894-898.

Engberg, J., and Pearlman, R.E. (1972). The amount of ribosomal RNA genes in Tetrahymena pyriformis in different physiological states. European journal of biochemistry / FEBS *26*, 393-400.

Gorovsky, M.A. (1973). Macro- and micronuclei of Tetrahymena pyriformis: a model system for studying the structure and function of eukaryotic nuclei. The Journal of protozoology *20*, 19-25.

Hai, B., and Gorovsky, M.A. (1997). Germ-line knockout heterokaryons of an essential α-tubulin gene enable high-frequency gene replacement and a test of gene transfer from

somatic to germ-line nuclei in Tetrahymena thermophila. Proceedings of the National Academy of Sciences *94*, 1310-1315.

Jackson, V. (1988). Deposition of newly synthesized histones: hybrid nucleosomes are not tandemly arranged on daughter DNA strands. Biochemistry *27*, 2109-2120.

Kim, B.C., Matsuoka, T., Moraes, C., Huang, J.X., Thouless, M.D., and Takayama, S. (2013). Guided fracture of films on soft substrates to create micro/nano-feature arrays with controlled periodicity. Scientific Reports *3*.

Kim, B.C., Moraes, C., Huang, J., Matsuoka, T., Thouless, M., and Takayama, S. (2014). Fracture-Based Fabrication of Normally Closed, Adjustable, and Fully Reversible Microscale Fluidic Channels. Small.

Kireeva, M.L., Walter, W., Tchernajenko, V., Bondarenko, V., Kashlev, M., and Studitsky, V.M. (2002). Nucleosome remodeling induced by RNA polymerase II: loss of the H2A/H2B dimer during transcription. Molecular cell *9*, 541-552.

Kornberg, R.D. (1974). Chromatin structure: a repeating unit of histones and DNA. Science *184*, 868-871.

Kouzarides, T. (2007). Chromatin modifications and their function. Cell *128*, 693-705.

Luger, K., Mäder, A.W., Richmond, R.K., Sargent, D.F., and Richmond, T.J. (1997). Crystal structure of the nucleosome core particle at 2.8 Å resolution. Nature *389*, 251-260.

MacAlpine, D.M., and Almouzni, G. (2013). Chromatin and DNA replication. Cold Spring Harbor perspectives in biology *5*, a010207.

Matsuoka, T., Kim, B.C., Huang, J.X., Douville, N.J., Thouless, M.D., and Takayama, S. (2012). Nanoscale Squeezing in Elastomeric Nanochannels for Single Chromatin Linearization. Nano Letters *12*, 6480-6484.

Mochizuki, K. (2008). High efficiency transformation of< i> Tetrahymena</i> using a codon-optimized neomycin resistance gene. Gene *425*, 79-83.

Rittweger, E., Han, K.Y., Irvine, S.E., Eggeling, C., and Hell, S.W. (2009). STED microscopy reveals crystal colour centres with nanometric resolution. Nature Photonics *3*, 144-147.

Schoonderwoert, V., Dijkstra, R., Luckinavicius, G., Kobler, O., and van der Voort, H. (2013). Huygens STED Deconvolution Increases Signal-to-Noise and Image Resolution towards 22 nm. Microscopy Today *21*, 38-44.

Sweet, M., and Allis, C. (1998). Culture and manipulation of Tetrahymena. Cells: Culture and Biochemical Analysis of Cells *1*.

Yao, M.C., Kimmel, A.R., and Gorovsky, M.A. (1974). A small number of cistrons for ribosomal RNA in the germinal nucleus of a eukaryote, Tetrahymena pyriformis. P Natl Acad Sci USA *71*, 3082-3086.

Yu, L., and Gorovsky, M.A. (1997). Constitutive expression, not a particular primary sequence, is the important feature of the H3 replacement variant hv2 in Tetrahymena thermophila. Molecular and cellular biology *17*, 6303-6310.

Zentner, G.E., and Henikoff, S. (2013). Regulation of nucleosome dynamics by histone modifications. Nature structural & molecular biology *20*, 259-266.

Chapter 7

Conclusion and Future directions

CONCLUSION

Recent advances in controlled micro and nano-patterning, and the biological applications they potentiate, have greatly enhanced the precision and resolution with which researchers may interrogate biomolecules, and biological systems at the length scale of single cells. As an alternative to conventional template-assisted fabrication techniques; fracture-based fabrication provides a unique ability to achieve efficient micro/nano-patterning on a large scale without the necessity of expensive equipment, specialized facilities, or elaborate technical skills. The body of work presented in this dissertation benefited greatly from the use of fracture-based micro/nano-patterning to create a novel, size-controllable, micro/nanochannel platform in the soft elastomer polydimethylsiloxane (PDMS). The capacity to adjust and tune channel dimensions within this platform was exploited to produce the controlled confinement necessary for the trapping and elongation of coiled chromatin, and the subsequent study of the fundamental mechanisms underlying epigenetic inheritance.

Two fundamental aims were pursued in this dissertation: (1) the development and application of a protocol for the fabrication of precisely defined, and tuneable, micro/nanochannels; and (2) the analysis of histone inheritance through the use of an ideal biological model system and super-resolution imaging.

A. **Optimization of crack channel device**. Precisely controlled fracture-based micro/nano-fabrication techniques were developed based upon an understanding of fundamental fracture mechanics and the properties of specific materials within a series of multi-layered material systems. As the intrinsic flaws present within any material are capable of determining crack positions, the distribution of cracks formed in a material under an applied tensile strain is generally random; resulting in inherently non-uniform crack profiles that produce concomitantly non-uniform molecular elongation. This problem was solved by the integration of stress focusing notch micro-features within the PDMS device to generate an array of micro/nanochannels with a stable periodicity at desired positions (Chapter 2). Furthermore, by selecting specific material combinations for use within the described multi-layered device that restrict crack propagation at the interface between two adjacent layers; crack channel depths could be managed by the thickness of a film deposited on the PDMS substrate, and channel widths could be reversibly controlled by varying the intensity of the applied strains. Consequently, fracture-based fabrication was successfully improved to produce fully reversible dynamic, normally-closed micro/nanochannels with precision control of spacing, depth, and width (Chapter 3).

B. **Biological application of the adjustable channel**. The reversible modulation of channel dimensions allowed for the easy loading of samples containing coiled molecules (e.g. DNA) when the channel is in an open state, and linearization when it is in a closed state. This capability allowed this novel channel system to be highly effective for the efficient pre-concentration, capturing, and linearization of DNA and chromatin via nanoconfinement.

.

A 10,000-fold pre-concentration of DNA was achieved within 20 min under an applied voltage of 80V at pre-defined positions due to the excursion enrichment effect induced by electro-physical chemistry within the nanochannels under the electric field (Chapter 5). Next, a single DNA molecule from a highly dilute solution was trapped and stretched by narrowing channels (Chapter 4). Hybrid micro/nanochannel system, which may offer dynamic cross-sectional change of the microchannel and ion concentration polarization (ICP), and was used to overcome associated entropic barriers of concentrating DNA within small volume as well as uncoiling DNA molecules.

Finally, elongated DNA and chromatin within the adjustable channel was studied to better understand the mechanisms underlying histone inheritance. Structural rearrangements of DNA and chromatin during DNA replication was characterized by "direct reading" of the elongated strand with the help of intercalating dyes (instead of direct base pair sequencing), and antibodies, used as histone markers (Chapter 6). rDNA mini-chromatin extracted from *Tetrahymena* was chosen to elucidate the spatial distribution of histones along replicated DNA due to its unique properties such as palindromic DNA structure, well defined DNA length, and easy genetic modification. Spatial distribution of old and new histones distinguished by selective protein maker expression on H3 histone in the rDNA chromatin was investigated with the aid of super-resolution microscopy, stimulated emission depletion (STED). This result enable to address a long standing question related to histone transmission during DNA replication.

In conclusion, biologically meaningful changes of epigenetic inheritance via the direct visualization of DNA/chromatin in the adjustable channel device were successfully studied. This multi-disciplinary dissertation projects provides insight into unknown epigenetic changes which cannot be addressed with conventional techniques. Practical application of this novel technique can be used for establishment of other epigenetic marker mapping including post translational histone modification and DNA methylation via systematic and quantitative analysis.

FUTURE DIRECTIONS

While this dissertation research has been conducted, in part, to address a fundamental question concerning histone inheritance; additional experiment may be performed to investigate additional physiological systems.

Short term goal

- Characterization of DNA strands

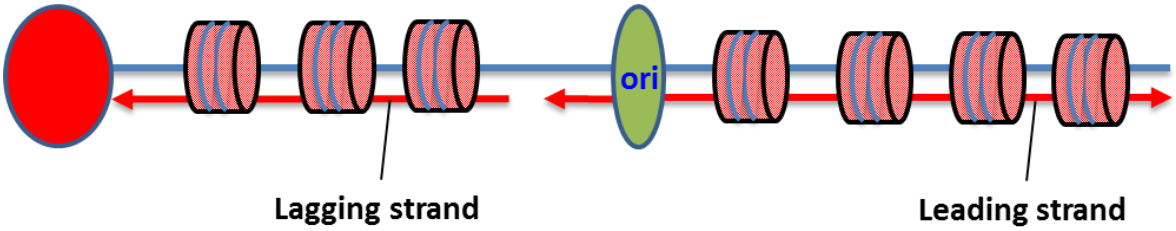

Figure 7.1 characterization of DNA strands synthesized during replication.

Fluorescence tagged telomere marker (Red) can be used to distinguish which ends is lagging or leading strands.

To verify and support my observations regarding histone transmission during replication (as presented in Chapter 6), additional analysis for differentiating the direction of DNA synthesis in rDNA is needed; as well as to confirm singular or plural stacking of the elongated chromatin. Since the direction of rDNA replication is fixed, due to its palindromic structure, the sense strand of the rDNA is always complementally copied to the leading strand, while the anti-sense strand is always complementally copied to the lagging strand. Thus, telomere repeats of 3'GGGGTT5' are replicated during leading strand synthesis whereas the inverse repeating unit of 3'AACCCC5' is replicated during lagging strand synthesis. This behavior may be used to distinguish the leading strand and the lagging strand after labelling by thymidine analogue, BrdU. The newly synthesized

DNA strand with the telomere repeat of 3'GGGGTT5' will be labelled with DAPI and Alexa 555 conjugated anti-BrdU antibody together, while the newly synthesized DNA strand (with the telomere repeat of 3'AACCCC5') will only be labeled by DAPI. Again, the combinatorial distribution of the signals from anti-BrdU antibody and anti-HA antibody will allow for the determination of whether new histones are preferentially deposited upon the leading or the lagging strand.

Long term goal

- Automated system for epigenetic marker analysis

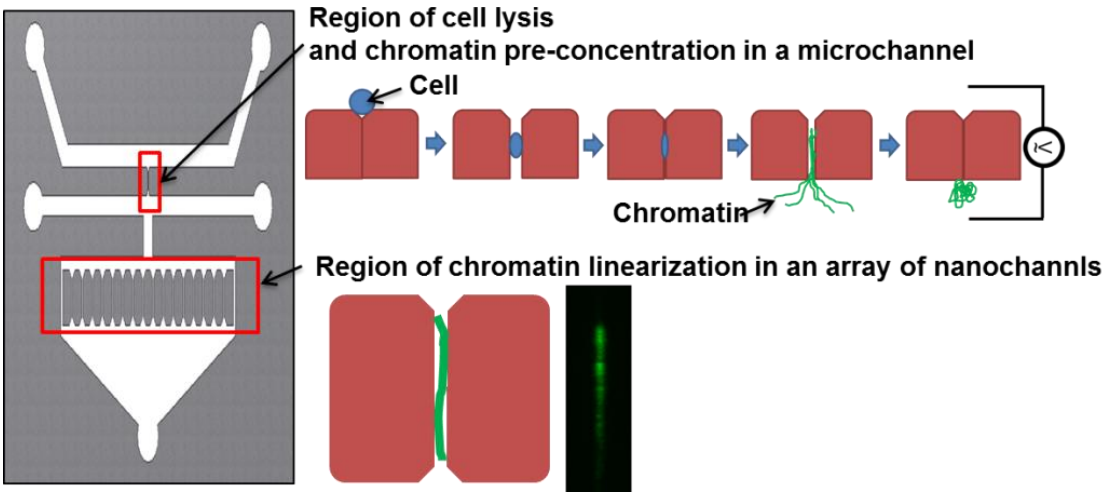

Figure 7.2 Schematic of automated fluidics platform for epigenetic marker analysis

In the course of completing the work presented within this thesis, multiple applications – including chromatin extraction after mechanical cell lysis, DNA pre-concentration, and linearization – have been independently conducted. Each of these functions, individually or collectively, may be integrated to develop an automated system for efficient epigenetic marker mapping. The device can be designed with special regard given to sample preparation procedures, channel geometries and material selections. The device consists of two parts; (1) top single adjustable microchannel and (2) bottom

adjustable nanochannels. In the top microchannel part, chromatin will be directly extracted from lysed cells under mechanical squeezing in the microchannel. Subsequent application of electric field on the first portion will allow to collect the extracted DNA and chromatin at the interface between the closed microchannel and the bottom micro-groove. Next, the chromatin will be transferred to the bottom nanochannel regions by a fluid flow, and then linearized to visualize specific target markers located on the stretched chromatin by the modulation of channel dimension. Consequently, capability of high-throughput analysis in such automated setup will be an excellent tool that would enhance not only our mechanistic understanding of epigenetic profiling but also related physiology and diseases.